Front. Optoelectron. 2014, 7(2): 156–198
DOI 10.1007/s12200-014-0396-4

REVIEW ARTICLE

# Terahertz radiation-enhanced-emission-of-fluorescence

**Jingle LIU (✉)[1], Xi-Cheng ZHANG (✉)[2]**

1 Bloomberg Tradebook LLC, 120 Park Ave, New York, NY 10017, USA
2 The Institute of Optics, University of Rochester, Rochester, NY 14627-0186, USA



**Abstract** Terahertz (THz) wave science and technology have been found countless applications in biomedical imaging, security screening, and non-destructive testing as they approach maturity. However, due to the challenge of high ambient moisture absorption, the development of remote open-air broadband THz spectroscopy technology is lagging behind the compelling need that exists in homeland security, astronomy and environmental monitoring. Furthermore, the underlying physical mechanisms behind the interaction between the THz wave and laser-induced plasma which responds strongly to electromagnetic waves have not been fully understood.

This review aims to explain the light-plasma interaction at THz frequencies within a semiclassical framework along with experimental study of the femtosecond-laser-induced nitrogen plasma fluorescence under the illumination of single-cycle THz pulses. The results indicate that THz-radiation-enhanced-emission-of-fluorescence (THz-REEF) is dominated by electron kinetics in the THz field and the electron-impact excitation of gas molecules/ions. The information of the time-dependent THz field can be recovered from the measured time-resolved THz-REEF from single-color laser induced plasma with the help of the bias as local oscillator. The calculations and experimental verification lead to complete understanding of the science behind these effects and push forward to extend their capabilities in related applications such as remote THz sensing, plasma diagnostics and ultrafast photoluminescence modulation.

Systematic studies in selected gases including neon, argon, krypton, xenon, methane ($CH_4$), ethane ($C_2H_6$), propane ($C_3H_8$), and n-butane ($C_4H_{10}$) gases were performed to obtain an improved understanding of the THz-REEF. The dependences of the enhanced fluorescence on the THz field, laser excitation intensity, gas pressure, and intrinsic atomic properties were experimentally characterized. Both narrow line emission and broad continuum emission of the gas plasma were enhanced by the THz field. Their fluorescence enhancement ratios and time-resolved enhanced fluorescence were largely dependent on the scattering cross section and ionization potential of atoms.

For the first time, we demonstrated a novel 'all-optical' technique of broadband THz wave remote sensing by coherently manipulating the fluorescence emission from asymmetrically ionized gas plasma that interacted with THz waves. By studying the ultrafast electron dynamics under the single cycle THz radiation, we found that the fluorescence emission from laser-induced air plasma was highly dependent on the THz electric field and the symmetry of the electron drift velocity distribution created by two-color laser fields. The time-resolved THz-REEF can be tailored by switching the relative two-color phase and laser polarizations. Owing to the high atmospheric transparency and omni-directional emission pattern of fluorescence, this technique can be used to measure THz pulses at standoff distances with minimal water vapor absorption and unlimited directionality for optical signal collection. The coherent THz wave detection at a distance of 10 m had been demonstrated. The combination of this method and previously demonstrated remote THz generation would eventually make remote THz spectroscopy available.

We also introduced a unique plasma diagnostic method utilizing the THz-wave-enhanced fluorescence emission from the excited atoms or molecules. The electron relaxation time and plasma density were deduced through applying the electron impact excitation/ionization and electron-ion recombination processes to the measured time-delay-dependent enhanced fluorescence. The electron collision dynamics of nitrogen plasma excited at different gas pressures and laser pulse energies were systematically investigated. This plasma diagnostic method offers picosecond temporal resolution and is capable of omni-directional optical signal collection.

The ultrafast quenching dynamics of laser-pulse-

Received December 5, 2013; accepted January 15, 2014

E-mail: mr.jingleliu@gmail.com, xi-cheng.zhang@rochester.edu

induced photoluminescence in semiconductors under the radiation of single-cycle THz pulses was studied. It was found that the quenching in both cadmium telluride (CdTe) and gallium arsenide (GaAs) was linearly proportional to the intensity of incident THz waves and reaches up to 17% and 4% respectively at the peak intensity of 13 MW/cm$^2$. The THz-wave-induced heating of the carriers and lattice and the subsequent decreased efficiency of photocarrier generation and recombination were most likely to be responsible for the quenching. This is potentially useful for the applications of a non-invasive ultrafast light modulator for photoluminescence devices with picoseconds switching time in the fields of the light-emitting devices and optical communication.

**Keywords** terahertz (THz), fluorescence, optical sensing, gas plasma

## 1 Introduction

### 1.1 Historical background

Terahertz (THz) waves, within wavelength range of 0.03 to 3 mm (corresponding frequency range of 0.1 to 10 THz), are electromagnetic waves in the spectral region between well-studied mid-infrared and microwave bands. Figure 1 shows where THz frequency is in the electromagnetic spectrum. The resonant frequencies of rotational and vibrational modes of molecules typically fall in the THz frequency range, which makes THz spectroscopy a promising technique for material characterization and identification [1–4]. Due to the low energy of the THz photon, e.g., 4.1 meV at 1 THz, the THz technology is considered to be non-invasive and safe compared to the X-ray technology. Furthermore, THz wave is able to penetrate many commonly used dielectric materials, including paper, leather, plastic, cloth and etc, which makes THz wave a versatile tool for non-invasive quality control, security inspection and biomedical imaging.

In the past decades, THz-wave related research has experienced rapid advancement in all aspects ranging from highly efficient broadband THz source and detector, to vast and unique applications in biology, chemistry and physics. With the fast development of laser technologies, ultrafast time-domain THz spectroscopic sensing and imaging have been widely available and used in areas of semiconductor characterization, security screening, industrial inspection, biomedical imaging and communications [1,2,5].

Figure 2 shows an example of using THz imaging for non-destructive inspection [6]. THz imaging has been used by National Aeronautics and Space Administration (NASA) scientists in non-destructive inspection of the sprayed-on foam insulation covering the external tank of the space shuttle. The fair transparency and spatial resolution of the THz wave makes THz imaging an effective tool for detecting the hidden defects inside the foam for the purpose of preventing the possible catastrophic detachment of the foam from the space shuttle surface.

Figure 3 shows more examples of the THz wave applications in biomedical imaging and security screening. The low photon energy makes THz imaging an ideal tool for non-invasive medical diagnostics. THz imaging is able to offer important information of the internal structures of human organs or tissues. Figures 3(a) and 3(b) show the THz images of a human tooth and a human hand.

Weapons such as knives and shotguns which are typically made of metal have very high reflectivity for THz wave since the plasma frequency of metal is much higher than THz frequency. The reflective or transmissive THz imaging can be used to detect the concealed weapon carried by terrorists or hostiles. Figures 3(c) and 3(d) show the comparison between the optical image and THz image of the same person carrying a concealed knife.

The bandwidth and spectral resolution are two key

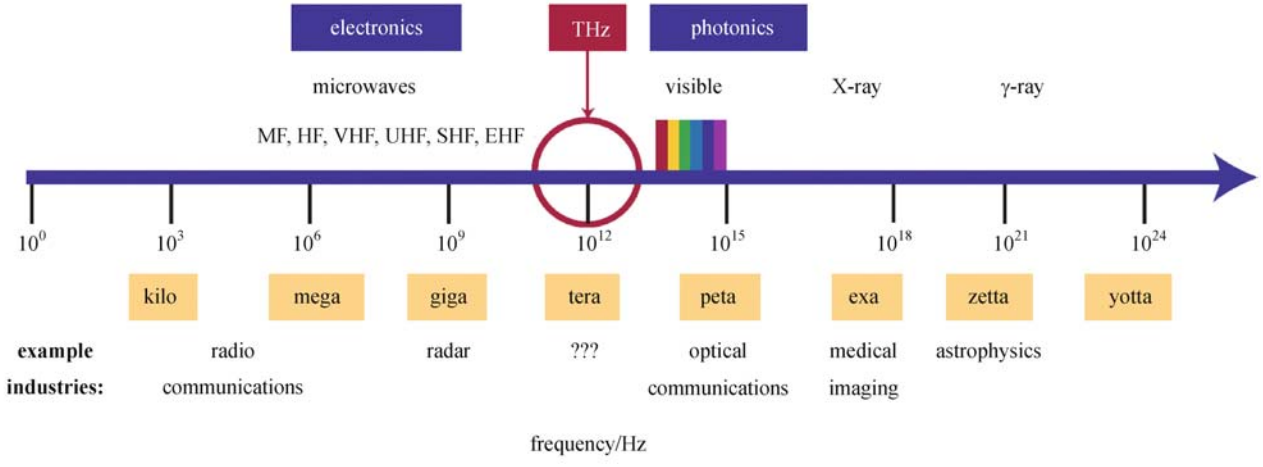


**Fig. 1** Electromagnetic spectrum. THz frequency falls between microwave and visible bands

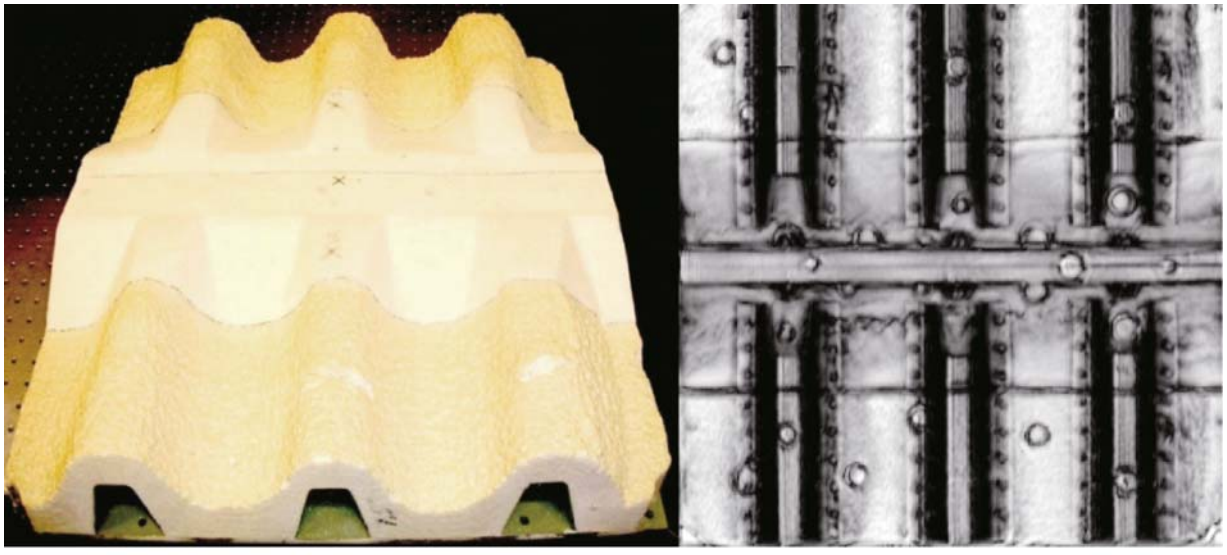


**Fig. 2** (a) Optical image of a 600 mm × 600 mm panel of foam insulation on a metal substrate. There exist some defects hidden underneath the surface; (b) THz image of the same panel. Black circles are the embedded defects [6]

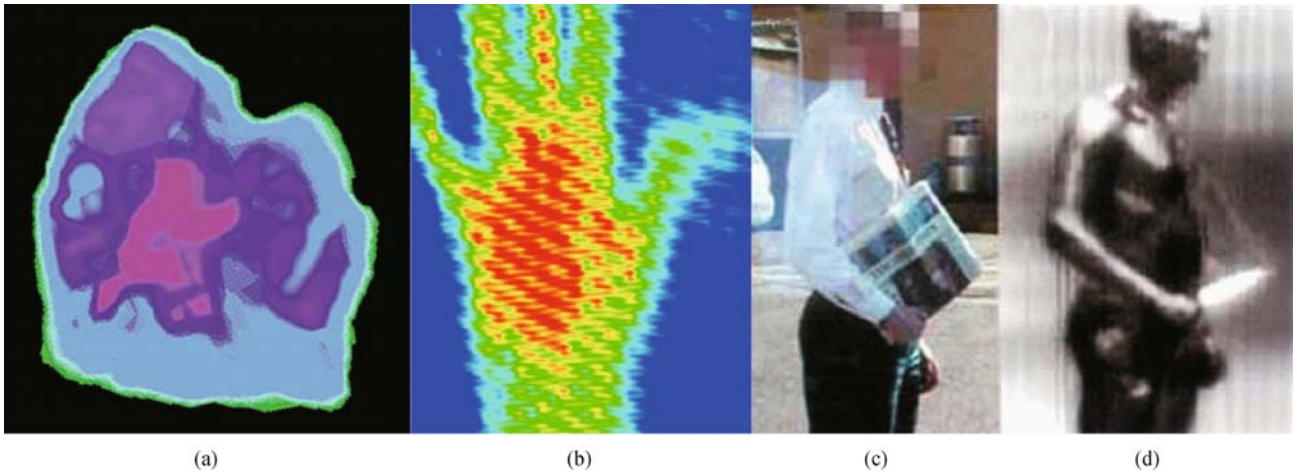


**Fig. 3** (a) Internal structure of a human tooth mapped out by THz imaging; (b) THz image of a human hand; (c) optical image of a person carrying a concealed weapon; (d) THz image of the same person (http://thznetwork.net/)

characteristics of the sensor. However, the bandwidth of the commonly used THz sensor such as the photoconductive antenna and electro-optical crystal is limited by intrinsic phonon modes and the spectral resolution is also limited by the THz beam multi-reflection from detector-air interface [7,8]. In recent years, laser-induced gas plasma has attracted a great amount of research interest and efforts due to its broad spectral coverage and ultrahigh spectral resolution as THz emitter and sensor [9–12]. The typical experimental setup for the THz gas photonics system is plotted in Fig. 4.

Unlike solids, gases do not have a damage threshold, or experience phonon absorption and interface reflection. This uniqueness makes gas an ideal emitter and sensor with broadband spectral response. The only limitation for the previously reported 10 THz bandwidth is the laser pulse duration [12]. Through using even shorter and stronger laser pulses, the spectral range of the THz pulse using gas photonics can be further extended with a higher peak field. These advances will be driving many new discoveries in fundamental molecular, biologic and materials dynamics.

### 1.2 Motivation

The interaction between the THz wave and the laser-induced plasma is the key to various THz technologies since the laser-induced plasma has many unique properties including: 1) Equal number of electrons and ions which respond strongly to the electromagnetic radiation; 2) More

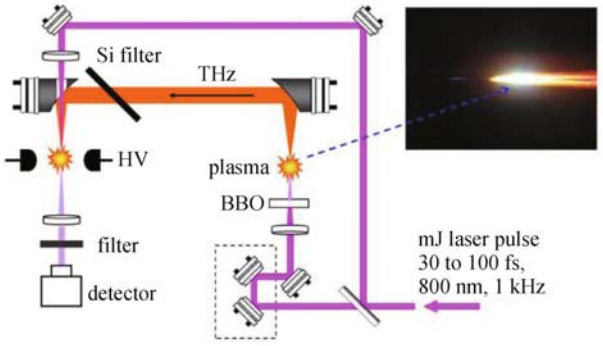


**Fig. 4** Schematics of the experimental setup of broadband THz generation and detection using gases. HV, high voltage; BBO, beta barium borate. Filter, 400 nm interference filter. Detector, photomultiplier tube (Courtesy of Jianming Dai)

chemically reactive than solid state; 3) Remotely controllable formation in the gas; 4) No damage threshold and suitable for power scalable applications. The plasma-related THz technologies include the THz detection using air-biased-coherent-detection which provides ultra broad bandwidth covering the entire THz gap [12]. Figure 5 shows the typical THz waveform and THz spectra obtained from the THz gas photonics system.

However, the light-plasma interaction at THz frequencies has not been fully understood compared to the study in other spectral region such as microwave, visible and X-ray [13–16]. The major reasons are the lacking availability of the strong table-top THz sources, and limited access to the large scale free electron THz laser facilities in the past. The recent development of strong THz sources has made many interesting studies possible, including plasma inverse-bremsstrahlung heating [17,18] and electron impact molecular excitation [19,20] by THz waves. These studies will offer an enhanced understanding of the complex physical picture of the interplaying between the strong-field ionization, plasma dynamics, and THz-wave-induced electron heating. Besides, this study will open new opportunities for many promising THz applications, such as plasma diagnostics and ultrafast photoluminescence modulator.

The laser filament's ultraviolet (UV) emission in the external electric field was previously studied by Sugiyama et al. [21]. The 337.1 nm fluorescence emission from laser-induced nitrogen plasma is measured to be very sensitive to the applied electric field up to 66 kV/cm and increases with the field. This observation can become a basis for a practical remote field measurement. Czarnetzki et al. used fluorescence-dip spectroscopy based on an optical double resonance to probe the Stark splitting in highly excited Rydberg states of atoms [22]. This fluorescence-dip spectroscopy is capable of sensitive measurement of the electric field applied on the laser-induced plasma. The minimum detectable electric field is 5 V/cm. Zhou et al. investigated the second harmonic (532 nm) nanosecond

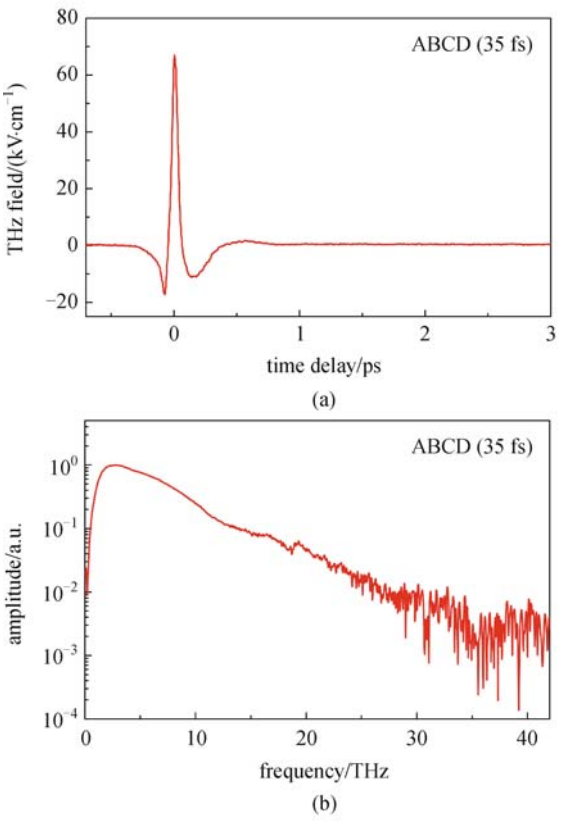


**Fig. 5** (a) Typical time-domain waveform of a THz pulse using air generation and air detection. A 35 fs ultrashort laser pulse is used for Thz generation and detection; (b) corresponding THz spectrum in the frequency domain. ABCD, air-biased-coherent-detection (Courtesy of I-Chen Ho)

(ns)-laser-induced fluorescence under the influence of another fundamental (1064 nm) ns laser pulse which arrived several ns later than the second harmonic pulse [23]. The peak amplitude and life time of the plasma UV emission is greatly enhanced by the delayed fundamental pulse whose field accelerates the pre-existing electrons in the plasma and multiplies them via avalanche. As microwave is incident on the laser-induced plasma, the microwave radiation will be partially reflected and partially absorbed because the plasma frequency is comparable or higher than the microwave frequency. The plasma spectroscopy subjected to the microwave electric field has been extensively studied in the past [24].

The fluorescence from laser-induced gas plasma under the influence of the THz radiation can be used as a probe for the theoretical and experimental investigation of fundamental physical mechanism behind the THz-plasma interaction. The fluorescence emission under THz pulse radiation in a variety of gases including monoatomic gases, diatomic gases, and alkaine gases, needs to be systematically investigated to address the universality of phenomena which occur in the interaction between THz wave and gas plasma.

Complete study on gas pressure and laser power dependence will be needed to reveal the general relationship between the plasma properties and fluorescence enhancement, which can be used as plasma diagnostic method with pico-second temporal resolution and omni-directional optical signal collection.

Besides the study in gas, the study of the THz-plasma interaction in the semiconductor would also be of significant interest to high-speed optoelectronic applications. The modulation of the photoluminescence emitted from semiconductor by the THz pulse on picosecond time scale can provide a non-invasive ultrafast light modulator for light-emitting device and optical communication application.

A long existing challenge faced by THz scientists and researchers in the past decades has been broadband THz remote spectroscopy, which is in compelling needs in the fields of the environmental control, homeland security and astronomy. To achieve THz remote spectroscopy, one needs to remotely generate and detect the THz wave. Previously Dai et al. demonstrated the long distance THz generation by focusing two-color laser beam remotely [25]. The schematic and results of the remote THz generation are shown in Fig. 6.

Nonetheless, remote THz sensing remained an obstacle to be conquered. Two major difficulties in the remote sensing are the strong ambient water vapor absorption at THz frequencies and the requirement for signal collection in the backward direction. The huge absorption of water molecules prevents the THz wave from propagating long before getting greatly attenuated, which makes acquisition of the THz signal at remote distance highly desirable to avoid the signal loss over the long distance propagation. Moreover, backward signal collection is essential because the forward or sideways signal collection is not realistic in real practice where the operator sends out the generation beam and collects the backward signal at the same physical location. Conventional THz detection methods, including photoconductive antenna, electro-optical sampling, and air-breakdown-coherent-detection [7,8,26], are not suitable solutions since they either require on-site detectors or forward signal collection. One of the major focuses in this paper is to introduce a unique method for broadband THz remote sensing using “all optical” control without using

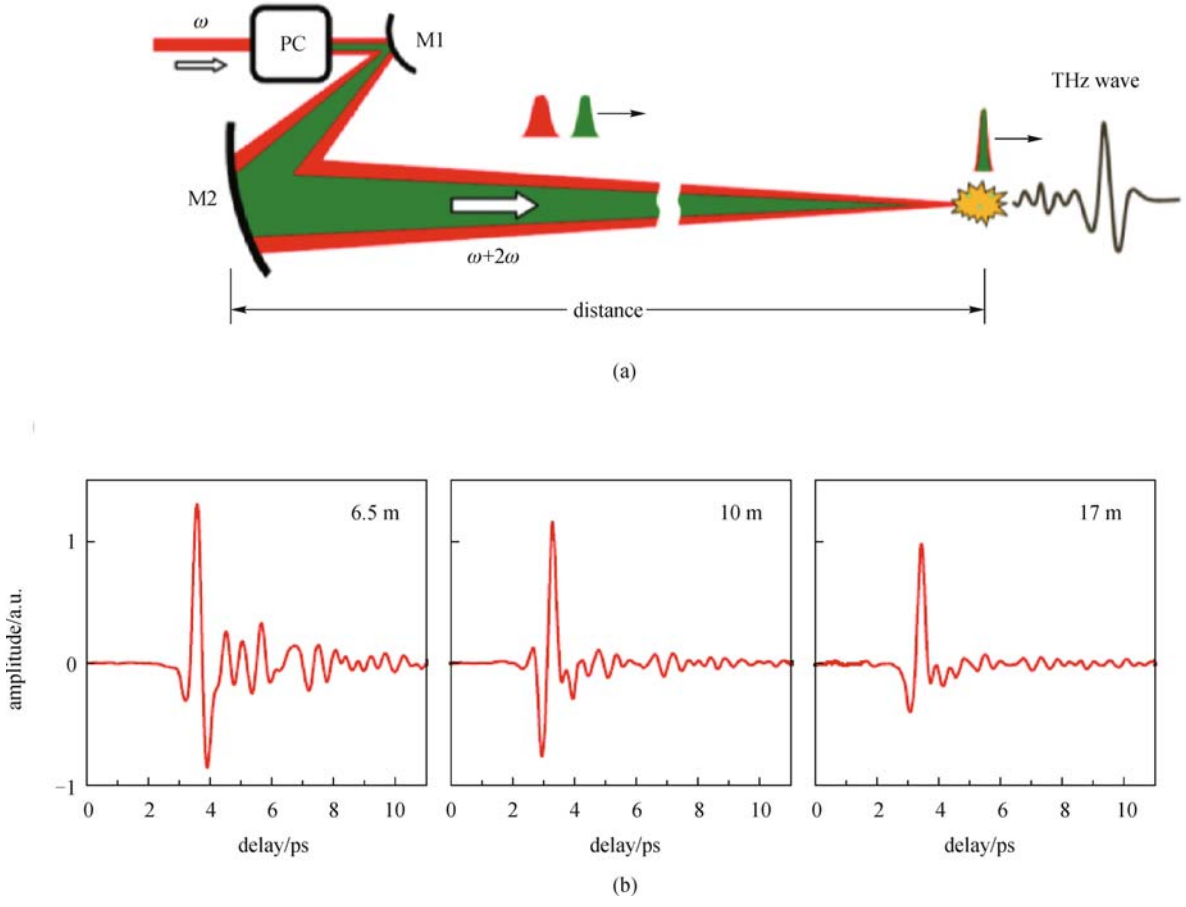


**Fig. 6** (a) Schematic of the experimental setup for remote THz wave generation from laser-induced plasma in the ambient air. PC, phase compensator; M1, convex spherical mirror used to expand the optical beams; M2, concave spherical mirror used to remotely focus optical beams; (b) THz waveforms generated in ambient air at distances of 6.5, 10 and 17 m respectively. 1 mm thick ZnTe crystal was used as sensor (Courtesy of Jianming Dai)

any on-site detector. The coherent THz detection in this method is achieved through coherent manipulation of the fluorescence emission from two-color laser induced plasma. The combination of this method and the existing long distance THz generation can eventually make the broadband THz remote spectroscopy available.

### 1.3 Overview

This paper seeks to advance the broad goal of discovering new THz physics and developing novel THz applications. This research invokes several disciplines: plasma physics, light-matter interaction, theoretical calculation and modeling, ultrafast optics, and remote sensing.

Along with the introduction and motivation given in this Section, the key contributions of this research will be discussed in detail in following sections and organized as below:

Section 2 provides the theoretical background and experimental verification of the THz-radiation-enhanced-emission-of-fluorescence (THz-REEF).

Section 3 systematically studies the THz-REEF in various noble gases and alkaline gases to reveal the dependence of the fluorescence enhancement on the atomic properties and plasma temperature.

Section 4 starts the investigation of the THz-REEF from two-color excited plasma and introduces a novel "all optical" technique for broadband THz remote sensing through coherently manipulating the fluorescence from asymmetrically biased gases.

Section 5 contributes to the feasibility study of using THz-REEF to diagnose the laser-induced plasma.

Section 6 extends the THz-REEF to the study of semiconductor photoluminescence and introduces a novel method for ultrafast light modulation for light emitting device.

Section 7 summarizes the achievement of each section and draws a final conclusion.

## 2 Terahertz radiation-enhanced-emission-of-fluorescence

In this section, the femtosecond laser-induced air plasma fluorescence under the illumination of single-cycle THz pulses was studied through semi-classical model and experimental verification. The results indicated that time-resolved THz-REEF was dominated by the electron kinetics and electron-impact-excitation of gas molecules/ions. The information of the time-dependent THz field can be recovered from the measured time-resolved THz-REEF from single-color laser induced plasma with the help of the bias as local oscillator. This coherent THz wave detection method was featured by omni-directional emission pattern and can be used for THz time-domain spectroscopy.

### 2.1 Introduction

The interaction between electromagnetic waves and laser-induced gas plasma has been extensively investigated in most of the spectral regions including microwave, visible and X-ray [13–16]. Electric field measurements and plasma dynamics characterization in gas DC and radio-frequency discharge were demonstrated by using laser-induced fluorescence spectroscopy in various schemes [22,27,28]. However, due to the lack of strong and tabletop THz sources and limited access to large scale free electron THz laser, the study in the THz region (0.1 to 10 THz) has long been an existing challenge in the past. Low energy of the THz photon makes THz technology a promising method for *in situ*, non-invasive plasma characterization. Also the large frequency span of THz pulses recently developed encompasses a wide range of plasma densities and allows highly sensitive probing of the photo-ionized gas [29–32]. Recent technical development of intensive THz sources [9,33–35], has offered us new opportunities for the study of plasma inverse-bremsstrahlung heating [17,18] and electron impact molecular excitation [19,20] by THz waves. Here, we studied the interaction between ultrashort THz pulses and single-color laser-induced plasma by measuring REEF. We built a semiclassical model to describe the electron motion in the presence of the THz field and following electron-impact-excitation of gas molecules. The time-dependent plasma response to the THz pulse was calculated as a function of electron collision relaxation time and electron-ion recombination rate. We found the enhanced fluorescence emission is quadratically dependent on the THz field. The experiments were performed at different gas pressures and results agreed with the theoretical calculation, which proved the validity of the theory. Coherent detection of broadband THz waves by measuring THz REEF from air plasma was also demonstrated. Moreover, this method has the feature of omni-directional emission pattern, which distinguishes it from other commonly-used THz detection techniques, such as electro-optical sampling, photo-conductive antenna and air-breakdown-coherent detection [26,36,37],

### 2.2 Theory and modeling

In the field of an ultrashort intense laser pulse, free electrons are rejected from air molecules by the photo-ionization and drift away from their parent ions after acquiring momentum from the rest of the laser pulse. The drift velocity is along the polarization of the laser field. Under the influence of the single-cycle THz pulse radiation, the free electron dynamics in laser-induced plasma are determined by the amplitude and phase of the laser pulse and THz pulse, their delay and gas density. After the passage of the laser pulse, the motion of the elections is dominated by the driving force from THz field

$\vec{E}_{\mathrm{THz}}(t)$ and can be described semiclassically as [15,31]

$$\frac{\mathrm{d}\vec{v}(t)}{\mathrm{d}t}+\frac{\vec{v}(t)}{\tau}=-\frac{e}{m}\vec{E}_{\mathrm{Loc}}(t), \tag{1}$$

where $\vec{v}(t)$ is the electron velocity, $\tau$ is the electron collision relaxation time and $m$ is the electron mass. $\vec{v}(t)/\tau$ is the damping term, which is accountable for the energy transfer from electrons to molecules/ions via collisions. $\vec{E}_{\mathrm{Loc}}(t)$ is the local electric field acting on the charges. $\vec{E}_{\mathrm{Loc}}(t)=\vec{E}_{\mathrm{THz}}(t)-\vec{P}/(2\varepsilon_0)$, where $\vec{P}$ is the space-charge polarization [31]. Here we focus our discussion on the case where the plasma density is low (~$10^{15}\mathrm{cm}^{-3}$ or lower), so that the electronic screening effect on THz field can be neglected and approximation $\vec{E}_{\mathrm{Loc}}\approx\vec{E}_{\mathrm{THz}}$ can be taken. During the THz cycle which is on pico-second time scale, the electron velocity is increased or decreased depending on the transient direction of the THz field and electron velocity. Because the electron velocity distribution is symmetric along laser polarization after the ionization, i.e., $\rho\left(\vec{v}(0)\right)=\rho\left(-\vec{v}(0)\right)$, the average electron kinetic energy is always increased no matter what direction the THz field is pointing.

In laser-induced plasma, besides ions and ground states, there are existing trapped states in the high-lying Rydberg states in atoms and molecules [38]. These trapped states are formed via absorption of multiple photons and have very large quantum numbers, i.e., their energy levels are very close to that of ionized state. Thus these trapped states can be easily ionized via the collision with neighboring energetic electrons. After free electrons are heated by the THz wave, electron-impact ionization of these trapped states produces more ions. Larger $N_2^+$ ion population leads to more UV fluorescence emission from electronic excited state $C^3\Pi_\pi$ of $N_2$ through the formation of $N_4^+$ ($N_2^+ + N_2 \Rightarrow N_4^+$) and the subsequent recombination $N_4^+ + e \Rightarrow N_2(C^3\Pi_\pi) + N_2$ [39]. This eventually results in an enhancement of the fluorescence emission from nitrogen molecules within nanoseconds [39–41]. Therefore, the enhancement of the molecular fluorescence emission provides a direct access to the rich information of electron temperature and population of excited molecular states in the presence of the THz radiation [42]. It is worth noting that the contribution of the THz field tunneling ionization and THz photo-ionization are not expected to dominant here because of the single cycle nature of the THz pulse and small THz photon energy, e.g., 1 THz photon energy is 4.3 meV, which is very small compared to the ionization energy of the high-lying Rydberg states of molecules (typically a few hundred meV) respectively. The validity of this argument will be further supported by the THz-REEF experiments at different gas pressures in Section 2.3.

To understand the time-resolved electron collision dynamics in the THz field, the total fluorescence emission $I_{\mathrm{FL}}(t_{\mathrm{d}})=I_{\mathrm{FL,b}}+\Delta I_{\mathrm{FL}}(t_{\mathrm{d}})$ as a function of the time delay $t_{\mathrm{d}}$ between the THz pulse peak and the laser pulse peak, is calculated based on the theoretical frame mentioned above. Sign of $t_{\mathrm{d}}$ is defined that $t_{\mathrm{d}}>0$ when the THz pulse is ahead of the laser pulse while $t_{\mathrm{d}}<0$ when THz pulse is behind the laser pulse. Here, $I_{\mathrm{FL,b}}$, the background plasma fluorescence emission without the THz field, is directly generated from the laser pulse excitation. The general form of the enhanced fluorescence $\Delta I_{\mathrm{FL}}(t_{\mathrm{d}})$ can be expressed as

$$\Delta I_{\mathrm{FL}}\propto n_{\mathrm{e}}(\beta_{\mathrm{ei}},t_{\mathrm{d}})\left(\sum\nolimits_{i=1}^{\infty}\langle\Delta E_i(\tau,t_{\mathrm{d}})\rangle|_{\vec{E}_{\mathrm{THz}}}-\sum\nolimits_{i=1}^{\infty}\langle\Delta E_i(\tau,t_{\mathrm{d}})\rangle|_{\vec{E}_{\mathrm{THz}=0}}\right), \tag{2}$$

where $\beta_{\mathrm{ei}}$ is the electron-ion recombination rate and $\langle\Delta E_i(\tau,t_{\mathrm{d}})\rangle$ is the average energy which one electron transfers to molecules during $i$th collision at $t_i$. The mean fractional loss of electron kinetic energy in a classical collision, $k$, is $2mM/(m+M)^2$, where $m$ and $M$ are electron and molecule masses. Since the electron mass is much smaller than molecule mass, i.e., $m<<M$, all directions of electron motion after collision are equally probable and energy transfer in each collision is very small, i.e., $k\approx 2m/M<<1$ [43]. Considering the equal scattering angle probability and constant energy transfer ratio, the energy transfer from one electron to molecules is

$$\langle\Delta E_i(\tau,t_{\mathrm{d}})\rangle=\int_{-\infty}^{+\infty}\left(m\vec{v}^2(0)/2+m\,\vec{v}\,\Delta\vec{v}_1\right)k(1-k)^{i-1}\rho\left(\vec{v}(0)\right)\mathrm{d}\,\vec{v}(0)+km\sum\nolimits_{j=1}^{i}\Delta\,\vec{v}_j^{\,2}(1-k)^{i-j}, \tag{3}$$

where $\Delta\vec{v}_i=-\int_{t_i-\tau}^{t_i}e\vec{E}_{\mathrm{THz}}(t)\mathrm{d}t/m$ is the velocity change between the $(i-1)$th collision and $i$th collision. Here the first term accounts for the energy transferred from the initial electron velocity while the second term accounts for the energy transferred from the THz field. Because of the $\rho\left(\vec{v}(0)\right)=\rho\left(-\vec{v}(0)\right)$ symmetry, the integration of $m\,\vec{v}\,\Delta\vec{v}_1\rho\left(\vec{v}(0)\right)$ over $\vec{v}(0)>0$ is cancelled by the integration over $\vec{v}(0)<0$. So the net value of integration $m\,\vec{v}\,\Delta\vec{v}_1\rho\left(\vec{v}(0)\right)$ is equal to zero.

One of the key parameters in Eqs. (2) and (3) is the electron relaxation time $\tau$, since $\tau$ determines how efficiently THz field can accelerate electrons and transfer energy. Figure 7 illustrates the frequent electron-molecule collisions within the THz pulse duration. Dash line refers to the time when the collision event occurs. As gas

pressure $P$ changes, the electron collision relaxation time varies accordingly with a relationship of $\tau(P) = \tau_0 P_0/P$, where $\tau_0$ is the relaxation time at atmosphere pressure $P_0$ and is typically a few hundred femtoseconds [44]. We will discuss two extreme cases where the gas pressure is very low and very high.

At very low gas pressure, $\tau(P)$ is much longer than THz pulse duration $\tau_{\mathrm{THz}} \sim 1$ ps due to the very large spacing between molecules as shown in Fig. 8(a). In the limit of very large $\tau$, the electron does not experience any collision during the single-cycle of THz pulse and $\Delta I_{\mathrm{FL}}$ can be approximated with $\Delta\vec{v}_1 \neq 0$ and $\Delta\vec{v}_{i>1} = 0$

$$\lim_{\tau >> \tau_{\mathrm{THz}}} \Delta I_{\mathrm{FL}} \propto n_{\mathrm{e}}(\beta_{\mathrm{ei}}, t_{\mathrm{d}}) \frac{e^2}{2m} \left( \int_{t_{\mathrm{d}}+t_\varphi}^{\infty} \vec{E}_{\mathrm{THz}}(t)\mathrm{d}t \right)^2$$

$$\propto \vec{A}^2 (t_{\mathrm{d}} + t_\varphi). \tag{4}$$

Here $\vec{E}_{\mathrm{THz}}(0) = \vec{E}_{\mathrm{peak}} \cdot t_\varphi$ is the phase delay caused by the plasma formation dynamics at the early stage. Therefore, at low pressure the $\Delta I_{\mathrm{FL}}$ is proportional to the square of the vector potential of the THz pulse at $t_{\mathrm{d}} + t_\varphi$.

At very high gas pressure, $\tau(P)$ is much shorter than THz pulse duration and the electron collides with molecules so frequently that $\vec{E}_{\mathrm{THz}}(t)$ can be considered nearly constant between neighboring collisions as shown in Fig. 8(b). Therefore, $\Delta I_{\mathrm{FL}}$ can be approximated as

$$\lim_{\tau << \tau_{\mathrm{THz}}} \Delta I_{\mathrm{FL}} \propto n_{\mathrm{e}}(\beta_{\mathrm{ei}}, t_{\mathrm{d}}) \frac{e^2 \tau}{2m} \int_{t_{\mathrm{d}}+t_\varphi}^{+\infty} \vec{E}_{\mathrm{THz}}^2(t)\mathrm{d}t. \tag{5}$$

Above equation indicates that at high pressure, $\Delta I_{\mathrm{FL}}$ is proportional to the time integral of the THz field squared, i.e., THz pulse energy.

In both cases of very high and low pressure, the fluorescence enhancement $\Delta I_{\mathrm{FL}}$ is a function of the time-dependent THz field. Therefore one is able to recover the critical information of the THz time-domain waveform by measuring time-resolved THz-REEF.

### 2.3 Experimental verification

To verify the semiclassical model described above, we experimentally investigated the influence of the single-cycle THz pulse radiation on the plasma. Figure 9 shows the schematic of the experimental layout.

A lithium niobate ($LiNbO_3$) prism is as THz emitter via the optical rectification. The tilted pulse front scheme [34] is (used) as guarantee the phase match between THz phase velocity and optical group velocity. To achieve tilted pulse front in the $LiNbO_3$ crystal, a 2000 lines/mm, gold-coated optical grating is used for spatially chirping the incident laser beam. The spatially chirped laser beam is refocused onto the prism by a lens with effective focal length of the 62 mm. A broadband, single-cycle THz pulse with linear polarization and a peak field of 100 kV/cm is output from

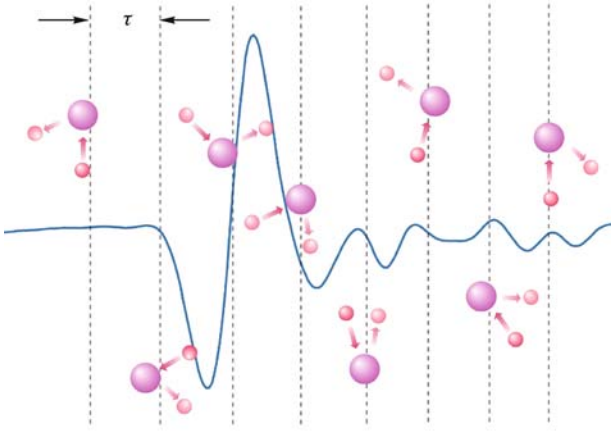


**Fig. 7** Illustration of the frequent electron-molecules collisions within THz pulse duration. Small circles are electrons and big circles are molecules. Arrow represents the direction of electron motion

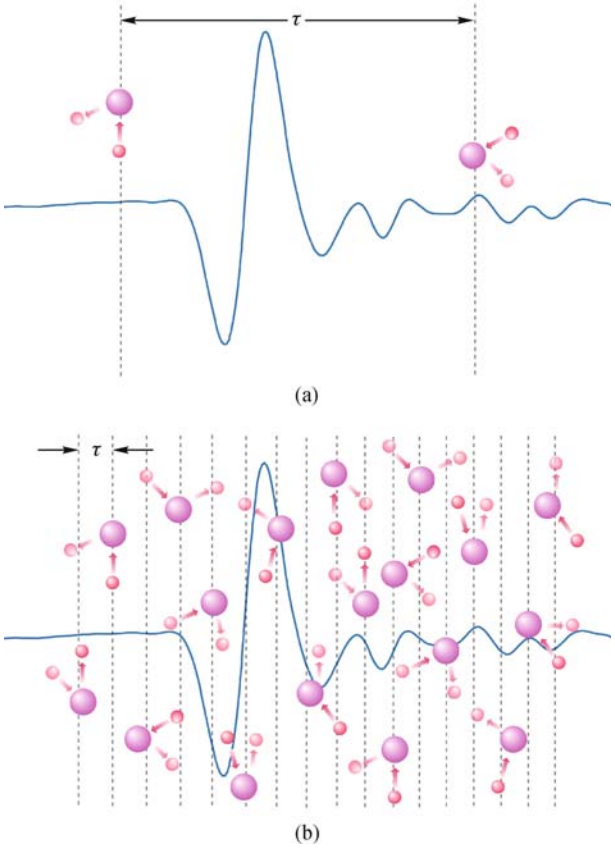


**Fig. 8** Illustration of the frequency of the electron-molecules collisions within the THz pulse duration (a) at extreme low pressure and (b) at extreme high pressure

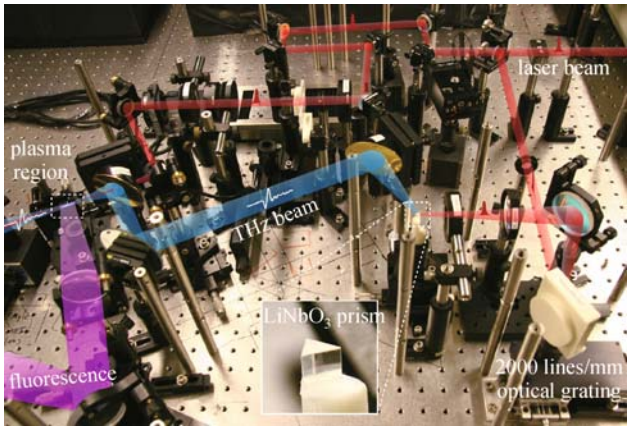


**Fig. 9** Schematic of THz-REEF experiment. Red beam is 800 nm laser. Blue beam is the THz generated from the $LiNbO_3$ prism. Purple beam is the fluorescence emission from the laser-induced plasma. Inset, the enlarged image of the $LiNbO_3$ prism

the $LiNbO_3$ prism and is then focused into a plasma region that is formed by focusing a 100 μJ femtosecond laser pulse with a center wavelength of 800 nm and pulse duration of 80 fs. The laser pulses propagate collinearly with the THz pulses. The laser-induced fluorescence is collected by a broadband convex lens and spectrally resolved by a monochromator (HORIBA Jobin Yvon SPEX 500M) and a photo multiplier tube (PMT, Hamamastu R7732-10). The spectral response of the PMT is over the wavelength range of 185 to 900 nm and peaks at 400 nm. As a parallel reference for fluorescence measurement, the THz time-domain waveform was measured by a 300 μm thick <110> Gallium Phosphor (GaP) crystal using electro-optic (EO) sampling [36]. Figure 10(a) shows the schematic of the interaction between the THz pulse and the laser-induced plasma. The image is the optical image of the laser-induced plasma measured by the charged-coupled device (CCD). Circles with positive sign represent the positively charged ions while circles with negative sign represent the negatively charged electrons.

Fluorescence emitted from nitrogen molecules, consisting of 78% ambient air, dominates the air plasma emission. Over 90% of the nitrogen fluorescence comes from the spectral range of 300 to 450 nm, where there are existing several major emission lines such as those from the second positive band system of $N_2$ ($C^3\Pi_u - B^3\Pi_g$ transitions at 337, 353, 357, 375 and 380 nm) and the first negative band system of $N_2^+$ ($B^2\Sigma_u^+ - X^2\Sigma_g^+$ transition at 391 nm) [45]. This is also the spectral window we are mainly interested in. We measured the laser-induced plasma emission spectrum in the spectral range of 320 to 400 nm at different THz field strength and results are shown in Fig. 10(b). Time delay is set as $t_d = -1$ ps. It can be seen that the fluorescence emission from both nitrogen molecules and ions are enhanced by the same factor as THz field is increased.

Figure 10(c) shows that the measured THz field dependence of the total emission $I_{FL}$ at the strongest line 357 nm (solid dots) and the quadratic fit (dashed line) when $t_d = -1$ ps. The fact that the $\Delta I_{FL}$ at all wavelengths is proportional to the THz intensity, agrees with Eq. (4) as high pressure approximation is satisfied at ambient pressure.

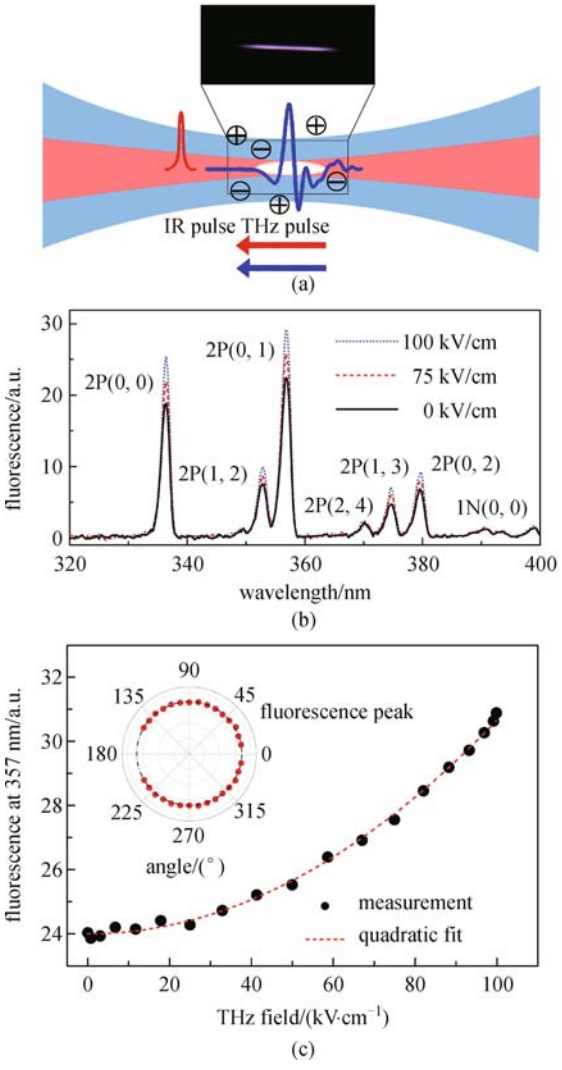


**Fig. 10** (a) Schematics of the interaction between the THz wave and laser-induced plasma; (b) measured fluorescence spectra versus THz field as $t_d = -1$ ps; (c) measured quadratic THz field dependence of 357 nm fluorescence emission line as $t_d = -1$ ps. Inset: The isotropic emission pattern of THz-REEF

The inset of Fig. 10(c) shows the angular pattern of fluorescence emission on the horizontal plane on which the detector is rotated around the plasma while the distance between plasma and detector is kept constant. An isotropic emission profile was observed in the angular range of 10°

to 150°. The absence of data smaller than 10° or larger than 150° is due to the geometric limitation of the experimental setup. The above experimental observations suggest that the THz pulse enhances plasma fluorescence emission through accelerating electron via the inverse-bremsstrahlung process and following energy transfer from hot electrons to air molecules/ions via inelastic collisions.

Figure 11(a) shows the measured time-delay dependence of $\Delta I_{\mathrm{FL}}(t_{\mathrm{d}})$ compared with that of $\vec{E}_{\mathrm{THz}}(t_{\mathrm{d}})$ measured by EO sampling. When the THz pulse (shown as blue pulse) is ahead of the laser pulse (shown as red short pulse) in time, there is no fluorescence enhancement, i.e., $\Delta I_{\mathrm{FL}}(t_{\mathrm{d}} >> 1\ \mathrm{ps}) = 0$, which is the same as that without the THz field present. A rapid increase of fluorescence is seen when two pulses move close enough that the tail of the THz pulse starts to temporally overlap with the laser pulse. The measured slow decrease of the $\Delta I_{\mathrm{FL}}(t_{\mathrm{d}})$ is at the larger negative delay due to the decrease of electron density as electrons recombine with ions. This is confirmed by the agreement with the calculated temporal evolution of electron density $n_{\mathrm{e}}(t) = n_{\mathrm{e}}(0)/\left(1 + n_{\mathrm{e}}(0)\beta_{\mathrm{ei}}t\right)$ [46], where the initial electron density $n_{\mathrm{e}}(0) \sim 10^{16}\mathrm{cm}^{-3}$ by assuming $\beta_{\mathrm{ei}} = 6.1 \times 10^{-12}\ \mathrm{m}^3/\mathrm{s}$ [47]. This $n_{\mathrm{e}}(0)$ might be overestimated here because $\beta_{\mathrm{ei}}$ used here is taken from the data measured at 29 torr and effective $\beta_{\mathrm{ei}}$ at atmospheric pressure is expected to be higher considering larger population of complex ions and larger three body recombination rate. To confirm this, a separate experiment was conducted to measure the plasma density using transmission THz time-domain spectroscopy [31] and plasma density was measured to be in range of $10^{14}$ to $10^{15}\mathrm{cm}^{-3}$. The electron densities in a laser filament were also previously characterized by several groups using various methods [46,48,49].

As the laser pulse is scanned through the THz pulse in time, the enhanced fluorescence shows two-step profile on the rising edge. The width of the rising edge is comparable with the THz pulse duration as shown in the expanded scale in Fig. 11(b). $\Delta I_{\mathrm{FL}}(t_{\mathrm{d}})$ reaches its maximum when the laser pulse temporally overlaps the beginning of the THz pulse. The enhancement ratio $\Delta I_{\mathrm{FL}}(t_{\mathrm{d}})/I_{\mathrm{FL}}(t_{\mathrm{d}})$ is observed to reach as high as 30% with a THz peak field of 100 kV/cm. What is more interesting here is that,we found that the time derivative of the enhanced fluorescence is proportional to the square of the THz field with a constant phase delay, $\mathrm{d}\Delta I_{\mathrm{FL}}(t_{\mathrm{d}})/\mathrm{d}t_{\mathrm{d}} \propto \vec{E}^{\,2}_{\mathrm{THz}}(t_{\mathrm{d}} + t_{\varphi})$. This is not a coincidence but a perfect agreement with the results predicted by Eq. (5) with high pressure approximation. The experimental value of $t_{\varphi}$ is about 100 fs at laser excitation intensity of $10^{13} \sim 10^{14}\ \mathrm{W/cm}^2$. The exact value of the $t_{\varphi}$ might be determined by various parameters such as laser power, THz-laser beam overlap and optical dispersion in plasma, which is beyond the scope of current study.

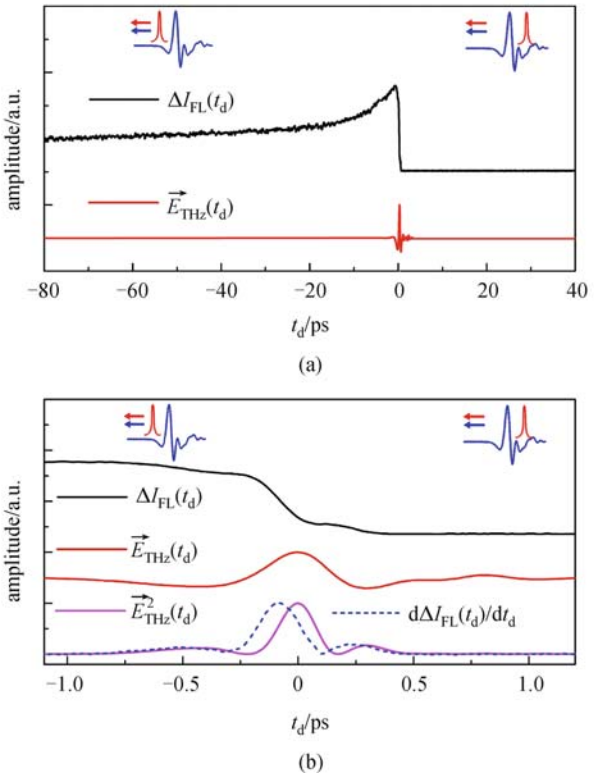


**Fig. 11** (a) Time-resolved THz-REEF $\Delta I_{\mathrm{FL}}(t_{\mathrm{d}})$ and THz field $\vec{E}_{\mathrm{THz}}(t_{\mathrm{d}})$; (b) time-resolved $\Delta I_{\mathrm{FL}}(t_{\mathrm{d}})$, $\vec{E}_{\mathrm{THz}}(t_{\mathrm{d}})$, $\mathrm{d}\Delta I_{\mathrm{FL}}(t_{\mathrm{d}})/\mathrm{d}t_{\mathrm{d}}$ and $\vec{E}^{\,2}_{\mathrm{THZ}}(t_{\mathrm{d}})$ on the rising edge in the expanded scale of (a). All curves are normalized and offset for clarity

To further verify the general calculation of $\Delta I_{\mathrm{FL}}$ in Eq. (2), THz-REEF experiments in pure nitrogen gas were carried out at different gas pressures. The measured $\Delta I_{\mathrm{FL}}(t_{\mathrm{d}})$ at different pressures are shown in Fig. 12(a). In the measurement, the laser excitation intensity remained constant. The $\Delta I_{\mathrm{FL}}(t_{\mathrm{d}})$, which is proportional to the product of $n_{\mathrm{e}}$ and $m\sum_{i=1}^{\infty}\Delta\vec{v}_i^{\,2}$, reaches a maximum at a few hundred torr as $n_{\mathrm{e}}$ monotonically increases with the pressure and $m\sum_{i=1}^{\infty}\Delta\vec{v}_i^{\,2}$ depends on pressure in a more complicated way.

On the slowly falling edge, the decrease of $\Delta I_{\mathrm{FL}}$ with larger negative $t_{\mathrm{d}}$ shows significant pressure dependence. The different decay rates are attributed to the electron density dependence of the electron-ion recombination process [46].

Figures 12(b) and 12(c) show the measured $\Delta I_{\mathrm{FL}}(t_{\mathrm{d}})$ and the calculated $\Delta I_{\mathrm{FL}}(t_{\mathrm{d}})$ from Eq. (2) on the rising edge in the expanded scale, respectively. $\tau_0$ is estimated to be 350 fs [44]. In the calculation at each pressure, $\Delta I_{\mathrm{FL}}(t_{\mathrm{d}})$ is normalized according to the experimental results. At low pressure the $\Delta I_{\mathrm{FL}}(t_{\mathrm{d}})$ shows a spike-like shape as predicted by Eq. (4), while at high pressure the $\Delta I_{\mathrm{FL}}(t_{\mathrm{d}})$ has a two-step profile as predicted by Eq. (4). The agreement between

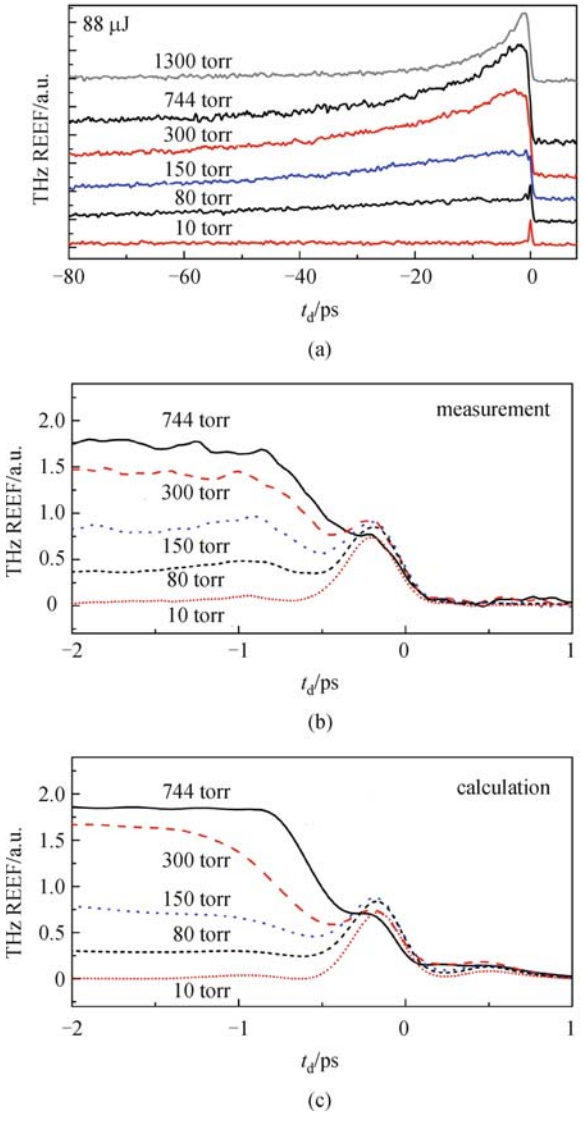


**Fig. 12** THz pulse enhanced fluorescence in nitrogen at a pressure range of 1300 to 10 torr. (a) Measured time-resolved $\Delta I_{FL}(t_d)$ (offset for clarity); (b) expanded scale of the measured time-resolved $\Delta I_{FL}(t_d)$ on the rising edge; (c) calculated time-resolved $\Delta I_{FL}(t_d)$ on the rising edge

the results shown in Figs. 12(b) and 12(c) provides further proof for the proposed mechanism of the THz-REEF.

### 2.4 Coherent THz detection using local bias

As discussed in Sections 2.2 and 2.3, the fluorescence enhancement $\Delta I_{FL}$ linearly depends on $\vec{E}^2_{THz}$ at ambient pressure. Equation (5) provides a method for incoherent THz detection with temporal resolution determined by the ionizing pulse envelope. The coherent detection using REEF is very appealing due to its omni-directional emission pattern and potential for remote THz time-domain spectroscopy. To obtain the phase information of the THz pulse by using REEF, a local oscillator is introduced to the THz-plasma interaction. An external 20 kV/cm AC bias parallel with $\vec{E}_{THz}(t)$ is applied on the plasma to act as a local oscillator $\vec{E}_{LO}$. In this measurement, the fluorescence enhancement is proportional to $\vec{E}^2_{THz}(t) + 2\vec{E}_{LO}\vec{E}_{THz}(t) + \vec{E}^2_{LO}$. The external bias is a square wave switching between positive bias and negative bias at a frequency of 500 Hz which is the half of the repetition frequency of the laser pulse and THz pulse, i.e., 1 kHz. The fluorescence signal from the PMT was measured by a Lock-in Amplifier (LIA) referenced to the 500 Hz bias modulation frequency. Here the contribution of $\vec{E}^2_{LO}$ term to $\Delta I_{FL}$ is modulated at 1 kHz and the contribution of $\vec{E}^2_{THz}(t)$ term to $\Delta I_{FL}$ is not modulated. As a consequence, $\vec{E}^2_{LO}$ and $\vec{E}^2_{THz}(t)$ terms cannot be "picked up" by the LIA. Only the cross term $2\vec{E}_{LO}\vec{E}_{THz}(t)$ whose phase was locked at 500 Hz can be measured by the LIA. Therefore, the fluorescence signal obtained by LIA has the form

$$\Delta I_{FL} \propto \tau \int_{t_d+t_\varphi}^{+\infty} 2\vec{E}_{LO}\vec{E}_{THz}(t)\mathrm{d}t \propto \vec{E}_{LO}\,\vec{A}(t_d + t_\varphi). \quad (6)$$

Therefore, the vector potential of THz waveform can be obtained by the measured time-resolved fluorescence enhancement. Then the time-dependent THz field $\vec{E}_{THz}(t)$ can be retrieved from the derivative of $\vec{A}(t_d)$, with a phase delay $t_\varphi$. Figure 13 shows measured $\vec{A}(t_d)$ and good agreement between the THz waveform calculated from $\mathrm{d}\vec{A}(t_d)/\mathrm{d}t_d$ and that measured by EO sampling. This demonstrates the feasibility of using THz-REEF as a coherent detection method. In Section 4, the broadband THz wave remote sensing using REEF without using the on-site bias will be discussed.

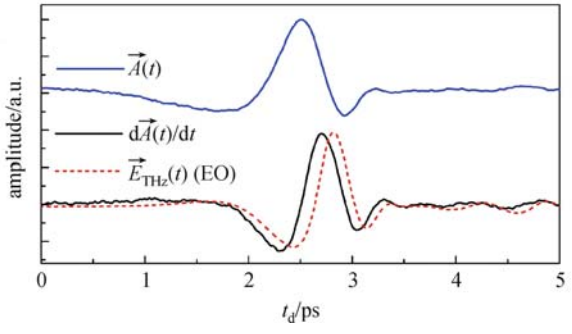


**Fig. 13** Vector potential $\vec{A}(t_d)$ of THz pulse measured by THz REEF and the $\mathrm{d}\vec{A}(t_d)/\mathrm{d}t_d$ compared with THz waveform measured by EO detection

### 2.5 Summary

The interaction between a THz pulse and plasma by investigating THz-REEF from laser-induced gas plasma has been systematically studied. Both theoretical model and experimental investigations show that the electron heating by the THz field and subsequent electron-impact-excitation of gas molecules/ions are key physical processes responsible for the enhancement of the plasma fluorescence under the THz radiation. The time-resolved THz-wave-enhanced fluorescence contains THz waveform information and has been demonstrated to be a method for coherent THz wave detection with the help of a local bias. The demonstrated omni-directional broadband coherent THz wave detection could be potentially extended to other spectral regions.

## 3 Terahertz-pulse-enhanced-fluorescence in gases

In this section, the enhancement of laser-induced fluorescence by intense THz pulses was investigated systematically in selected gases including neon (Ne), argon (Ar), krypton (Kr), xenon (Xe), methane ($CH_4$), ethane ($C_2H_6$), propane ($C_3H_8$), and n-butane ($C_4H_{10}$) gases. The dependences of the enhanced fluorescence on the THz field, laser excitation intensity, gas pressure, and intrinsic atomic properties were experimentally studied. Both narrow line emission and broad continuum emission of noble gas plasma were enhanced by the THz field. Their fluorescence enhancement ratios and time-resolved enhanced fluorescence were largely dependent on the scattering cross section and ionization potential of atoms. Furthermore, the fluorescence emission from various molecular fragments in alkane gas plasma was also found to be enhanced by the THz field.

### 3.1 Introduction

The interaction of the intense laser pulse and gases has attracted a great amount of research interests in the fields of multiphoton ionization [50,51], laser filamentation [52], super continuum [53], high harmonic generation [54,55], and THz wave generation [11,56]. Laser-induced fluorescence in gases has also been widely used as a versatile tool in optical diagnostics of plasma [57]. The laser-induced gas plasma in the presence of a single-cycle THz pulse has recently been studied by measuring the THz-REEF [58]. The study shows that the THz field can effectively increase the electron kinetic energy by driving electrons faster in the plasma and increase electron-impact ionization rate of the high-lying Rdyberg states, which results in the increase of the nitrogen ion population and enhancement of the molecular fluorescence. As stated in Section 2, the THz-REEF can be employed to study the light-plasma interaction in the long wavelength limit as well as coherently detecting THz wave. Despite this initial study in nitrogen plasma, the study of how the electric field oscillating at THz frequency influences laser-induced plasma in different gases is still uncompleted. The roles of atomic/molecular structure and laser intensity in THz-wave-enhanced fluorescence are not also fully understood. Therefore, a more comprehensive study of interaction between the THz pulses and gases plasma would be desired to offer a clearer physical insight in the complex interplay between ultrashort laser pulse ionization, THz-wave-induced electron heating, electron impact ionization, and dissociative recombination. The systematic study presented in this section is also very important for studying the population trapping behavior in noble and alkane gases [59,60], plasma diagnostics [61] and THz wave generation/detection using gaseous [9,11,35,62–65].

In this section, we showed our experimental observation of the enhancement of laser-induced fluorescence from noble gases (Ne, Ar, Kr and Xe) and alkane gases ($CH_4$, $C_2H_6$, $C_3H_8$ and $C_4H_{10}$) by intense THz single-cycle pulses. The reason noble gases were chosen as objects to be studied is that the noble gases are chemically inert and structurally simpler as compared to complex molecules such as diatomic molecules or large molecules. One does not need to take vibrational structures or photoinduced fragmentation into consideration in the data analysis. Thus the simple and well-understood fluorescence spectra make noble gases ideal samples for systematic studies. The enhancement of both narrow spectral line emission and broad continuum emission of noble gas atoms were experimentally observed. We also showed how the dynamics of THz-REEF were correlated with the atomic properties, laser pulse energy and the THz field.

Besides studying the noble gases, we investigated the THz-REEF with alkane gas molecules, which were scientifically interesting because their saturated hydrocarbon structures were major constituents of larger organic molecules, including those of biochemical and radiological significance. Under the irradiation of the intense ultrashort laser pulse, alkane molecules were photodissociated into smaller fragments. The fluorescence from molecular fragments such as $C_2$ and CH in the THz field were measured and its relationships with the laser power and the THz field were studied in details.

### 3.2 Theoretical background

As gas molecules are exposed in the electric field of the intense laser pulse, some electrons in the molecules are excited from the ground states and finally get rejected from the parent molecules, becoming free electrons. At the same time, some other electrons jump from the ground states to the high-lying Rydberg states by absorbing several laser photons and get trapped in those states. These high-lying Rydberg states have very large quantum number and are

very close to the ionic continuum. Therefore they are much "fragile" compared to the ground states and electrons on those states can be easily kicked out of the molecules once the molecules collide with neighboring particles including neutral molecules, electrons and ions. When an external THz field is applied on the laser-induced plasma, free electrons are accelerated and gain extra kinetic energy from the THz wave. After getting "hotter", these energetic electrons collide with other atoms/molecules at larger velocity than that without the THz field. As a consequence, more high-lying Rydberg states are ionized via inelastic collision and more upper states that will transit to lower states by emitting fluorescence photons are formed [58]. The fluorescence enhancement ratio, as an important indicator, represents the magnitude of the overall influence of the THz pulse on the plasma. The detailed characterization and explicit description of the fluorescence enhancement ratio are of great importance for the enhanced understanding of the light-plasma interaction in the THz region. To express fluorescence enhancement ratio in a more quantitative way, the physical processes of the electron heating and energy transfer via electron-atom collision, are mathematically elaborated in detail, following the derivations in Section 2. The average energy transferred from one electron to atoms during the *i*th collision at time $t_i$, is

$$\langle \Delta E_i \rangle = \int_{-\infty}^{+\infty} \left( m\vec{v}^2(0)/2 + m\vec{v}(0)\Delta\vec{v}_1 \right) k(1-k)^{i-1} \rho\left(\vec{v}(0)\right) \mathrm{d}\vec{v}(0) + km\sum_{j=1}^{i} \Delta\vec{v}_j^2 (1-k)^{i-j}, \quad (7)$$

where $m$ and $M$ are electron and atom masses. $k = 2mM/(m+M)^2 << 1$. $\rho\left(\vec{v}(0)\right)$ is the initial electron velocity distribution after photoionization and satisfies the condition $\int_{-\infty}^{+\infty} \rho\left(\vec{v}(0)\right) \mathrm{d}\vec{v}(0) = 1$. $\Delta\vec{v}_i = -\int_{t_i-\tau}^{t_i} e\vec{E}_{\mathrm{THz}}(t)\mathrm{d}t/m$ is the electron velocity change by the THz field during the time period between two neighboring collisions. In the excitation of the multiple-cycle single-color laser pulse, the electron velocity distribution is symmetric, i.e., $\rho\left(\vec{v}(0)\right) = \rho\left(-\vec{v}(0)\right)$. This means that the electrons move in one direction and the other direction along the laser polarization with equal probabilities. Therefore, with this symmetry, the $\langle \Delta E_i \rangle$ can be simplified to

$$\langle \Delta E_i \rangle = m<\vec{v}^2(0)> k(1-k)^{i-1}/2 + km\sum_{j=1}^{i} \Delta\vec{v}_j^2 (1-k)^{i-j}. \quad (8)$$

Here $<\vec{v}^2(0)>$ is the average of the $\vec{v}^2(0)$ over all the electrons. The amount of total energy transferred from one electron to other molecules in all the sequential collisions (occurring at $t_1$,$t_2$,$t_3$...) can be obtained by summing up all of $\langle \Delta E_i \rangle$

$$\Delta E_{\mathrm{total}} = \sum_{i=1}^{\infty} \langle \Delta E_i \rangle = m<\vec{v}^2(0)>/2 + m\sum_{l=1}^{\infty} \Delta\vec{v}_l^2. \quad (9)$$

Here the first term is the initial kinetic energy of electron without the influence of the THz field. This kinetic energy is determined by the laser pulse energy, laser wavelength, pulse duration and ionization potential of atoms. The second term depicts the extra kinetic energy gained from the THz wave and is largely dependent on the THz pulse shape and electron relaxation time or scattering frequency. Based on the expression in Eq. (9), we can further describe the fluorescence enhancement ratio, $I_{\mathrm{FL}}\left(\vec{E}_{\mathrm{THz}}\right)/I_{\mathrm{FL}}(0)$, in following form

$$I_{\mathrm{FL}}\left(\vec{E}_{\mathrm{THz}}\right)/I_{\mathrm{FL}}(0) = \left(I_{\mathrm{MP}} + Cm<\vec{v}^2(0)>/2 + Cm\sum_{l=1}^{\infty} \Delta\vec{v}_l^2\right) / \left(I_{\mathrm{MP}} + Cm<\vec{v}^2(0)>/2\right), \quad (10)$$

where $I_{\mathrm{FL}}(0)$ is the fluorescence emission when the THz field is zero and totally determined by the laser pulse and gas properties. $I_{\mathrm{FL}}(0)$ includes the collision-induced fluorescence emission ($\propto m<\vec{v}^2(0)>/2$) and transition from upper-states which are directly excited by absorbing multiple photons, $I_{\mathrm{MP}}$. $C$ is a constant that represents the impact excitation efficiency. It can be seen that the enhancement ratio largely depends on $\sum_{l=1}^{\infty} \Delta\vec{v}_l^2 / <\vec{v}^2(0)>$ especially. In the following sections, we will experimentally characterize this ratio by varying the laser power and gas species.

### 3.3 Experimental setup

Figure 14 illustrates the experiment of the THz-REEF in gases. A tabletop Ti:sapphire regenerative amplifier generates ultrashort laser pulses with 80 fs pulse duration, 600 μJ pulse energy, 1 kHz repetition rate, and 800 nm central wavelength. The output laser pulse is split into two by a 70/30 beam splitter. Larger portion, i.e., 70%, of the pulse energy is illuminated onto the $LiNbO_3$ prism to generate strong THz radiation using the scheme of the tilted pulse front excitation [66]. In this THz pulse generation scheme, the phase front of laser pulse is spatially tilted by an optical grating (gold coated and 2000

lines/mm). This maneuver allows the perfect match between the phase velocity of the THz wave and group velocity of the laser pulse inside the $LiNbO_3$ crystal. The combination of the good phase match and large nonlinear optical coefficients $\chi^{(2)}$ of $LiNbO_3$ promises the high energy conversion efficiency and intense THz pulse generation. The total efficiency of the THz generation through the optical rectification process can reach as high as $10^{-3}$, calculated as output THz pulse energy divided by the input laser pulse energy. The emitted intense single cycle THz pulses has (100±2) kV/cm peak field and 1~2 ps pulse duration.

The laser beam with smaller portion of the pulse energy, the other 30% of total energy, is focused by a convex lens with 25 mm diameter and 100 mm effective focal length to into a gas cell. The energy of the laser pulse is tunable by rotating two neutral attenuators. The optical intensity at the focus varies correspondingly in the range of $10^{13}$ ~ $10^{14}$ W/cm$^2$. When the optical intensity is above the ionization threshold of gases, laser plasma is created in cell and emits fluorescence. The windows used on the gas cell are 1 mm thick quartz plates which transmit both the THz wave and fluorescence in the range of ultraviolet to infrared. To guarantee maximal temporal and spatial interaction, the optical pulses and the THz pulse are collinearly focused into the plasma region. The time delay between the THz pulse and laser pulse can be continuously changed by a motorized translation stage. The sign of the time delay is defined as positive when the peak of THz pulse is ahead of the laser pulse in time. A gas inlet and a vacuum pump are used to control the gas pressure and switch the gas species in the cell. The fluorescence emissions from gas plasma are collected by a broadband convex focusing lens with 50 mm diameter, and refocused to the entrance slit of a monochromator (HORIBA Jobin YvonSPEX 500M). On the exit slit side, a sensitive PMT is used to detect the spectrally resolved fluorescence intensity. The amplitude of the THz field, $E_{THz}$, is controlled by rotating two metal wire THz polarizers located in the path of the THz beam.

### 3.4 Fluorescence enhancement in noble gases

The atomic properties of noble gas atoms, such as atomic spectra, ionization potential and scattering cross section, are relatively simple and well-studied. These characteristics make them ideal testbeds for systematic research of THz-REEF. This study is intent to draw more definitive conclusion on the roles of the photoionization, electron heating, impact ionization and electronic transition. Selected gas media are Ne, Ar, Kr and Xe specifically. The ionization potentials of Ne, Ar, Kr, and Xe are 21.6, 15.8, 14 and 12.1 eV, respectively. The reason that helium (He) has not been studied here is that the ionization potential of He atom, i.e., 24.6 eV, is so high that the ionization rate is not appreciable at the laser intensity used here ($10^{13}$ ~ $10^{14}$ W/cm$^2$). When maximal laser energy 140 μJ was used to ionize Ne, Ar, Kr and Xe gases at atmospheric pressure, significant ionization occurred and was accompanied by the appearance of the visible plasma.

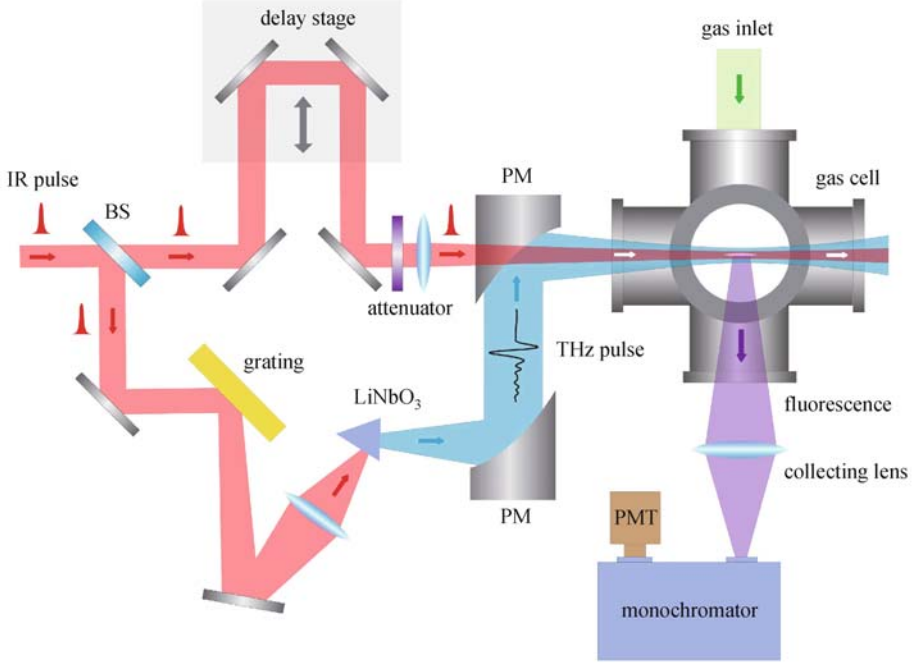


**Fig. 14** Experimental setup of THz-REEF in gases. BS, beam splitter; PM, parabolic mirror; PMT, photo multiplier tube

The main objective of this study is to investigate the dependence of fluorescence emission on pulse energy, THz field strength and gas species. In the measurements in Sections 3.4.1 to 3.4.4, the THz pulse is temporally delayed behind the laser pulse so that the plasma is influenced by the entire THz pulse. In the measurement in Section 3.4.5, the time delay between the THz pulse and laser pulse is varied while the fluorescence signal is being recorded.

### 3.4.1 Neon

The Ne fluorescence spectra between 580 and 760 nm at the pressure of 760 torr were measured at different laser pulse energies when the THz beam was blocked so there was no direct interaction between the THz wave and plasma. The spectroscopic results are shown in Fig. 15(a). The broadening of the fluorescence lines here is mainly due to the current instrumental resolution of 1~2 nm rather than stark or pressure broadening. Ne fluorescence becomes significant at the pulse energy larger than 60 μJ. The spectral positions of the measured emission peaks agree well with literature data [67]. All the observed lines are Ne I lines which result from transitions in neutral Ne atom. No obvious Ne II or Ne III line was observed because the photo-emission from excited Ne atoms is much stronger than that from Ne ions at current excitation pulse energy. Ne spectra in the presence of the THz field with pulse energy 100 and 120 μJ are shown in Figs. 15(b) and 15(c) respectively. The emission of all the lines is increased homogeneously with the THz field. The emission intensity is increased by more than a factor of two as THz field is increased from 0 to 100 kV/cm.

As stated in Section 2, the fluorescence enhancement in gas plasma results from the THz-wave-assisted electron heating and subsequent electron impact ionization of the high-lying states. Most of observed lines in this spectral region are from 3p → 3s transitions of Ne atom. This indicates that the increased population of uppers state, i.e., 3p states, gives raise to the fluorescence enhancement. One possible mechanism responsible for the increase of 3p states population is that the electron impact turn more high-lying states into ions and then more excited states A* are populated through ion conversion $A + A^+ + A \rightarrow A_2^+ + A$ and dissociative recombination $A_2^+ + e \rightarrow A + A^*$ [68,69]. A = {Ne, Ar, Kr, Xe} is used as a symbol of one of these atoms for convenience. Here $A_2^+$ is a molecular ion. Populated excited states A* is 2p state for Ne specifically.

Figure 16(a) shows the laser pulse energy dependence of the Ne fluorescence line at 702 nm in the THz field. This line is assigned to $2s^22p^5(^2P^0_{3/2})3p \rightarrow 2s^22p^5(^2P^0_{1/2})3s$ transition. As the pulse energy increases, the background fluorescence $I_{FL}$(0 kV/cm) increases so does the enhanced fluorescence, i.e., $I_{FL}$(100 kV/cm) − $I_{FL}$(0 kV/cm). The relative enhancement ratio versus pulse energy is plotted in Fig. 16(b). The enhancement ratio is nearly constant from 60 to 120 μJ.

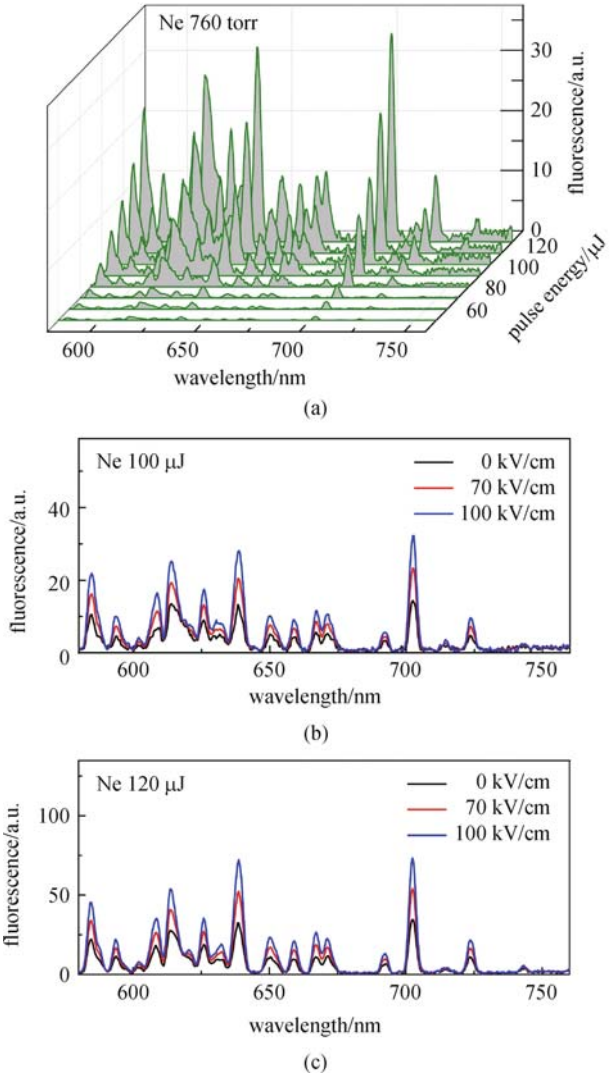


**Fig. 15** (a) Ne fluorescence spectra between 580 and 760 nm at different laser pulse energies (without THz field). The Ne fluorescence spectra at the laser pulse energies of (b) 100 and (c) 120 μJ in the THz field

### 3.4.2 Argon

Figure 17(a) shows the Ar fluorescence spectra between 680 and 780 nm measured at different laser pulse energies. The gas pressure in cell is 760 torr. All the lines observed in this region are from 4p → 4s transition of Ar atom and are increased by the THz field homogeneously. The THz field dependence of Ar spectra were measured at pulse energies of 80, 100 and 140 μJ respectively as shown in Figs. 17(b) – 17(d). The pulse energy dependences of strongest Ar I line at 763 nm and its relative enhancement ratio, are plotted in Figs. 18(a) and 18(b). The enhancement ratios vary with pulse energy and are 124%, 123%,

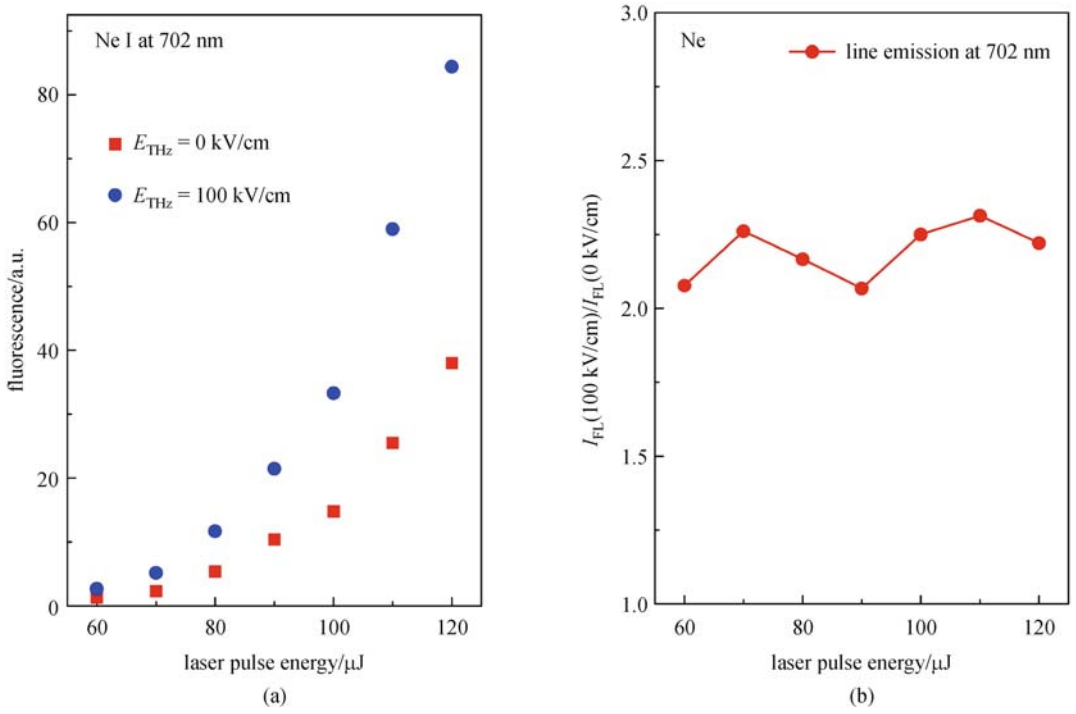


**Fig. 16** Laser pulse energy dependence of (a) absolute emission intensity and (b) enhancement ratio of Ne 702 nm line in the THz field

and 110% respectively at above energies. The smaller enhancement ratio at 140 μJ is due to the larger initial electron velocity and larger electronic screening of the THz field in the denser plasma.

In the comparison between Figs. 18 and 16, it can be noticed that the enhancement ratio $I_{FL}\left(\vec{E}_{THz}\right)/I_{FL}(0)$ of Ar fluorescence is much smaller than that of Ne under the same condition, e.g., the same pulse energy, THz field and gas pressure. According to Eq. (10), the larger enhancement ratio in Ne can be mainly attributed to the smaller $\vec{v}(0)$ in Ne whose ionization potential is higher.

### 3.4.3 Krypton

As shown in Fig. 19(a), the fluorescence spectra of Kr in the wavelength region of 820 to 900 nm were measured at different excitation pulse energies at 760 torr when no THz radiation is incident on the Kr gas plasma. The observed larger line emission and continuum emission of Kr than those of Ne and Ar, were because of the lower ionization potential. The line emission results from bound-bound transition while the continuum emission results from free-bound and free-free transition. Figures 19(b) – 19(d) show the THz field dependence of the emission spectra between 750 and 890 nm at pulse energies of 60, 70, and 90 μJ respectively. The huge background signal in the shadow area is due to the scattering of the laser beam.

As shown in Figs. 20(a) and 20(b), the pulse energy and THz field dependence of the line emission at 759 nm and continuum emission were characterized. Figure 20(c) plots the enhancement ratios for the line emission and continuum emission. The line emission enhancement is induced by THz wave in the similar way as that in Ne whereas the continuum emission enhancement is attributed to the increased electron-ion radiative recombination resulting from the THz-wave-assisted electron-impact ionization and thus larger free electrons density.

Both enhancement ratios decrease with the pulse energy and get close to 1 at 120 μJ. This means the fluorescence enhancement is saturated at the high pulse energy and the THz-wave-enhanced fluorescence is negligible compared to the background fluorescence, i.e., $\sum_{l=1}^{\infty}\Delta\vec{v}_l^{\,2}/<\vec{v}^{\,2}(0)>\ll 1$. The difference between line enhancement ratio and continuum enhancement ratio is possibly due to the different transition channels or/and different fluorescence life times of the line emission and continuum emission.

### 3.4.4 Xenon

Figure 21(a) shows the Xe fluorescence spectra at different laser pulse energies without any THz field presented in the plasma. Figures 21(b)–21(d) show fluorescence spectra in the THz field at laser pulse energies of 40, 50, and 80 μJ.

As shown in Figs. 22(a) and 22(b), the intensity of Xe I 823 nm line emisison resulting from $5s^25p^5(^2P^0_{3/2})6p \rightarrow 5s^25p^5(^2P^0_{3/2})6s$ transition [70] and continuum emission,

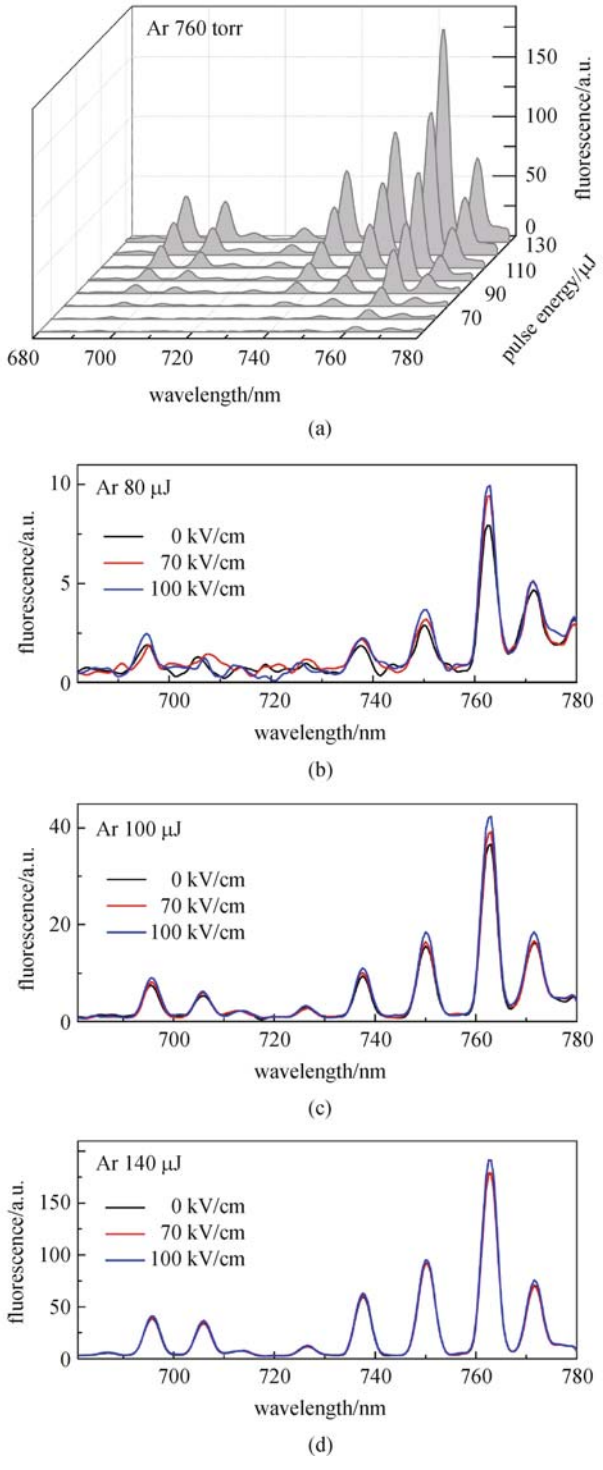


**Fig. 17** (a) Ar fluorescence spectra between 680 and 780 nm at different laser pulse energies (without THz field). The Ar fluorescence spectra at laser pulse energies of (b) 80, (c) 100, and (d) 140 μJ in the THz field

were measured at the pulse energy range of 30 to 130 μJ. The enhancement ratios of both are plotted in Fig. 22(c). Compared to that of Kr, the enhancement saturates at lower pulse energies. The smaller threshold of saturation region in Xe (80 μJ) than that in Kr (120 μJ) is mainly because of the larger screening effect which reduces the effective electric field in the plasma, and higher electron temperature in Xe plasma which reduces the relative enhancement ratio.

### 3.4.5 Time-resolved fluorescence enhancement

To study the correlation between the time-resolved THz-REEF and atomic properties, e.g., ionization potential and scattering cross section, we measured the enhanced fluorescence in Ar, Kr, and Xe at the same excitation power and same pressure as the time delay between the THz pulse and laser pulse is changed. As is shown in Fig. 23, the shape of the time-resolved THz-REEF varies significantly from Ar to Xe at 30 torr.

The key factor which determines this shape variation is the electron relaxation time. On the one side, the "spike shape" observed in Ar can be attributed to the long relaxation time which is much longer than the THz pulse duration. On the other hand, the "two step stairs" shape observed in Xe plasma is because the relaxation time is much shorter than the THz pulse duration. Actually the relaxation time can be retrieved by fitting the measured time-resolved THz-REEF with Eq. (9). The fitted relaxation times for Ar, Kr and Xe are (4±0.3) ps, (1.3±0.14) ps, and (0.4±0.04) ps respectively. This also suggests that THz-REEF could be used for plasma diagnostics, which will be further discussed in Section 5.

These different electron relaxation times in three gases are attributed to different ionization potential and scattering cross section of Ar, Kr and Xe atoms. The electron relaxation time can be expressed as $\tau = 1/(\sigma v_e N_s)$, where $v_e$ is the average electron velocity and $N_s$ is the scatter density which is proportional to gas pressure [61]. The electron velocity $\vec{v}(0)$ is higher in the tunneling ionization of the atoms with lower ionization potential. Also the scattering cross section increases from Ar to Xe. Therefore, the larger electron velocity and bigger scattering cross section result in the shortest electron relaxation time in Xe plasma.

## 3.5 Fluorescence enhancement in alkane gases

The experiment of the THz-wave-enhanced fluorescence was also performed in several linear alkane gases including $CH_4$, $C_2H_6$, $C_3H_8$, and $C_4H_{10}$, whose ionization potentials are very low (12.6, 11.5, 10.95, and 10.55 eV) [71,72]. Relatively low laser pulse energy and low gas pressure were used in order to reduce the electronic screening effect at high plasma density ($>10^{16}$ cm$^{-3}$, corresponding plasma frequency is $>1$ THz). Alkane gas molecules are broken into small fragments such as CH and $C_2$ by intense laser field via photodissociation. Then THz pulse that is delayed after the laser pulse, would affect the dynamics of these molecular fragments in the plasma.

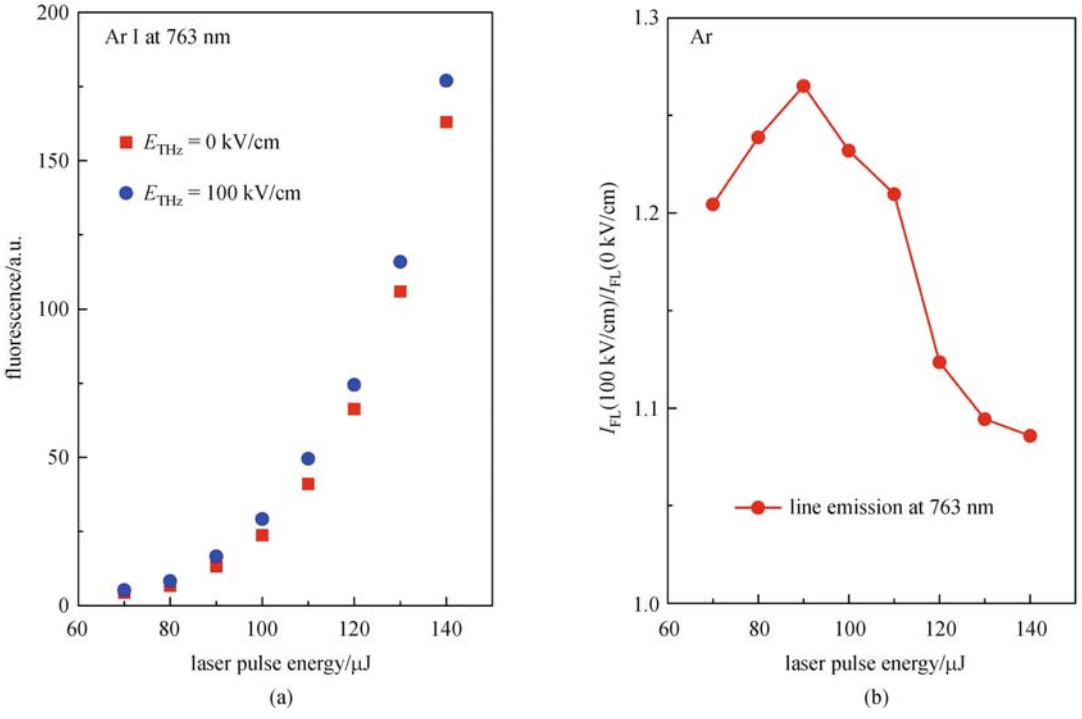


**Fig. 18** Pulse energy dependence of (a) absolute emission intensity and (b) relative enhancement of Ar 763 nm line in the THz field

The fluorescence spectra of $CH_4$, $C_2H_6$, $C_3H_8$ and $C_4H_{10}$ measured in the THz field were shown Fig. 24. Both of CH radical (labeled in red) and $C_2$ Swan band (labeled in blue) fluorescence were observed in all alkane gases except only CH radical fluorescence was observed in $CH_4$. The emission line at 431 nm is assigned to $A^2\Delta \rightarrow X^2\Pi$ transition of CH radical. The emission lines at 437, 473, 516, and 563 nm are assigned to the $v = -2, 1, 0, -1$ progressions of the $C_2$ Swan bands ($d^3\Pi_g \rightarrow a^3\Pi_u$) respectively [73]. Figure 24 shows that both of CH and $C_2$ fluorescence were enhanced by the THz field but by different factors. When a THz pulse with 100 kV/cm peak field is applied, the enhancement ratio of $C_2$ fluorescence is around 20% whereas enhancement ratio of CH fluorescence is 11% in $C_3H_8$ at 5 torr. The mechanism for this different enhancement ratio is not very clear currently. These ratios are different possibly because that THz-wave-assisted electron-impact affects the formation and excitation processes of CH and $C_2$ differently.

### 3.6 Summary

The theoretical and experimental investigations of the enhancement of laser-induced fluorescence by intense THz pulses have been performed in noble gases and alkane gases. Both narrow line emission from atom or molecular fragments and broad plasma continuum emission can be enhanced by the THz field. The experiment with all the gases tested show that the THz-REEF can be considered a "universal" phenomenon that occurs in the light-matter interaction in THz spectral region. The possible channel for formation of fluorescence upper states in noble gases is through the ion conversion $A + A^+ + A \rightarrow A_2^+ + A$ and dissociative recombination $A_2^+ + e \rightarrow A + A^*$. The dependences of fluorescence enhancement on laser pulse energy, THz field, and gas species were experimentally characterized. The enhancement ratio is also found to be highly dependent on the initial electron velocity and electron acceleration in the THz field, which agrees with the theory. Besides offering enhanced understanding of the light-plasma interaction in long wavelength limit, this study introduces the potential applications in broadband THz wave remote sensing and plasma diagnostics.

## 4 Broaband remote terahertz sensing

In this section, we reported an "all-optical" technique of broadband THz wave detection by coherently manipulating the fluorescence emission from asymmetrically ionized gas plasma that interacts with THz waves. Owing to the high atmospheric transparency and omni-directional emission pattern of fluorescence, this technique can be used to coherently measure THz pulses at standoff distances with minimal water vapor absorption and unlimited directionality for optical signal collection. Coherent THz wave detection at a distance of 10 m has been demonstrated.

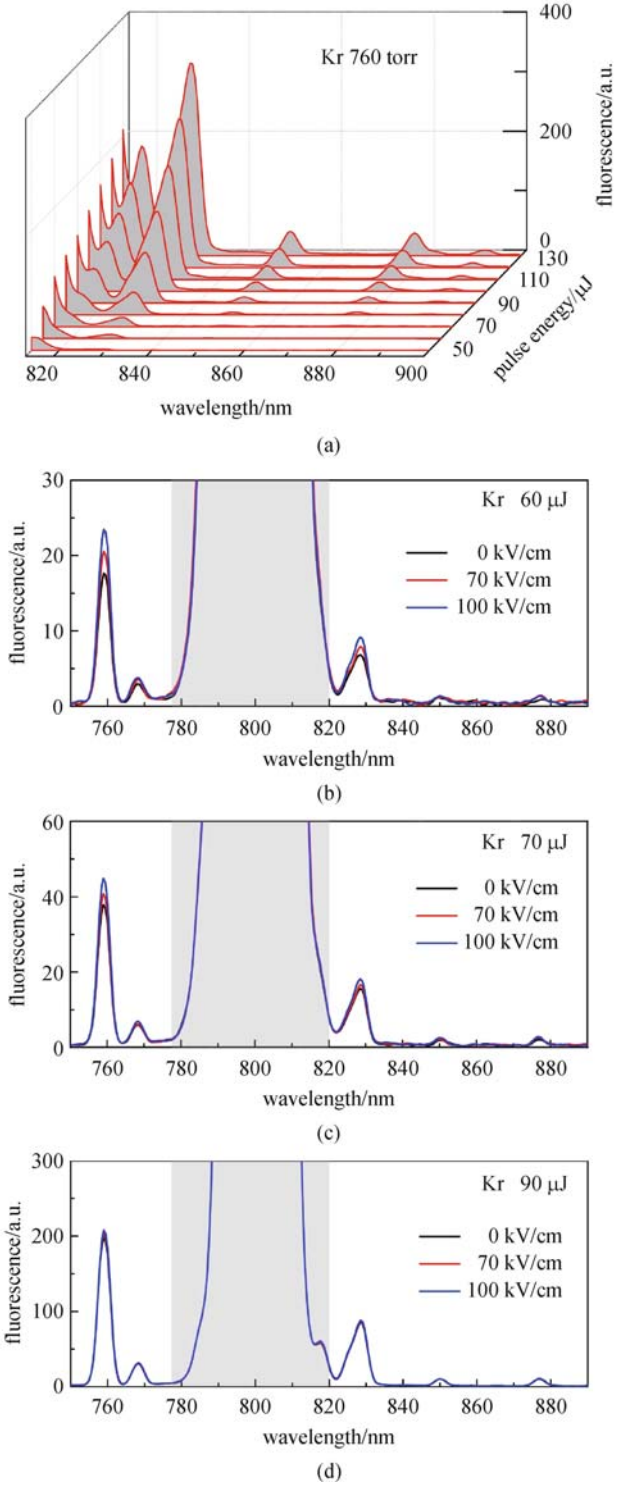


**Fig. 19** (a) Kr fluorescence spectra between 820 and 900 nm at different laser pulse energies (without THz field). The Kr fluorescence spectra at laser pulse energies of (b) 60, (c) 70 and (d) 90 μJ in the THz field

### 4.1 Introduction

THz wave sensing and imaging have received extensive attention due to their significant scientific and technological potential in multi-disciplinary fields [1,5,74]. Due to the challenge of high ambient moisture absorption, the development of remote open-air broadband THz spectroscopy technology is lagging behind the compelling need that exists in homeland security, astronomy and environmental monitoring [5,75]. Photo-conductive antennas, electro-optic (EO) sampling, and THz air detection [7,8,26] have been widely used in the past decades for detection of broadband THz radiation in an increasing variety of applications such as bio-medical imaging, non-destructive inspection, and material characterization. In attempts to meet the emerging needs in homeland security and environmental science, a great amount of research effort has been witnessed in developing broadband remote THz spectroscopy. Remote THz wave generation has been demonstrated by focusing two-color optical beams remotely [25]. However, realization of broadband THz remote sensing is even more challenging. This is because the strong absorption of ambient water vapor in the THz band prohibits long distance THz wave propagation, and the remote optical signal collection at backward direction is also rather difficult. Nearly all the conventional THz detection methods fall short in at least one of these aspects. For photo-conductive antenna, the requirement for an on-site bias makes remote sensing impractical. For electro-optical sampling, on-site crystal and forward collection of optical signal hinders remote operation. For THz detection using air-breakdown-coherent-detection, second harmonic beam generated from four-wave-mixing process has to be measured in the forward direction, which inevitably prohibits remote sensing.

THz-REEF from gas plasma excited by single-color, multi-cycle laser pulses, has been studied and demonstrated for THz wave detection but the phase information of the THz pulse is lost and thus it cannot be used for remote sensing [58]. To achieve standoff broadband coherent THz wave detection, we introduce an ‘all-optical’ technique by probing the THz pulse with fully controllable two-color laser-induced gas plasma and analyzing the THz-REEF. The high transparency of UV fluorescence in the atmosphere can circumvent the sensing distance limitation due to strong water vapor absorption in the THz region. The omni-directional emission pattern of fluorescence enables one to detect signal in the backward direction which is necessary for remote sensing. Instead of being used for THz wave generation as demonstrated in reference paper [76], the two-color laser field functions as a remote ‘optical modulator’ for the THz-REEF through controlling electron momentum and directly measuring THz field. By utilizing this technique we have realized the detection of broadband THz radiation at a distance of 10 m [77].

### 4.2 Method using two-color laser excited plasma fluorescence

The schematics of experiments on THz wave remote

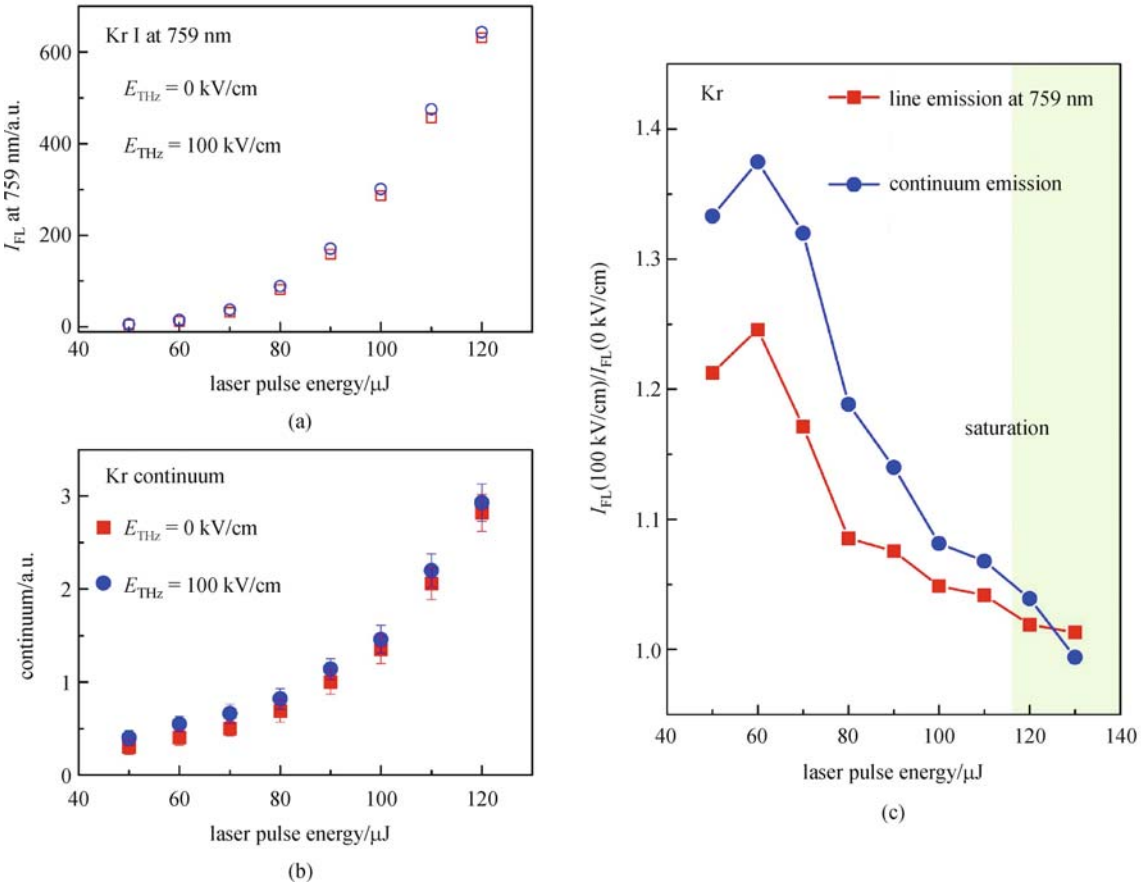


**Fig. 20** Pulse energy dependence of (a) 759 nm line and (b) continuum emission in Kr plasma in the THz field; (c) pulse energy dependence of the enhancement ratio in the THz field. The shadow area is the enhancement saturation region

sensing utilizing coherent manipulation of THz-wave-enhanced fluorescence from asymmetrically ionized gas is shown in Fig. 25. The plasma is created by focusing two-color laser beam into air. A superposition of a linearly polarized fundamental pulse $E_\omega$ and its second harmonic pulse $E_{2\omega}$ is created by propagating a 80 fs, 100 μJ, 800 nm laser pulse through a 250 μm type-I beta-barium borate (β-BBO). The two optical intensities at the focus are $I_\omega (= 10^{13} \sim 10^{14}\ \mathrm{W/cm^2})$ for the fundamental beam, and $I_{2\omega} (= I_\omega/10)$ for the second harmonic beam, respectively. If $E_\omega$ and $E_{2\omega}$ are aligned parallel, the combined optical field $E_{\mathrm{Opt}}$ can be expressed as

$$E_{\mathrm{Opt}}(t) = E_\omega(t) + E_{2\omega}(t) = A_{\omega 0}(t)\cos(\omega t) + A_{2\omega 0}(t)\cos(2\omega t + \phi_{\omega,2\omega}), \quad (11)$$

where $A_{\omega 0}(t)$, $A_{2\omega 0}(t)$ are the envelopes of fundamental (frequency $\omega$) and second harmonic (frequency $2\omega$) pulses, respectively. The relative phase $\phi_{\omega,2\omega}$ is controlled by an in-line phase compensator consisting of an alpha-barium borate (α-BBO) time plate, a pair of fused silica wedges, and a dual wavelength plate (DWP, Alphalas GMBH), with attosecond phase-control accuracy [76]. The polarization of $E_\omega$ and $E_{2\omega}$ can be controlled by DWP. Figure 26 shows the photo image of the phase compensator.

As a demonstration of THz wave remote sensing, a single-cycle THz pulse $\vec{E}_{\mathrm{THz}}(t)$ with 100 kV/cm peak field was generated locally from a $LiNbO_3$ prism using an optical pulse with a tilted pulse-front as the excitation [34] and was focused collinearly with the optical beam onto the plasma. The dashed area in Fig. 25 shows the fluorescence detection system with translational mobility on a horizontal plane. The fluorescence emitted from the two-color laser-induced plasma is collected at a distance by a rotatable UV concave mirror (M1) with 200 mm diameter and 500 mm focal length. The maximal distance between detection system and plasma can be up to 10 m in the laboratory. Another UV plane mirror (M2) with 75 mm diameter is used to reflect the fluorescence beam to the entrance slit of the monochromator. The reflectivity of the UV mirror is greater than 86% in the wavelength range of

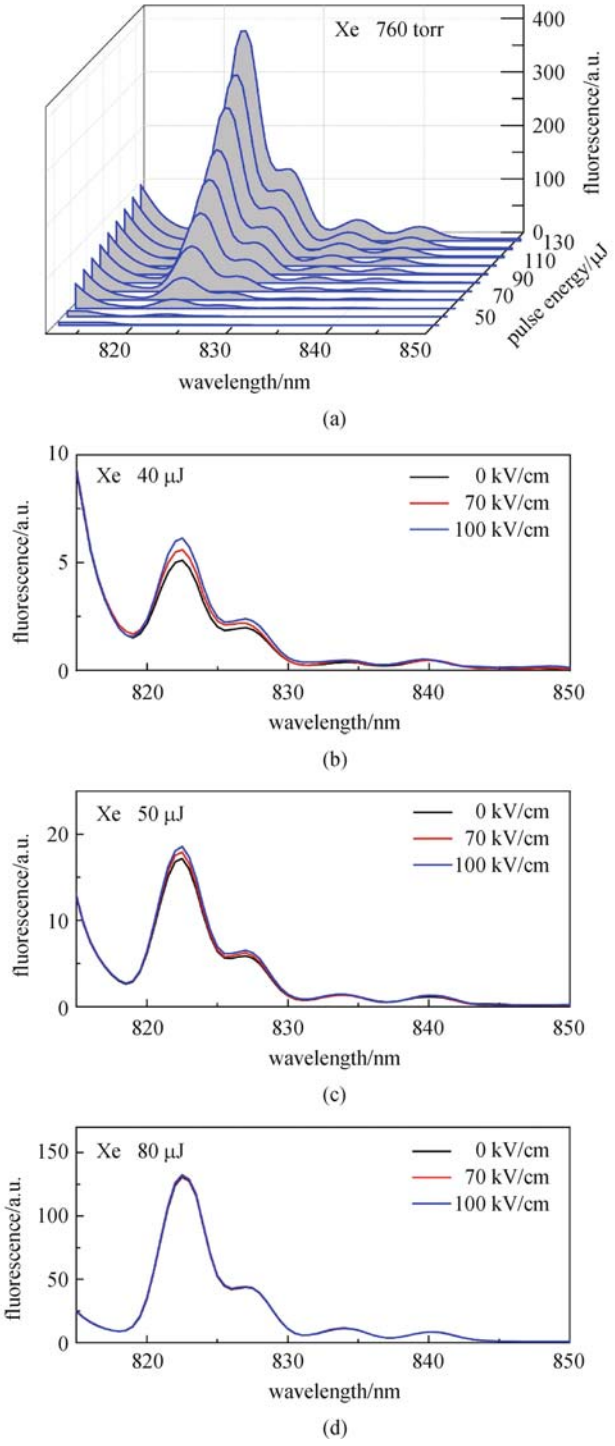


**Fig. 21** (a) Xe fluorescence spectra between 810 and 850 nm at different laser pulse energies (without THz field). The fluorescence spectra at laser pulse energies of (b) 40, (c) 50, and (d) 80 μJ in the THz field

200 to 400 nm. The fluorescence is measured by a photomultiplier tube (PMT) located at the exit of the monochromator. THz wave sensing was performed as the distance between plasma and fluorescence detection system was varied.

### 4.3 THz-wave-assisted impact ionization

In the laser-field-induced ionization processes, electrons newly released from molecules or atoms acquire a constant drift velocity after passage of the laser pulse and the drift velocity is determined by the time when the electron is born [78]. Residual-current density or asymmetric electron velocity distribution could remain in the plasma, ionized by single-color few-cycle pulses [79] or by two-color fields with optimized relative phase [11,80]. Under irradiation of intense laser pulses, a portion of the excited electrons are trapped in high-lying states of atoms and molecules. This "population trapping" was initially predicted and later on experimentally observed in molecular and atomic gases [38,60,81,82]. Some experimental observations also indicate the existence of the population trapping in nitrogen molecules. Those trapped states [83,84], have a large principal quantum number ($n \gg 1$). Compared to electrons in the ground state that has high ionization threshold, these trapped states are more easily ionized via the collision with energetic electrons [19,85–87], as illustrated in Fig. 27(a). The interaction of laser-induced plasma with a THz wave leads to an increase in plasma temperature through electron heating in the THz field and subsequent electron-impact produces more ionized gas species. Through formation of $N_4^+$ and subsequent dissociative recombination, larger $N_2^+$ ion population leads to an enhancement of UV fluorescence emission from electronic excited state $C^3\Pi_\pi$ of $N_2$ [39].

In single-color, multi-cycle laser pulse excitation which results in a symmetric electron drift velocity distribution as discussed in Section 2, THz-REEF from nitrogen plasma is quadratically dependent on the THz field. Contrarily, the two-color laser fields generates ionized electrons with an asymmetric drift velocity which are controllable by the polarizations and relative phase of two optical fields $\phi_{\omega,2\omega}$ [76,88]. The electric field of a single-cycle THz pulse applied upon the laser-induced plasma alters the ionized electron momentum continuously by acceleration or deceleration, depending on whether the driving force from $\vec{E}_{\mathrm{THz}}(t)$ is parallel or anti-parallel to the electron initial velocity $\vec{v}(0)$ as illustrated in Fig. 27(b). In this manner, both the amplitude and direction of the THz field affect plasma fluorescence, whereas only amplitude of the THz field affects plasma fluorescence in single-color excitation. Therefore, the THz waveform information is encoded into the change of the fluorescence at different time delay $t_{\mathrm{d}}$ between the THz pulse and optical pulses. The THz waveform can be retrieved by measuring time-delay-dependent fluorescence emission both when $\vec{v}(0)$ is aligned parallel and aligned anti-parallel to $\vec{E}_{\mathrm{THz}}(t)$.

We characterized the phase dependence of the free electron velocity distribution in plasma by monitoring the intensity of the plasma-photocurrent-induced THz wave

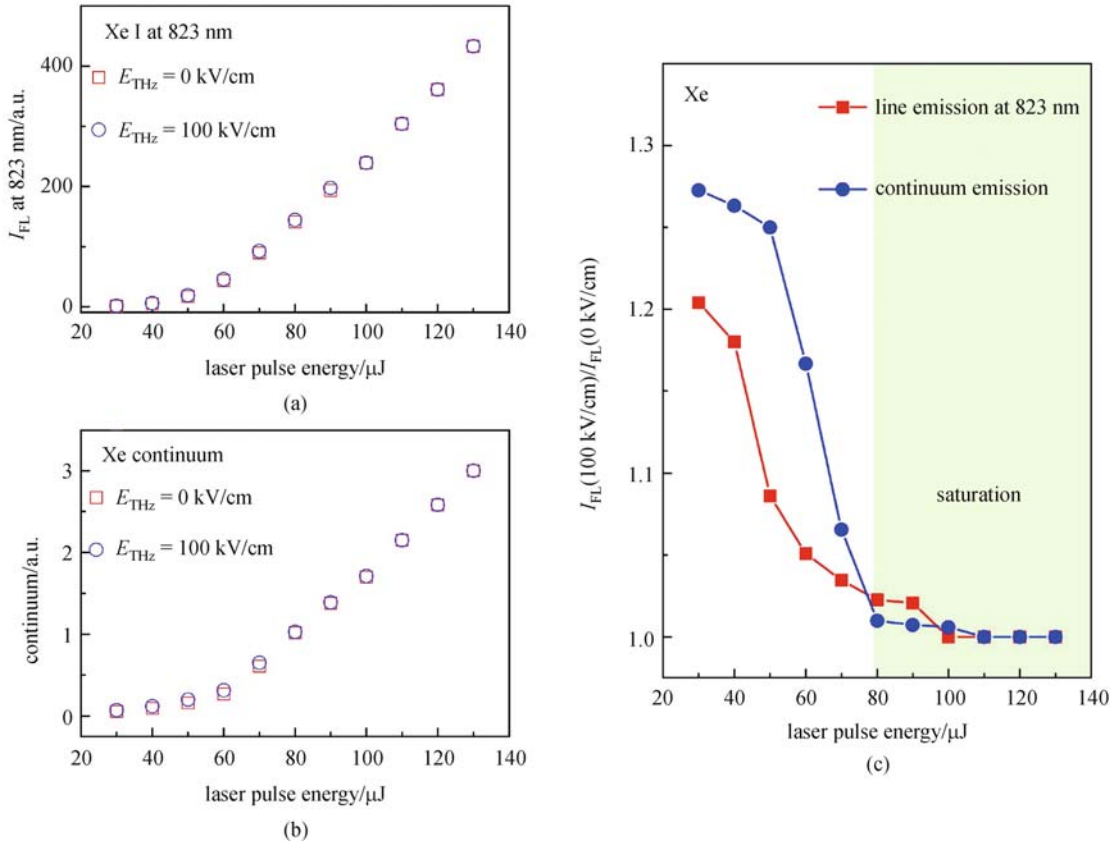


**Fig. 22** Pulse energy dependence of the (a) 823 nm line and (b) continuum emission in Xe plasma in the THz field; (c) laser pulse energy dependence of the enhancement ratio in the THz field. The shadow area is enhancement saturation region

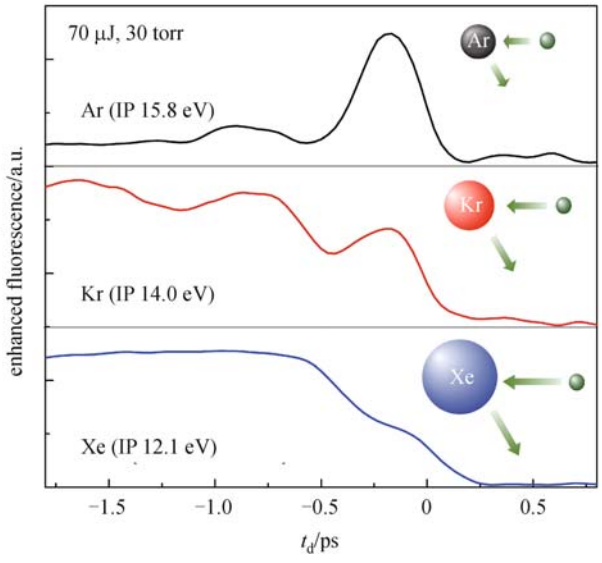


**Fig. 23** Time-dependent enhancement of the fluorescence emission in Ar, Kr, and Xe gases when the excitation pulse energy is 70 μJ and pressure is 30 torr

emission, $I_{THz}^{pla}$ and fluorescence intensity radiated from the two-color excited plasma, $I_{FL}$. To eliminate any interaction between the plasma and other THz sources, the external THz pulse from $LiNbO_3$ prism was blocked. $I_{THz}^{pla}$ was measured using a pyroelectric detector in the forward direction. A silicon wafer was put in front of the pyroelectric detector to filter out the $\omega$ and $2\omega$ pulses and pass the THz wave. $I_{FL}$ was collected sideways (detection angle is set as 90°) from the plasma by the fluorescence detection module as shown in Fig. 25. The strongest molecular nitrogen emission line at 357 nm was chosen. As $\omega$ and $2\omega$ pulses are overlapped temporally and spatially, the fluorescence emission from two-color lased plasma is increased by 50% compared to that generated by two non-overlapping pulses. The measurement results in comparison with the numerically calculated phase dependences of $I_{THz}^{pla}$ and total ion yield $N_2^+$ by using the general Ammosov–Delone–Krainov (ADK) tunnel ionization model [89] and tracing the ionized electron motion [11], are shown in Fig. 27(c). At the optical intensity of $10^{13}$ ~$10^{14}$ W/cm$^2$, the measured and calculated results show that $I_{THz}^{pla}$ and $N_2^+$ yield have the same periodic dependence on relative phase change $\Delta\phi_{\omega,2\omega}$ as shown in Fig. 27(d) . This means that the velocity distribution is a periodic function of $\Delta\phi_{\omega,2\omega}$, i.e., $\rho\left(\vec{v}(0), +\pi/2\right) = \rho\left(-\vec{v}(0), -\pi/2\right)$. The ionized elec-

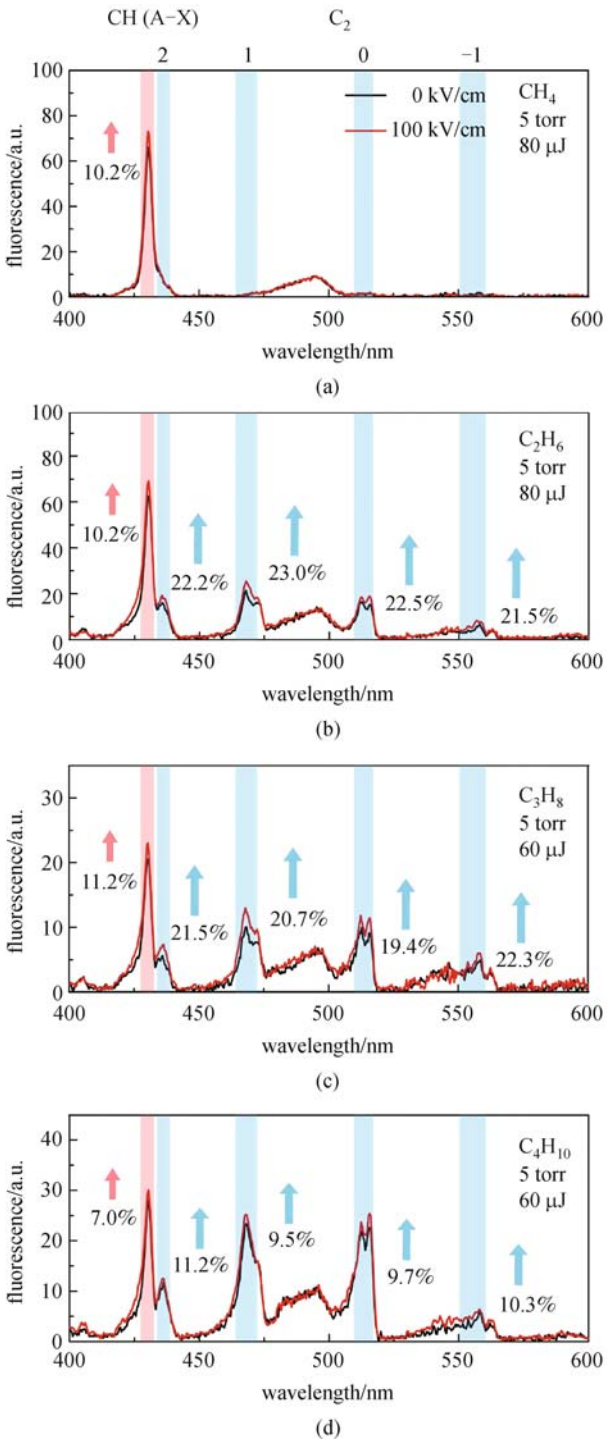


**Fig. 24** Fluorescence spectra of alkane gases in the THz field

tron velocity distribution $\rho\left(\vec{v}(0),\Delta\phi_{\omega,2\omega}\right)$ is strongly asymmetric at the phase generating largest photocurrent ($\Delta\phi_{\omega,2\omega}=\pm(2l+1)\pi/2$, in Fig. 27(d)), but almost symmetric at the phase generating smallest photocurrent ($\Delta\phi_{\omega,2\omega}=\pm l\pi$, in Fig. 27(d)) [56,80].

### 4.4 Electron velocity direction dependence of THz-REEF

When two-color pulses create a plasma before the external THz pulse from the $LiNbO_3$ crystal arrives (defined as $t_d<0$), the pre-existing plasma is influenced by the THz field. The THz pulse drives an electron to move faster if $\vec{E}_{THz}(t)$ is anti-parallel to the initial velocity or slower if $\vec{E}_{THz}(t)$ is parallel to the initial velocity. To verify this behavior, fluorescence intensities at different $\Delta\phi_{\omega,2\omega}$ were recorded as the time delay $t_d$ between the external THz pulse and the two overlapped optical pulses were changed. The optical polarization is set parallel to the THz polarization. Figure 28(a) shows a 3D plot of the THz-REEF $\Delta I_{FL}(t_d,\Delta\phi_{\omega,2\omega})$ as a function of $t_d$ and $\Delta\phi_{\omega,2\omega}$. As $\Delta\phi_{\omega,2\omega}$ varies, the shape of the time-resolved curve $\Delta I_{FL}(t_d,\Delta\phi_{\omega,2\omega})$ evolves, showing different signatures in the slope and in the following oscillatory part with a period of $2\pi$. As optical pulses fall behind the THz pulse ($t_d>0$), the $\Delta I_{FL}$ gradually drops to zero.

To further confirm the dependence of $\Delta I_{FL}(t_d,\Delta\phi_{\omega,2\omega})$ on electron velocity-direction, the same experiment with optical polarizations perpendicular to the external THz field was performed. The results are shown in Fig. 28(b). In contrast to the parallel case, the THz-REEF shows no change as $\Delta\phi_{\omega,2\omega}$ varies. This is because electrons with opposite velocities perpendicular to THz polarization are indistinguishable to the THz field and gain the same amount of energy from the THz pulse. Figure 28(c) shows the 3D plot of the differential REEF which is equal to the difference between $\Delta I_{FL}(t_d,\Delta\phi_{\omega,2\omega})$ minus $\Delta I_{FL}(t_d,0)$ when $E_\omega$, $E_{2\omega}$ and $E_{THz}$ are parallel. The differential REEF shows clear periodic change and reveals the external THz waveform information embedded in the fluorescence.

### 4.5 Differential REEF and coherent THz wave detection

The sliced, individual fluorescence change $\Delta I_{FL}\left(t_d,\pm(2l+1)\pi/2\right)$ for the same external THz pulse and optical intensity is shown in detail in Fig. 29. The different shapes of $\Delta I_{FL}(t_d,\Delta\phi_{\omega,2\omega})$ indicate how the initial electron drift velocity distribution $\rho\left(\vec{v}_e,\Delta\phi_{\omega,2\omega}\right)$ affects the electron heating by THz field and energy transfer in the electron-molecule inelastic collision. $\Delta I_{FL}(t_d,\pi/2)$ and $\Delta I_{FL}(t_d,-\pi/2)$ are found to be symmetric around $\Delta I_{FL}(t_d,0)$, as shown in Fig. 30(a).

A semi-classical model involving the electron acceleration in THz field, electron-molecule energy transfer and ionization of the high-lying Rydberg states, is used to calculate $\Delta I_{FL}$ and interpret the observed phase dependence of $\Delta I_{FL}$ in Fig. 30(b). In the approximation that electron mass $m_e$ is much smaller than that of the molecule, the average energy transferred from one electron to one

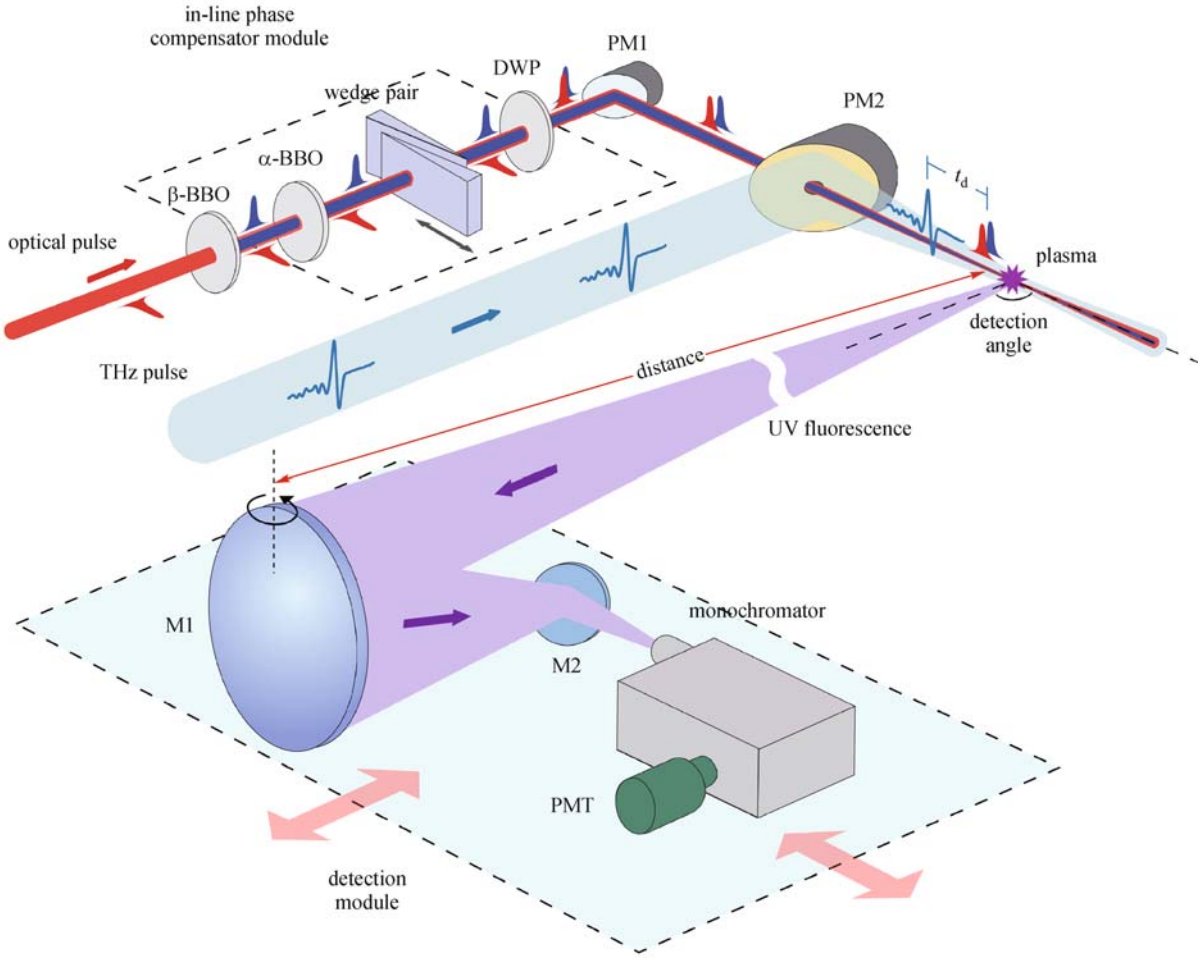


**Fig. 25** Schematics of the THz wave remote sensing. The $2\omega$ pulse is generated by passing the fundamental beam through a type I β-BBO crystal. Both of the fundamental and second harmonic optical pulses are linearly polarized along a vertical direction. The relative phase change between the $\omega$ and $2\omega$ pulses is tuned by the lateral translation of fused silica wedges in the optical beam path after the α-BBO. The two optical pulses are focused by a parabolic mirror with effective focal length of 150 mm into air to generate plasma. The time delay $t_d$ is defined as the delay between optical pulse peak and THz pulse peak. The distance of the remote sensing is varied by moving the fluorescence detection system

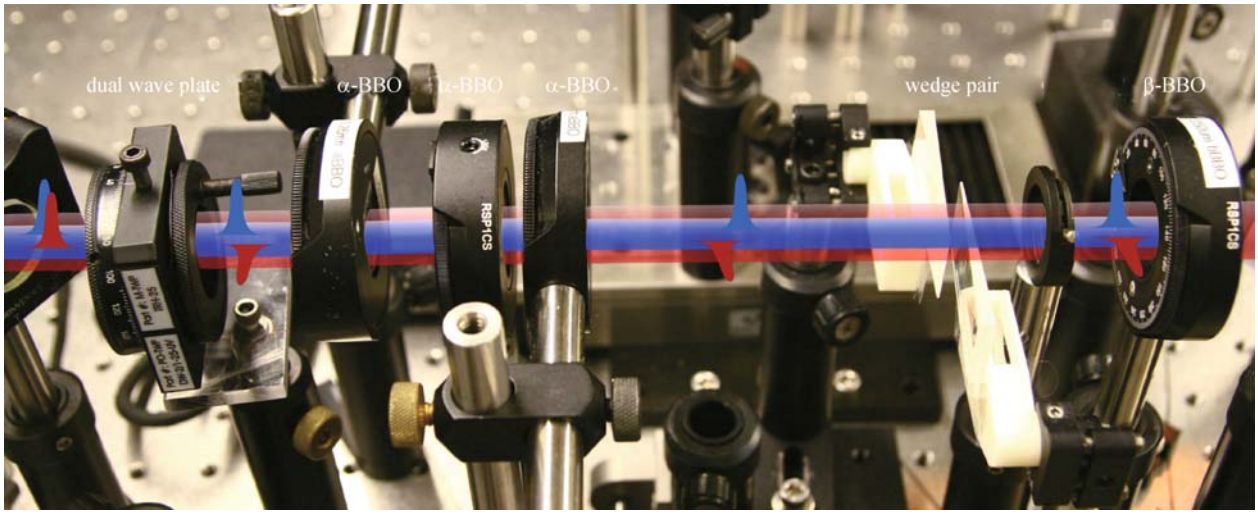


**Fig. 26** Photo image of the in-line phase compensator consisting of a β-BBO crystal, a few α-BBO crystals, a pair of the fused silica wedges, and a dual wave plate

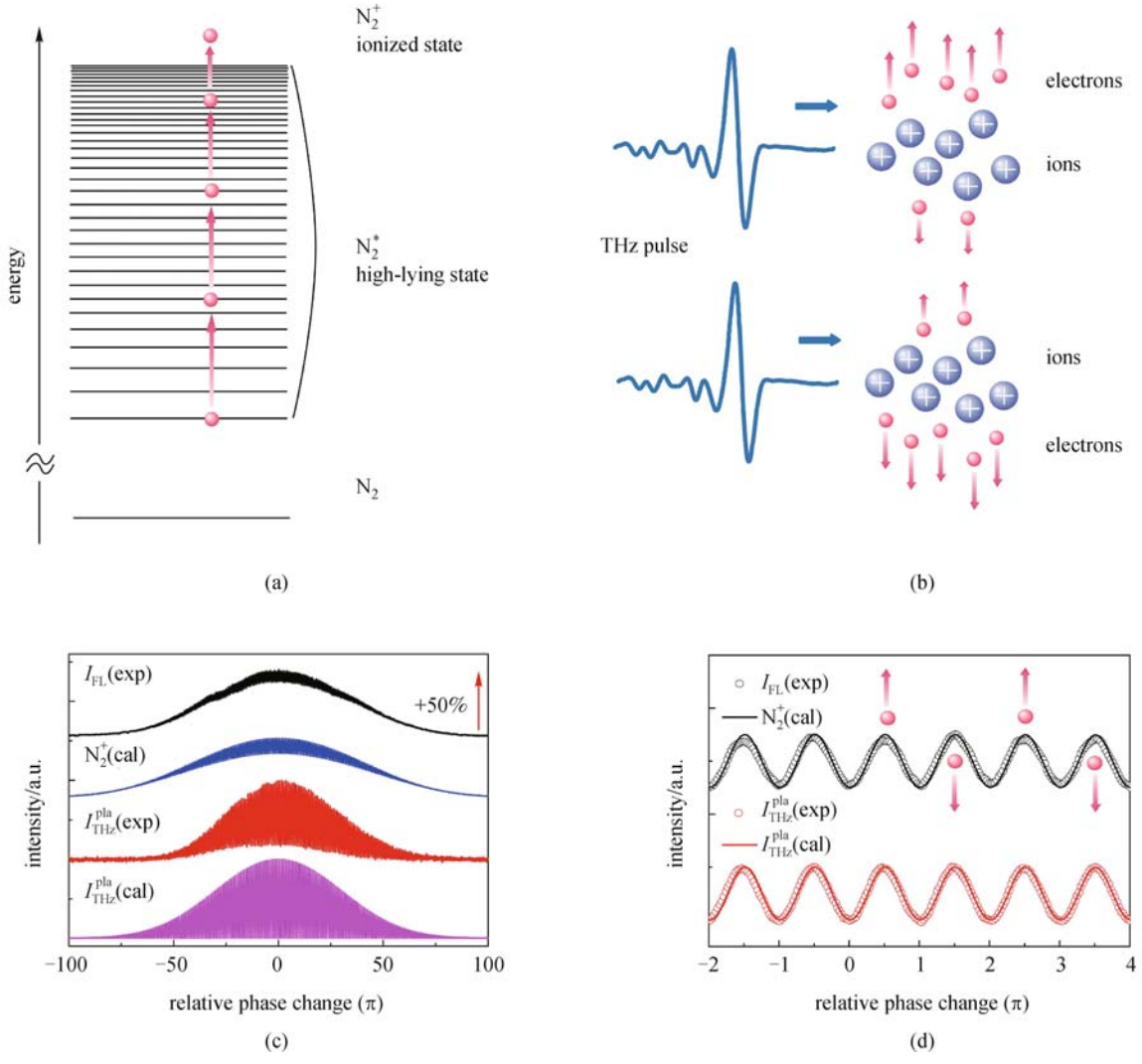


**Fig. 27** (a) High-lying states can be ionized by a series of collisions with energetic electrons; (b) interaction between the THz pulse and the asymmetric photoelectron velocity distributions generated by two-color fields ionization; (c) measured phase dependence of fluorescence emission $I_{FL}$ and plasma-photocurrent-induced THz emission $I_{THz}^{pla}$ are compared with the calculated phase dependence of ion yield $N_2^+$ and $I_{THz}^{pla}$; (d) zoom-in of (c) (shifted and normalized for clarity). Electron velocity direction is reversed as $\Delta\phi_{\omega,2\omega}$ is changed by π

molecule in each collision is $(2m_e/M)m_e\vec{v}_i^2/2$ [43]. This value is estimated to be on the order of meV at the electron temperature of $10^5$ K. Because of the quasi-continuum nature of the high-lying states spectra, molecule can be promoted by absorbing any amount of the energy. This means those states get further excited step-by-step by a series of collisions until they finally become ionized. As discussed in Section 2, the total fluorescence enhancement due to energy transfer over a long period of time can be described as below

$$\Delta I_{FL}(\Delta\phi_{\omega,2\omega}) \propto n_e\left[\int_{-\infty}^{+\infty}\left(m_e\vec{v}^2(0)+2m_e\vec{v}(0)\Delta\vec{v}_1\right)\rho\left(\vec{v}(0),\Delta\phi_{\omega,2\omega}\right)\mathrm{d}\vec{v}(0)/2+m_e\sum_{i=1}^{\infty}\Delta\vec{v}_i^2\right], \quad (12)$$

where $n_e$ is the electron density and $\Delta\vec{v}_i = -\int_{t_i-\tau}^{t_i} e\vec{E}_{THz}(t)\mathrm{d}t/m_e$. The $m_e\vec{v}^2(0)$ term is the energy transferred from the initial electron kinetic energy depending on laser intensity. The $\vec{E}_{THz}$ first order term, $2m_e\vec{v}(0)\Delta\vec{v}_1$, originates from acceleration before the first collision. The $\vec{E}_{THz}$ second order term, $m_e\sum_{i=1}^{\infty}\Delta\vec{v}_i^2$, is the energy transferred from the external THz field.

After applying the symmetry $\rho\left(\vec{v}_e,\pi/2\right) = \rho\left(-\vec{v}_e,-\pi/2\right)$ to Eq. (12), then we have a simplified

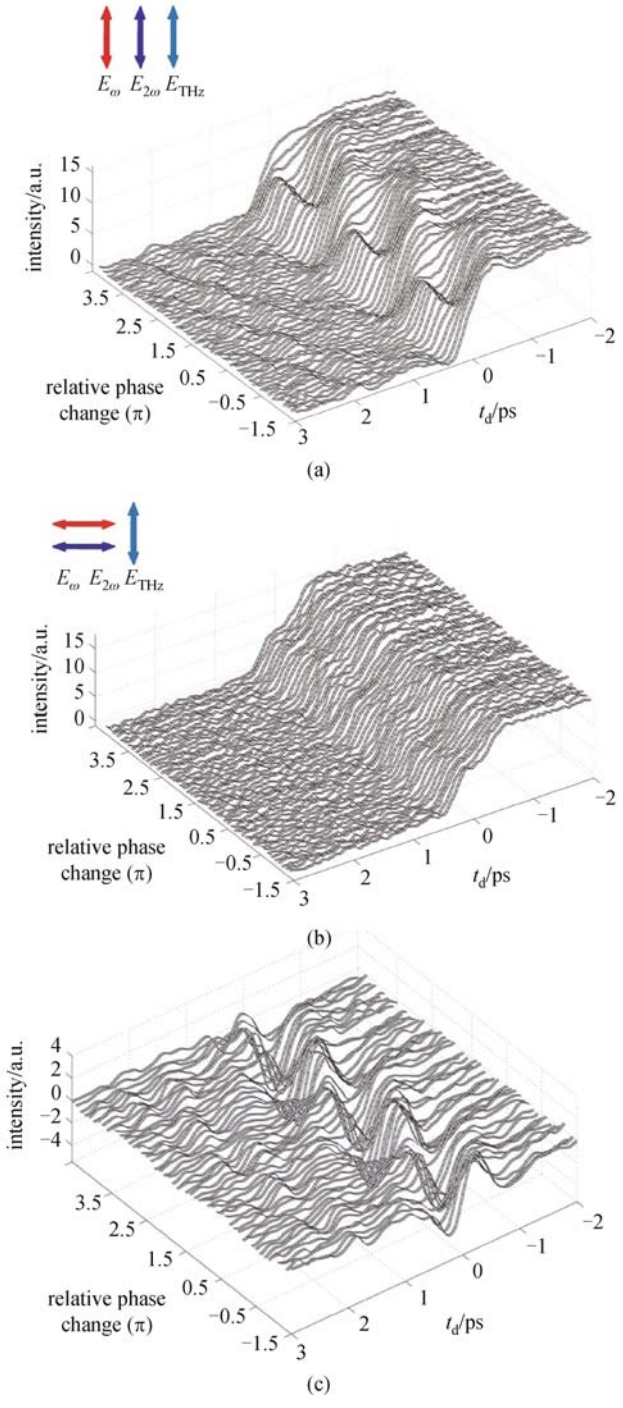


**Fig. 28** (a) 3D plot of THz-REEF at different relative optical phase between $\omega$ and $2\omega$ pulses when $\omega$, $2\omega$ and THz beams are all vertically polarized; (b) 3D plot REEF at different relative optical phase when $\omega$, $2\omega$ beams are horizontally polarized and THz beam is vertically polarized; (c) 3D plot of differential REEF between $\Delta I_{FL}(t_d,\Delta\phi_{\omega,2\omega})$ with any velocity distribution and $\Delta I_{FL}(t_d,0)$ with symmetric velocity distribution, under the same polarization condition as that in (a)

relationship between $\Delta I_{FL}(\Delta\phi_{\omega,2\omega}=\pm\pi/2)$ and $\Delta I_{FL}(\Delta\phi_{\omega,2\omega}=0)$, i.e.,

$$\Delta I_{FL}(\Delta\phi_{\omega,2\omega}=\pi/2)-\Delta I_{FL}(\Delta\phi_{\omega,2\omega}=0)$$
$$=-[\Delta I_{FL}(\Delta\phi_{\omega,2\omega}=-\pi/2)-\Delta I_{FL}(\Delta\phi_{\omega,2\omega}=0)].$$

Because electron relaxation time $\tau$ is ~350 fs [90] at atmospheric pressure and is small compared to the THz pulse cycle (~1.5 ps), we can assume that the THz field is nearly constant between neighboring collisions. With this assumption, we can segment the THz waveform into many small pieces and further simplify $m_e\sum_{i=1}^{\infty}\Delta\vec{v}_i^2$. The information of the THz time-domain waveform can be directly recovered by taking the difference between $\Delta I_{FL}(\Delta\phi_{\omega,2\omega}=\pi/2)$ and $\Delta I_{FL}(\Delta\phi_{\omega,2\omega}=-\pi/2)$:

$$\Delta I_{FL}(\Delta\phi_{\omega,2\omega}=-\pi/2)-\Delta I_{FL}(\Delta\phi_{\omega,2\omega}=\pi/2)$$
$$\propto n_e\rho\left(\vec{v}_e,0\right)e\tau\vec{v}_e(0)\vec{E}_{THz}\propto\vec{E}_{THz}. \quad (13)$$

The THz time-domain waveform obtained by differentiation was compared to the THz waveform measured with a 300 μm <110> GaP crystal through EO sampling [8], as shown in Fig. 30(b). Simulated time-delay-dependent THz-REEF at different phases using the semiclassical model, i.e., Eqs. (12) and (13), are shown in Fig. 30(c). There is a good agreement between the calculated phase dependence and the measurement results. This consistency makes the descriptive framework described above more convincing. This differential THz-REEF signal obtained in asymmetric plasma current offers a new method of THz wave coherent detection featured by its omni-directional emission pattern, which is essential for remote operation.

The application of this method in broadband, high-resolution, THz time-domain spectroscopy has also been demonstrated. Transmitted THz pulse in ambient air with relative humidity of 30% was measured using differential THz-REEF and the results are shown in Fig. 31(a). Water vapor absorption is exemplified by the ripples after the main peaks in the measured THz waveform. As a comparison, a reference waveform was measured when the entire optical system except the fluorescence detection system is purged with dry nitrogen gas. Their spectra, calculated through Fourier transformation of the waveforms, are plotted in Fig. 31(b).

The observed sharp absorption lines of the water molecule are consistent with previous measurement results obtained by using conventional THz time-domain spectroscopy system [91]. Here the spectral resolution in the current measurement is 0.02 THz, which can easily be further improved by using a longer sampling window of the THz waveform. Unlike the solid state THz detectors, this method is free of interference of the multi-reflection of THz pulse from the detector-air interface and so there is no limitation on length of the temporal sampling window. The spectral bandwidth here is only limited by the cut-off frequency of the $LiNbO_3$ emitter, which is determined by

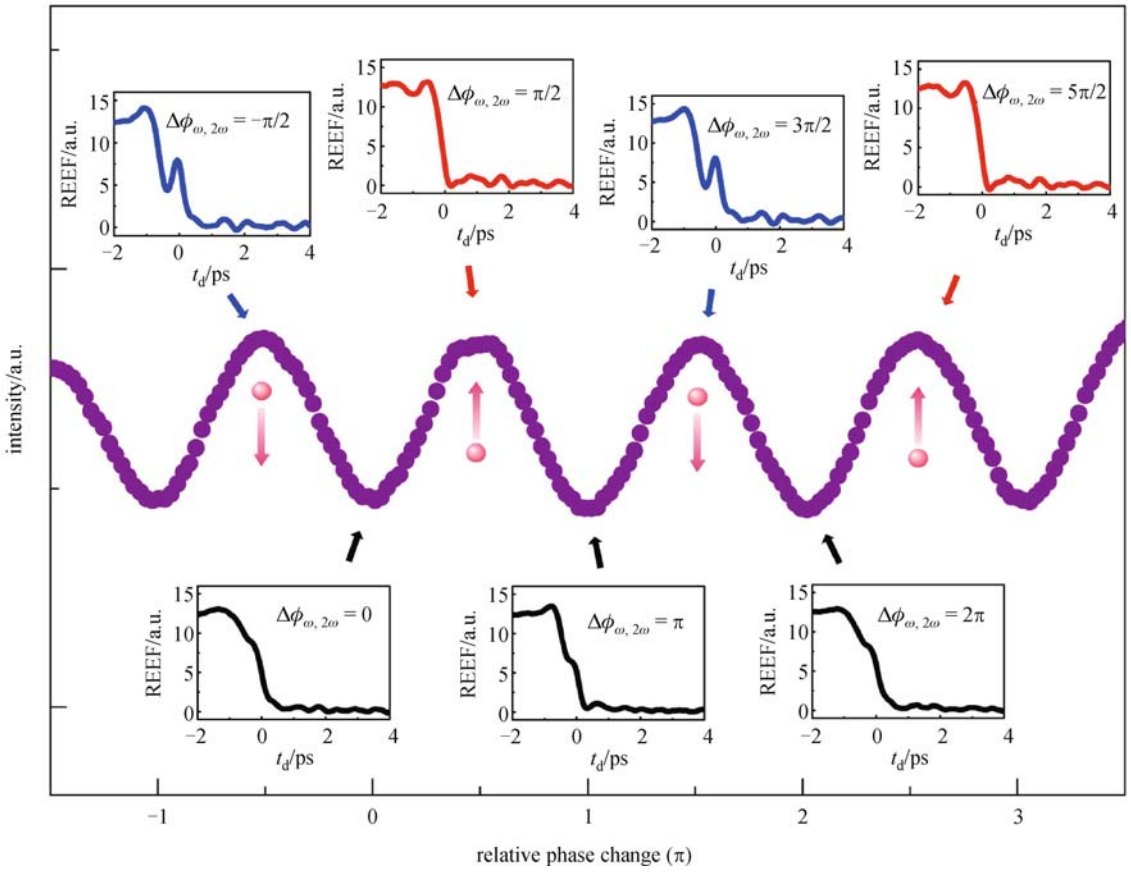


**Fig. 29** Measured time-resolved REEF at relative optical phase change $\Delta\phi_{\omega,2\omega} = \pm l\pi/2$

the phonon frequency and frequency dependence of the phase matching efficiency. To demonstrate the capability of this approach in inspection and identification of biologic/chemical materials, we measured the absorption spectrum of a 4-amino-2, 6-dinitrotoluene (4A-DNT) pellet sample compared with the results using EO sampling. The sample is a 0.5 mm thick pellet consisting of 20% 4A-DNT and 80% polyethylene. All the sample constituents were gently grounded to power and compressed into a pellet using 5 tons of pressure from a hydraulic press. The sample was in the path of the THz beam before the parabolic mirror focusing the THz beam. The THz waveform transmitted through the sample was measured and the results in Fig. 32 show good agreement between the two methods.

### 4.6 Broadband remote THz sensing

One of the advantages of this THz wave detection method is the standoff THz wave sensing capability. To demonstrate standoff sensing, we measured the THz waveform using the plasma UV fluorescence (357 nm) signal at different distances. The fluorescence detection module is placed at distances of 0.1, 5 and 10 m away from THz source/plasma respectively. The detection angle is 90°, i.e., sideways collection. By scanning the time delay between THz pulse and two-color laser pulses, we obtained the differential THz-REEF signal and recovered the time-dependent THz field. The measured waveforms and spectrum are shown in Fig. 33.

Despite the decreased fluorescence collection efficiency (~1/distance$^2$) and the reduced signal-noise-ratio of the THz wave measurement as the distance increases, the remote sensing system can well reproduce the THz waveform at different distances and clearly resolve the THz spectrum at a distance of 10 m. Water vapor absorption presented in the spectrum is due to the short distance (roughly 30 cm) THz wave propagation from local THz source to the plasma. This water absorption can be further reduced by creating plasma even closer to the THz source. Detection at farther distances is limited by the laser pulse energy as well as the current laboratory space.

This demonstrated broadband THz wave sensing using REEF provides a promising tool in various THz sensing and imaging applications with advantages of broadband, high resolution, pinpoint detection, omni-directional signal collection, and remote capability. With sufficient laser power, the combination of this THz wave remote sensing technique and previously demonstrated THz wave generation at long distance using two-color laser beam with stable

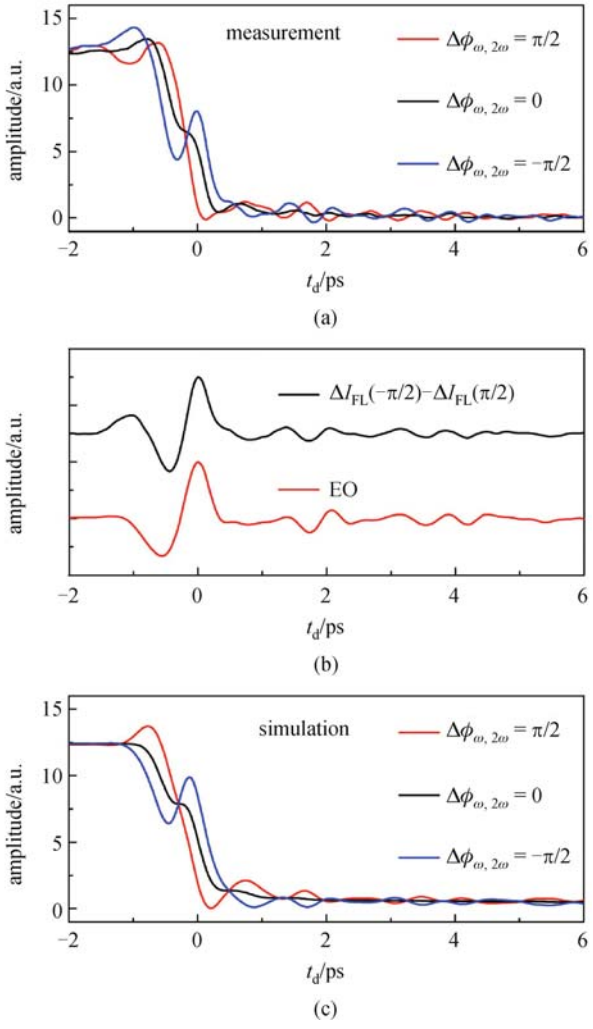


**Fig. 30** (a) Measured time-resolved THz-REEF at phase $\Delta\phi_{\omega,2\omega} = 0, \pm\pi/2$ respectively; (b) comparison between the THz waveform measured by electro-optic (EO) sampling and THz waveform obtained from the difference of the two REEF curves with opposite velocity distribution; (c) simulated THz-REEF derived from Eq. (12) at $\Delta\phi_{\omega,2\omega} = 0, \pm\pi/2$, respectively

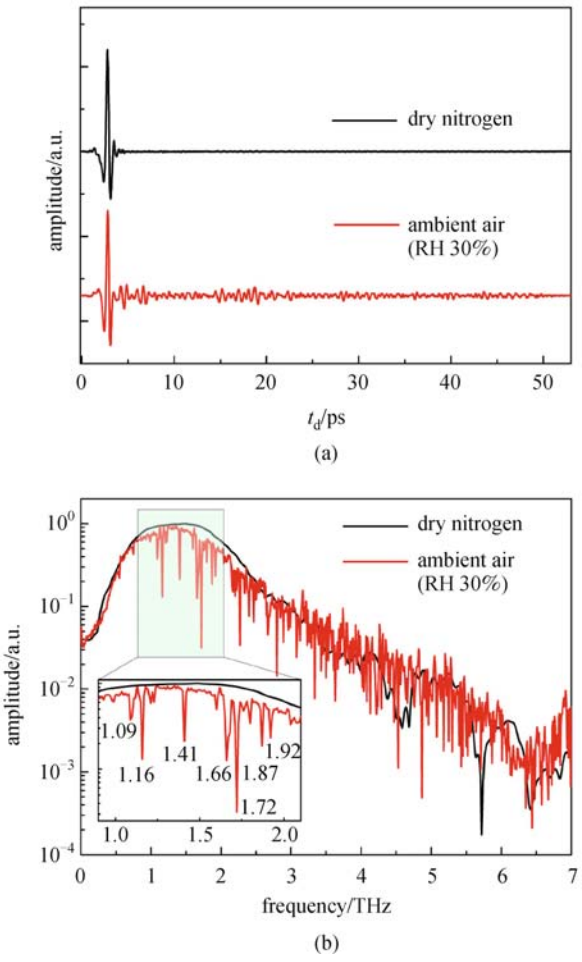


**Fig. 31** (a) Measured THz waveforms using REEF in dry nitrogen and ambient air environment, respectively; (b) corresponding THz spectra in logarithmic scale. The spectral resolution is 0.02 THz. Inset: Zoom-in on water vapor absorption features in shadow area

and accurate control of the relative phase, would eventually make remote THz spectroscopy available [25,92].

There are also some limitations or cons of broadband THz wave sensing using REEF: 1) the highest resolvable frequency is limited by the electron scattering frequency in the plasma. For the frequency component much higher than the electron scattering frequency, this sensing method has lower response than that for the low frequency component; 2) the laser safety issue. The use of the intense amplifier laser for the detection imposes potential threats to the human eyes.

The sensitivity of this sensing method has been experimentally determined by attenuating the THz field and measuring the corresponding REEF signal. The measurement results and quadratic fit are shown in linear scale and log scale in Figs. 34(a) and 34(b) respectively. The measured REEF signal agrees well with the quadratic fit in the field range of 3 to 100 kV/cm. There are some significant deviations at the field below 3 kV/cm as shown in Fig. 34(b). Therefore, in current system, the minimal detectable THz electric field is around 3 kV/cm that is mainly limited by the laser noise, detector noise and other noises. However, this sensitivity could be further improved by using a more sensitive detector (e.g., single photon counter), larger collection optics (e.g., UV reflective concave mirror of 20 inch[1)] diameter or larger) and gated fluorescence measurement (e.g., using gated PMT to reduce the scattered light from environment or laser beam).

1) 1 inch ≈ 2.54 cm

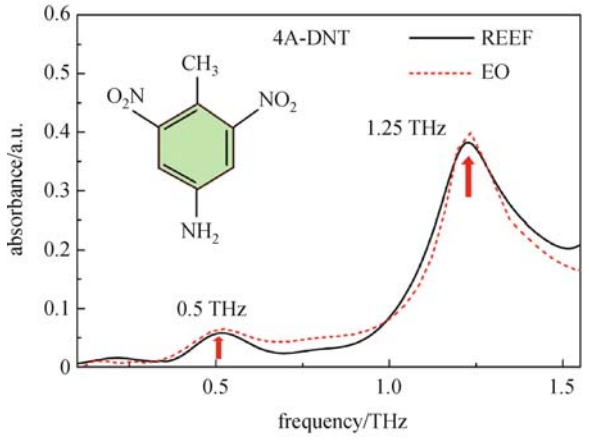


**Fig. 32** THz absorption spectrum of 4A-DNT measured by REEF compared with that measured by electric-optic sampling

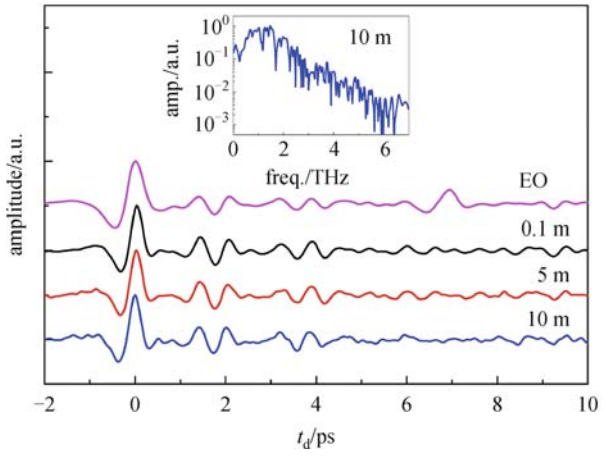


**Fig. 33** Broadband THz wave remote sensing. The measured THz waveforms by EO sampling and REEF at different distances from plasma were shown respectively. Waveforms are normalized and shifted for clarity. Inset: THz spectrum measured at a distance of 10 m

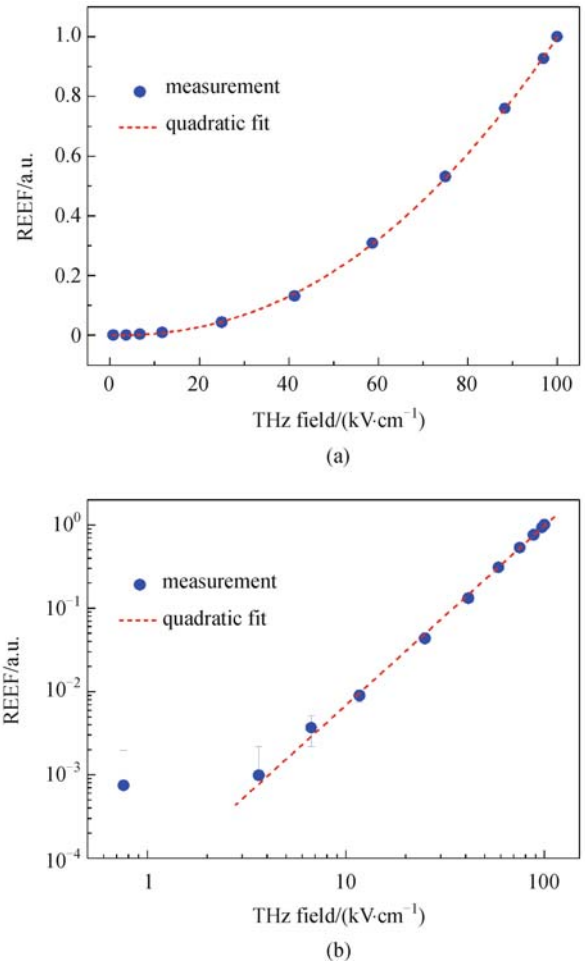


**Fig. 34** Measured field dependence of the REEF signal (solid dots) and quadratic fit (dashed line) (a) in linear scale and (b) in log scale

### 4.7 Summary

We introduced a novel "all optical" technique for broadband THz remote sensing utilizing the THz-REEF from two-color laser-induced gas plasma. By studying the ultrafast electron dynamics under the single cycle THz radiation, we found that the fluorescence emission from laser-induced air plasma is highly dependent on the THz electric-field and the symmetry of the electron drift velocity distribution created by two-color laser-fields. The time-resolved THz-REEF can be tailored by switching the relative two-color phase and laser polarizations. As a consequence, this provides a unique approach of detecting the amplitude and phase of the THz wave at the same time. With its onmi-directional emission pattern and minimal ambient water vapor absorption, this technique makes broadband standoff THz spectroscopy possible. Moreover, this offers a promising way to the characterization of electron behavior in strong light-matter interaction by revealing the detailed interplay process of the strong-field ionization, plasma dynamics, and THz-wave-induced electron heating.

## 5 Plasma diagnostics

In this section, we demonstrated that the THz-wave-enhanced fluorescence emission from excited atoms or molecules could be employed in the characterization of laser-induced gas plasmas. The electron relaxation time and plasma density were deduced through applying the electron impact excitation/ionization and electron-ion recombination processes to the measured time-resolved enhanced fluorescence. The electron collision dynamics of nitrogen plasma excited at different gas pressures and laser pulse energies were systematically investigated. This demonstrated plasma characterization method offers pico-

second temporal resolution and is capable of omni-directional optical signal collection.

### 5.1 Introduction

Plasma diagnostics is essential to the various industrial applications and has been employed in experimental plasma physics to characterize the physical properties of plasma, such as density, temperature and collision frequency [93]. The commonly used plasma diagnostic methods include Langmuir probe [94], plasma spectroscopy [95], microwave [96], and optical interferometry [97]. Laser-pulse-induced plasma is created by the photoionization of the strong optical pulse and is of transient nature with a fast temporal evolution of plasma temperature, plasma density, and collision frequency. A detailed understanding of the fast dynamics of laser-induced plasma is of great importance to potential applications in plasma chemistry, high harmonics generation [98], and self-guided filament propagation [99]. To study the property of laser propagation in the gas media, the plasma density inside the laser filaments was characterized by several groups based on different methods [46,48,100]. Among these methods, the electric conductivity measurement provides most direct density information of the plasma channel with a nanosecond temporal resolution [48]. Optical interferometric methods, measuring the interference between the sample beam and reference beam, are capable of resolving the plasma dynamics with sub-picosecond resolution [46,100]. Methyl-alcohol lasers operating in far-infrared range have also been used to measure plasma densities using interferometry since the 1980s [101]. In last few years, scientists introduced a plasma diagnostic method based on transmission THz time-domain spectroscopy, providing high temporal resolution, broad bandwidth coverage and high sensitivity [31,102,103].

We introduced a method to characterize laser induced plasma using THz wave enhanced fluorescence emission from the excited gas molecules/ions. The dynamic plasma properties in nitrogen and helium gas with different gas density and laser excitation intensity ($10^{13}$ ~ $10^{14}$ W/cm$^2$) were systematically investigated. We showed that the time-resolved enhanced fluorescence was used to deduce relaxation time and plasma density. This method provides picosecond temporal resolution by using an ultra-short THz pulse to probe the plasma, and unlimited directionality of optical signal collection which allows the characterization under the circumstances in which forward geometry is not allowed.

### 5.2 Method and experimental design

The basic mechanism and method are discussed first and then followed by the illustration of experimental schematic. The interaction between single-cycle THz pulses and laser-induced gas plasma has been recently studied by the THz-wave-enhanced fluorescence emission [58], as well as discussed in detail in Section 2. The enhanced fluorescence results from the THz wave induced electron heating, electron impact ionization of high-lying trapped states and subsequent increased population of fluorescing upper states. The time-resolved enhanced fluorescence $\Delta I_{\mathrm{FL}}$ can be expressed as [58]

$$\Delta I_{\mathrm{FL}}(\tau,t_{\mathrm{d}}) \propto n_{\mathrm{e}}(\beta_{\mathrm{ei}},t_{\mathrm{d}})\sum_{i=1}^{\infty}\Delta\vec{v}_i^{\,2}(\tau,t_{\mathrm{d}}), \qquad (14)$$

where $n_{\mathrm{e}}$ is the electron density as a function of electron-ion recombination rate $\beta_{\mathrm{ei}}$, and the time delay between laser pulse and the peak of the THz pulse, $t_{\mathrm{d}}$. $\tau$ is the average electron relaxation time. Here $\Delta\vec{v}_i(\tau,t_{\mathrm{d}}) = -\int_{t_{\mathrm{d}}+(i-1)\tau}^{t_{\mathrm{d}}+i\tau} e\vec{E}_{\mathrm{THz}}(t)\mathrm{d}t/m$ is the change of electron velocity in the THz field $\vec{E}_{\mathrm{THz}}(t)$ between two neighboring collisions at time $t_{i-1} = t_{\mathrm{d}} + (i-1)\tau$ and $t_i = t_{\mathrm{d}} + i\tau$ respectively. As the plasma temperature or plasma density changes, the $n_{\mathrm{e}}(\beta_{\mathrm{ei}},t_{\mathrm{d}})\sum_{i=1}^{\infty}\Delta\vec{v}_i^{\,2}(\tau,t_{\mathrm{d}})$ will be also changed. With the prior knowledge of the THz waveform, $\tau(=t_i-t_{i-1})$ and temporal evolution of $n_{\mathrm{e}}$ can be obtained from the measured $\Delta I_{\mathrm{FL}}$.

Figure 35 shows the experimental schematic, where a gas plasma is generated inside the gas cell by focusing a femtosecond laser pulse with 80 fs pulse duration, 1 kHz repetition rate and 800 nm center wavelength. A convex lens of 100 mm effective focal length is used for focusing laser beam. The pulse energy can be varied from 60 to 150 μJ by tuning the power attenuator. The maximal optical intensity at the focus is estimated to be $10^{13}$ ~$10^{14}$ W/cm$^2$. A vacuum pump is used to control gas density and switch the gas species in the cell.

A $LiNbO_3$ prism is used for THz source and efficiently generates linearly polarized single-cycle THz pulses. The output THz pulse has pulse width $\tau_{\mathrm{THz}}$ of 1 to 1.5 ps, and peak field of (100±2) kV/cm. The single-cycle THz pulse is collinearly focused onto the optical focal region to interact with the laser-induced plasma. Front and rear cell windows are 1 mm thick quartz plates, which are fairly transparent in visible and THz range. The time-domain waveform of the THz pulse is characterized by a 300 μm thick <110> GaP crystal through electro-optical sampling [36].

The fluorescence emission from gas plasma is collected by a convex lens (50 mm diameter and focal length 75 mm) and located outside the gas cell. The fluorescence was refocused through a narrow band interference filter to a photo-multiplier tube. Here we focus our interest on the laser-induced nitrogen plasma because nitrogen gas constitutes 78% of earth's atmosphere by volume and understanding its intrinsic properties is crucial to many

atmospheric laser applications such as lightening control and pollution control. To monitor the nitrogen fluorescence and effectively reject the surrounding scattering light, a narrow-band interference filter with center transmission wavelength of 357 nm and a full-width-half-magnitude of 10 nm, is used to transmit the strongest line of nitrogen molecules ($C^3\Pi_u - B^3\Pi_u$).

As time delay between THz pulse and laser pulse is tuned continuously by a translation stage, the time-resolved fluorescence signal, $\Delta I_{FL}$, is measured and recorded. As shown in Fig. 35, a typical time-resolved fluorescence signal consists of a slowly falling tail (bottom) and a steep rising edge (shaded area). The sign of $t_d$ takes the convention that $t_d > 0$ when the peak of the THz pulse proceeds the laser pulse, while $t_d < 0$ when the THz pulse trails the laser pulse. The steep rising edge results from the THz-field-assisted electron impact ionization and subsequent fluorescence enhancement. Its shape is highly dependent on $\sum_{i=1}^{\infty} \Delta \vec{v}_i^2$, i.e., the electron relaxation time and temporal shape of the THz pulse. Within the THz pulse duration $\tau_{THz}$, the free electrons motion is affected by THz field and plasma temperature is increased. The THz-wave-assisted impact-ionization process takes place on a much long time scale (usually nanosecond) before the electrons cool down or get recombined by the dissociative ions. Therefore the plasma density $n_e(\beta_{ei}, t_d)$ can be considered nearly constant during the THz pulse duration. The slowly falling tail of $\Delta I_{FL}$ is due to electron-ion recombination and thus represents the temporal evolution of plasma density.

### 5.3 Pressure dependence

The pressure dependence of the time-resolved fluorescence enhancement $\Delta I_{FL}(t_d)$ in pure nitrogen gas and nitrogen-

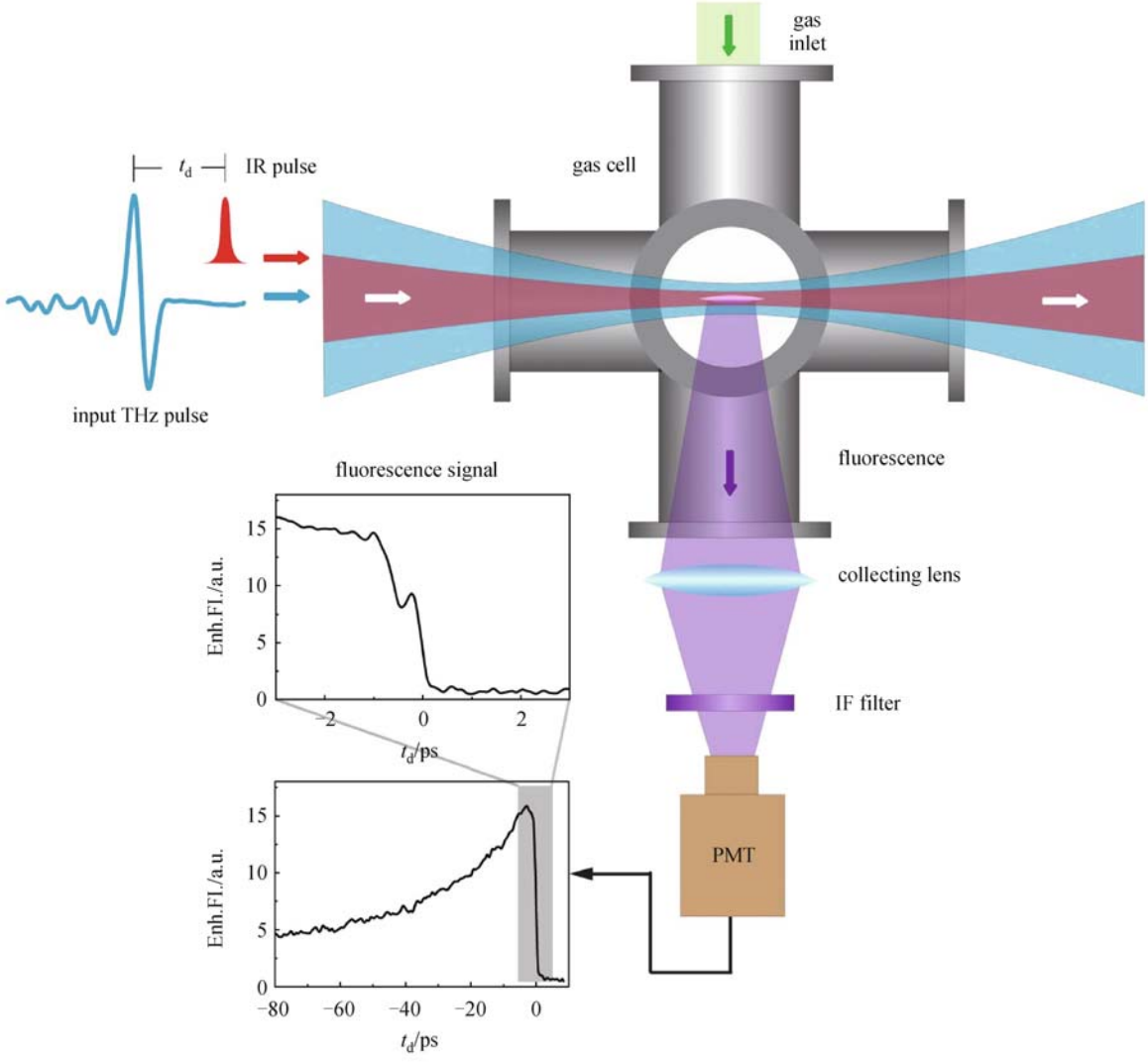


**Fig. 35** Schematics of plasma characterization using THz-wave-enhanced fluorescence. IF, interference filter; PMT, photo-multiplier tube; Enh. Fl., enhanced fluorescence

helium gas mixture, were experimentally characterized as shown in Figs. 36(a) and 36(b) respectively. Varying amounts of helium were added to the nitrogen as a buffer gas. For the intensities involved here, helium gas remains almost non-ionized due to its high ionization potential (24.6 eV). Thus the helium gas does not contribute the electron density and all the ionized electrons are assumed to be released by nitrogen molecules. But the presence of more helium atoms changes the interspacing between gas particles and thus increases the electron collision frequency. This change is reflected by the observed changing shape of $\Delta I_{\mathrm{FL}}(t_{\mathrm{d}})$ as total pressure changes. We found that pressure dependent behaviors in Figs. 36(a) and 36(b) are quite similar. This observation suggests that the collision frequency is mainly determined by the total particle density. The average relaxation time of free electrons can be theoretically estimated as

$$\tau_{\mathrm{t}} = \frac{1}{\sigma \overline{v}_{\mathrm{e}} N_{\mathrm{s}}}. \tag{15}$$

Here, $\sigma$ is the scattering cross section, $\overline{v}_{\mathrm{e}}$ is the average electron velocity and $N_{\mathrm{s}}$ is the total scatterer density. At pulse energy of 80 μJ, the ionization degree is very low ($<10^{-3}$, i.e., only less 0.1% of gas particles are ionized). Therefore, $N_{\mathrm{s}}$, mainly composed of the neutral particles including nitrogen molecules and helium atoms, is proportional to total gas pressure. Because scattering cross sections of helium and nitrogen are in the same order ($\sigma \sim 10^{-19}\mathrm{m}^2$) [104,105] and the initial electron drift velocity is determined by the optical intensity, only $N_{\mathrm{s}}$ can be changed and thus the electron relaxation time is mostly determined by $N_{\mathrm{s}}$. As the pressure varies, the shape of the $\Delta I_{\mathrm{FL}}(t_{\mathrm{d}})$ also varies significantly. For example, $\Delta I_{\mathrm{FL}}(t_{\mathrm{d}})$ shows a "two step" shape on the rising edge at high pressure ($\tau \ll \tau_{\mathrm{THz}}$). However, at low pressure ($\tau \gg \tau_{\mathrm{THz}}$), $\Delta I_{\mathrm{FL}}(t_{\mathrm{d}})$ exhibits quite different shapes and is zero at large negative delay because of $\int_{-\infty}^{\infty} \vec{E}_{\mathrm{THz}}(t)\mathrm{d}t = 0$.

To deduce $\tau$ at different pressures, an algorithm of root mean square (RMS) minimization was used to fit the $\Delta I_{\mathrm{FL}}(t_{\mathrm{d}})$ curve measured at each pressure. The procedures in the algorithm are:

1) $\sum_{i=1}^{\infty} \Delta \vec{v}_i^2(\tau, t_{\mathrm{d}})$ is calculated using the known $\vec{E}_{\mathrm{THz}}(t)$ and an initially given $\tau$. Then we obtain an error function which is defined as the RMS difference between $\sum_{i=1}^{\infty} \Delta \vec{v}_i^2(\tau, t_{\mathrm{d}})$ and measured $\Delta I_{\mathrm{FL}}(t_{\mathrm{d}})$ after $\sum_{i=1}^{\infty} \Delta \vec{v}_i^2(\tau, t_{\mathrm{d}})$ and $\Delta I_{\mathrm{FL}}(t_{\mathrm{d}})$ are normalized.

2) We change $\tau$ by a certain amount, which is defined by step size. Then we compare new error function with the old one calculated from 1). The smaller RMS difference means that the chosen value of $\tau$ is closer to the best fit value.

3) The change and comparison processes are repeated several times until the global minimum of error function is reached or the RMS is smaller than a pre-set threshold for biggest acceptable error. Then the obtained $\tau$ is the electron relaxation time.

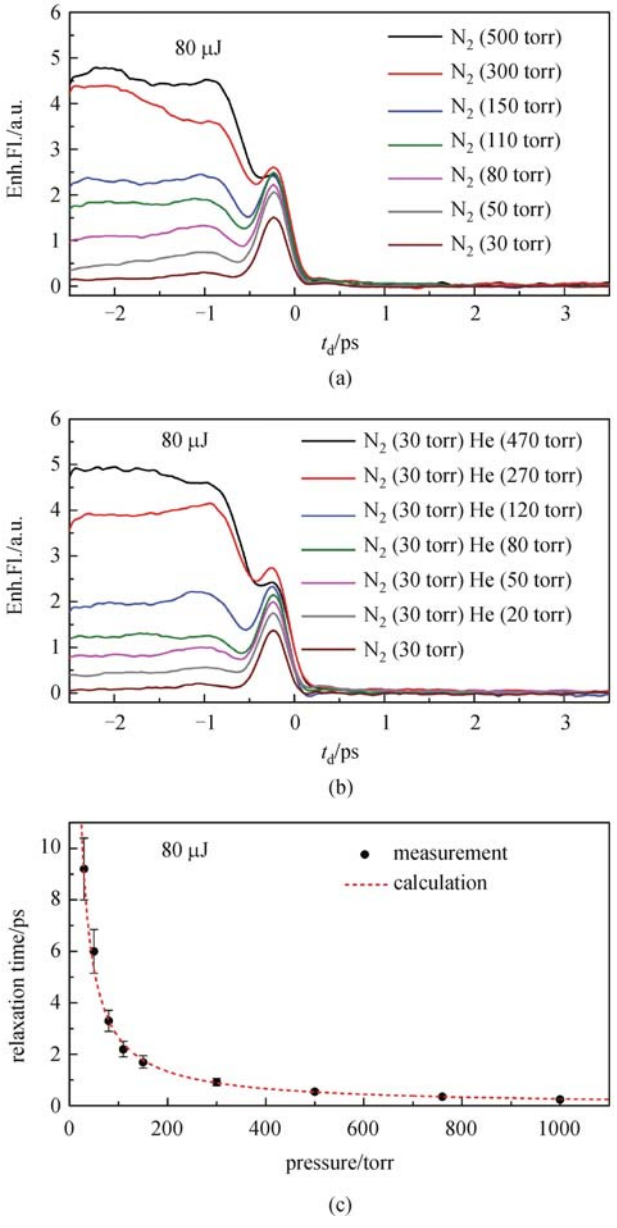


**Fig. 36** Pressure dependences of the enhanced fluorescence (Enh. Fl.) in (a) pure nitrogen gas and (b) mixture of nitrogen and helium gas. The laser pulse energy is 80 μJ. (c) Comparison between measured (solid squares) and calculated (dash line) relaxation time. The error bar is due to the uncertainty from the fitting for 5 individual scans measured at the same pressure

We use the above algorithm to deduce $\tau$ at each gas pressure and results are plotted in solid dots in Fig. 36(c). The deduced value is also compared with the theoretically calculated $\tau_{\mathrm{t}}$ at different pressures. A good agreement within measurement uncertainty was found. In the theoretical calculation of relaxation time, $\tau_{\mathrm{t}}$ at atmospheric pressure ($N_{\mathrm{s}} = 2.7 \times 10^{19}\mathrm{cm}^{-3}$) is estimated to be 350 fs

[44]. Since the shape of $\sum_{i=1}^{\infty}\Delta\vec{v}_i^2(\tau,t_d)$ is essentially determined by how THz pulse is segmented by $\tau$, the sensitivity of the method is high for relaxation time which is comparable to the THz pulse duration. This method might not be very accurate if the relaxation is too small (e.g., $<20$ fs) or too big (e.g., $>2000$ fs).

### 5.4 Plasma density measurement

Besides measuring the electron collision dynamics, we also demonstrate that THz-wave-enhanced fluorescence emission can be used for plasma density measurement. As the THz pulse is further temporally delayed behind the laser pulse ($t_d < -2$ ps), the number of electrons being influenced by the THz pulse decreases accordingly due to plasma decay which is dominated by the electron-ion recombination in the first few ns after the photoionization [46].

With this assumption, the rate equation of electron density evolution can be simplified to

$$\frac{\partial n_e}{\partial t} = -\beta_{ei} n_e n_i. \tag{16}$$

Here, $\beta_{ei}$ is the electron-ion recombination rate and $n_i$ is the ion density. In single-charged plasma ($n_i = n_e$), the temporal evolution of $n_e(t)$ can be solved analytically to be $n_e(t) = 1/\left(1/n_e(0) + \beta_{ei}t\right)$, where $n_e(0)$ is the initial electron density. In nitrogen, $\beta_{ei}$ was measured to be $6.1 \times 10^{-6}\mathrm{cm}^3\cdot\mathrm{s}^{-1}$ at 29 torr [47].

It is expected that $\beta_{ei}$ is larger at higher pressure due to the increased density of complex ions and three-body recombination. As an estimation, $\beta_{ei} \sim 10 \times 10^{-6}\mathrm{cm}^3\cdot\mathrm{s}^{-1}$ is used for fitting in the pressure range of 40 to 500 torr. Therefore, one can obtain the electron density $n_e$ by fitting the slowly falling tail of $\Delta I_{FL}(t_d)$ with the electron density equation.

Figure 37(a) shows the measured $\Delta I_{FL}(t_d)$ and fitted $n_e(t)$ at 100, 300 and 500 torr. Three decay curves are fitted well by using $(1.4 \pm 0.06)$, $(2.3 \pm 0.1)$ and $(2.8 \pm 0.1) \times 10^{15}\mathrm{cm}^{-3}$ for $n_e(0)$ respectively. The decay rate depends heavily on $n_e(0)$ and thus this makes the density measurement sensitive. In Fig. 37(b), the measured (deduced) plasma densities at different pressures are plotted and compared with the background fluorescence signal which is measured when incident THz pulse is blocked from interacting with plasma. The background fluorescence signal is expected to approximately proportional to the ion density. The agreement between the results from two measurements proves the validity of the plasma density measurement using THz-wave-enhanced fluorescence emission.

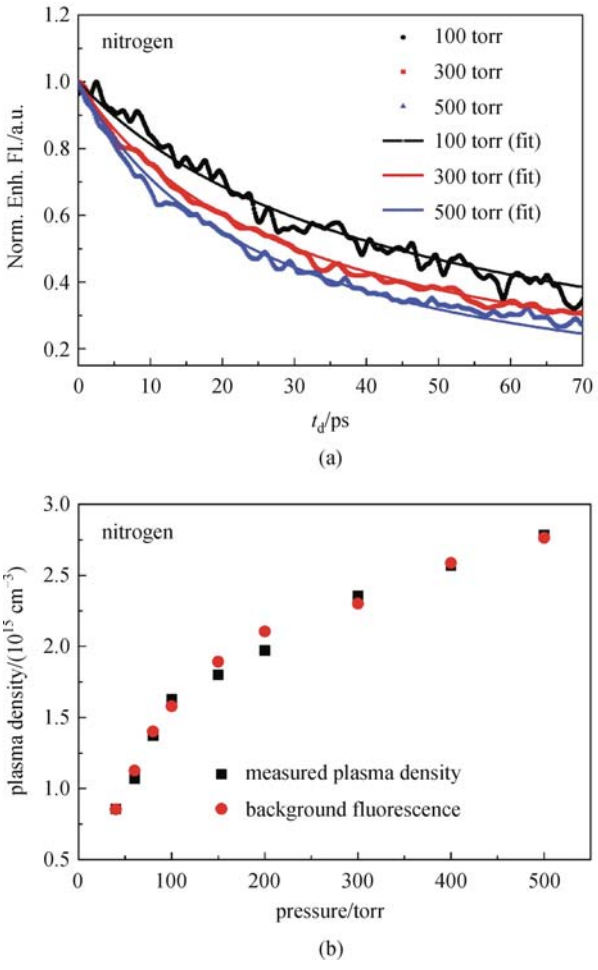


**Fig. 37** (a) Measured (symbol) and fitted (line) $\Delta I_{FL}(t_d)$ at 100, 300 and 500 torr, respectively. All the curves are normalized for clarity; (b) plasma densities extracted from $\Delta I_{FL}(t_d)$ curves are compared with normalized background fluorescence signal (without THz field) at different pressures. Norm. Enh. Fl., normalized enhanced fluorescence

### 5.5 Collision dynamics at different excitation pump power

Electron collision dynamics under irradiation of laser pulses with different pulse energies was also experimentally investigated. The time-resolved $\Delta I_{FL}(t_d)$ was measured at pulse energy range of 60 to 150 μJ. The results are displayed in Fig. 38(a). The relaxation time at each power was deduced by using the algorithm described in Section 5.3 and the corresponding results are shown in Fig. 38(b).

One can clearly see that the $\tau$ decreases with higher pulse energy. This decrease at higher pump power can be explained by the increased electron velocity, and larger average scattering cross section. Scattering cross section of the ion is larger than that of the neutral particle due to the existence of Coulomb force between ion and electron. Therefore the increased ion density would increase the average scattering cross section. The inset (Fig. 38(b)) shows the pulse energy dependence of the measured background fluorescence signal and ion density calculated using the ADK model [89].

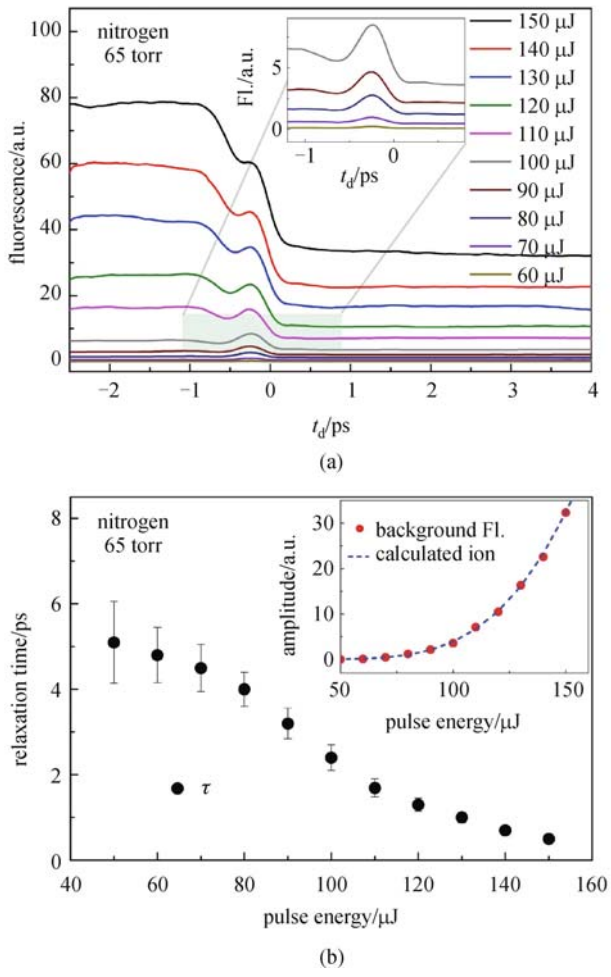


**Fig. 38** (a) Measured nitrogen fluorescence (Fl.) with different excitation laser pulse energies at 65 torr. The shade area is enlarged for clarity; (b) measured electron relaxation time. Inset, the measured background fluorescence signal (sold red circle) and calculated ion density being normalized to fluorescence signal (blue dash line)

### 5.6 Summary

In this section, we demonstrated a method for plasma characterization through THz-wave-enhanced fluorescence emission. The correlation between the time-resolved enhanced fluorescence and plasma parameters such as relaxation time and electron density, are quantitatively determined. The proposed characterization method is capable of resolving plasma dynamics with high temporal resolution and providing omni-directional signal collection which is crucial to potential remote applications.

## 6 Photoluminescence quenching by terahertz wave

In this section, we study the quenching dynamics of laser-pulse-induced photoluminescence in semiconductors under the radiation of single-cycle THz pulses. Photoluminescence quenching was observed when electron kinetic energy gained from the THz field was larger than initial excess electron energy. We found that the quenching in both of cadmium telluride (CdTe) and gallium arsenide (GaAs) was linearly proportional to the intensity of incident THz waves and reaches up to 17% and 4%, respectively, at a peak THz intensity of 13 MW/cm$^2$. The carrier dynamics on the sub-picosecond scale in semiconductor was characterized by time-resolved photoluminescence measurement. The ultrasfast decay times of THz-pulse-induced quenching are measured to be (700±60) fs for CdTe and (350±30) fs for GaAs respectively.

### 6.1 Introduction

The ultrafast carrier dynamics in semiconductors are of great importance to the development and application of high-speed devices, laying the critical foundation for the rapid growth of information technology in the past decades [106]. Several optical techniques, such as optical-pump-THz-probe and optical-pump-optical-probe, have been used to investigate the fundamental physical processes such as carrier transport in semiconductors [107–109]. Recently time-resolved THz spectroscopy, due to its broadband spectral coverage and high sensitivity in electron density and mobility measurements, has emerged as a versatile technique for resolving carrier motion and distribution in semiconductors on ultrashort time scale [110–114]. But most of the study was done in the "linear" optical region due to the lack of intense THz sources in the past. The large scale free electron laser provides high THz wave output power, but its wide application is limited by the accessibility. Recent years have witnessed the development of high-power, table-top THz pulse sources, which includes the THz generation from laser-induced air plasma and THz generation from $LiNbO_3$ crystal using tilted pulse front scheme. The laser-induced air plasma provides a broadband bandwidth which is only limited by the laser pulse duration, while the $LiNbO_3$ crystal offers very high energy conversion efficiency (usually 0.1%). These newly developed THz sources have enabled the experimental study of "nonlinear" optical response of materials at THz frequencies and the carrier dynamics under intense THz field over a time scale of picoseconds and sub-picoseconds [34,115–119]. However, although photoluminescence spectroscopy has been widely used as a diagnostic tool for semiconductor light-emitting devices and recently used to study the interaction of THz wave and laser-induced gas plasma [58,61], few studies on semiconductor photoluminescence under the influence of intense THz radiation have been reported. The role of a strong THz field in carrier recombination dynamics has not been well understood. Photoluminescence can be used as a probe to acquire rich information regarding carrier dynamics on a time scale of sub picoseconds. Compared to conventional methods

using transmission geometry, this method has two advantages: 1) the convenience of simple optical alignment; 2) flexibility of signal collection direction. Moreover, the study of THz-pulse-modulated photoluminescence can provide enhanced understanding of the ultrafast carriers dynamics and can be potentially useful for the applications of a non-invasive ultrafast modulator of photoluminescence device with picoseconds switching time, which are of great interest to the scientists and researchers in the fields of light-emitting devices and optical communication.

Through the systematic study of the photoluminescence quenching dynamics in CdTe and GaAs induced by intense single-cycle THz pulses, we illustrate the relationship between THz wave intensity and photoluminescence quenching. The measured dependence of photoluminescence quenching on time delay between THz pulse and optical excitation pulse, reveals THz-wave-modulated carrier recombination dynamics. The results were theoretically analyzed and numerically fit by the exponential decay of THz-wave-induced change of carrier energy. It is also worth noting that no significant photoluminescence quenching was observed in ZnSe, ZnTe, $Zn_{1-x}Cd_xTe$ ($0 < x < 0.8$) or GaP.

### 6.2 Photoluminescence spectra in THz field

The schematic of the photoluminescence quenching experiment is illustrated in Fig. 39(a). A Ti:sapphire amplifier laser used here has 800 nm center wavelength, 1 kHz repetition rate, 80 fs pulse duration, and 600 μJ pulse energy. Most of the laser pulse energy was used for THz wave generation while only small amount of the laser pulse energy was used for optical excitation in the semiconductor since too much laser power would create high density carriers on the semiconductor surface and build up electronic screening for the THz field. About 400 μJ laser pulse energy was used to generate a THz pulse via optical rectification in a $LiNbO_3$ crystal using the tilted-pulse-front scheme to realize good match between THz phase velocity and optical group velocity [34]. The optical excitation beam with much weaker pulse energy (~ 0.01 μJ) and the THz beam were collinearly focused by off-axis parabolic mirrors onto the semiconductor surface at normal incident angle.

The focal spot diameters of the THz beam and optical beam are about 0.5 and 0.05 mm, respectively. The peak field strength of the THz pulse at focus is 100 kV/cm and corresponding the peak intensity is 13 MW/cm$^2$. The actual intensity of the THz wave illuminated on the semiconductor surface was tunable by rotating two metal wire-grid broadband THz polarizers (extinction ratio > 1000:1 and bandwidth ~ 0 to 4 THz). The spectra of photoluminescence emitted from the semiconductors were measured by a spectrometer consisting of a monochromator and a photomultiplier tube. The wavelength range of the spectrometer is from 200 to 900 nm.

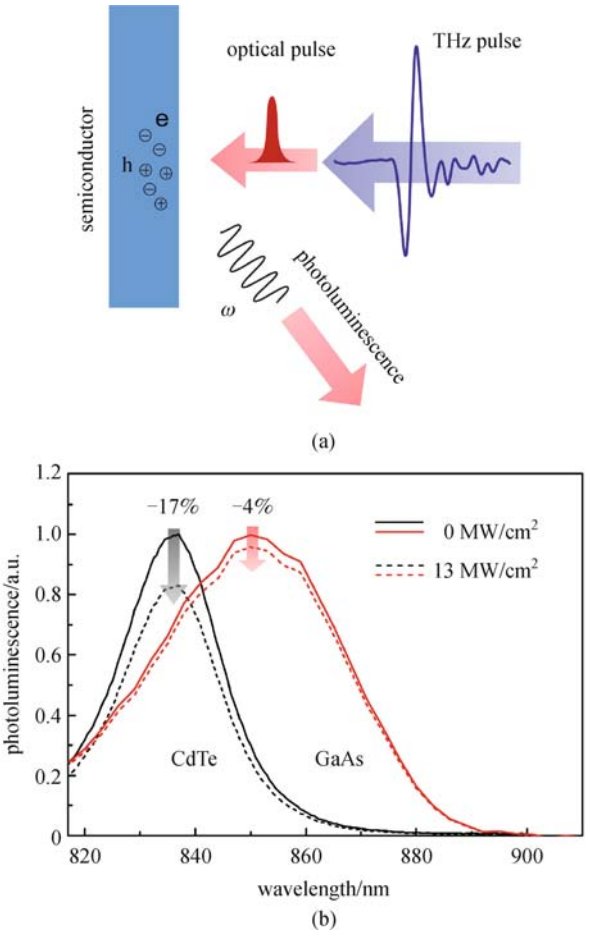


**Fig. 39** (a) Schematic of the THz-wave-induced photoluminescence quenching experiment; (b) measured photoluminescence emission spectra of CdTe and GaAs at the peak THz intensity of 0 (solid lines) and 13 MW/cm$^2$ (dashed lines)

The photoluminescence spectra of CdTe and GaAs under the THz wave intensities of 0 and 13 MW/cm$^2$ respectively were measured and the results are shown in Fig. 39(b). The time delay between the THz pulse and laser excitation pulse is set to a certain value so that maximal quenching is reached. The time-resolved quenching will be discussed in detail in Section 6.3. The spectra of CdTe are centered at 837 nm, which is equivalent to the bandgap of 1.48 eV. The spectra of GaAs are centered at 850 nm,which is equivalent to the bandgap of 1.45 eV. When the THz wave with peak intensity of 13 MW/cm$^2$ is incident on the semiconductor, the photoluminescence emissions from CdTe and GaAs are decreased by 17% and 4% compared to those without the THz radiation presented, respectively. The only change in the emission spectra is the amplitude and no significant spectral shift was observed in either of the spectra. This hints that the stark shift in the THz field is not the dominating mechanism here.

### 6.3 Time-resolved quenching

To further investigate the time-resolved photoluminescence quenching, we measured the intensity of photoluminescence from CdTe and GsAs at their peak wavelengths, respectively as a function of time delay, $t_d$, between the THz pulse and the optical excitation pulse. The spectrometer only allows the photoluminescence component at 837 nm pass for CdTe and only allows the photoluminescence component at 850 nm pass only for GaAs. Since the emission profile remains unchanged, the amplitude of the spectral peak is linearly proportional to the total photoluminescence emission integrated over the spectrum.

Figure 40 plots the measured results of CdTe and GaAs together with THz time-domain waveform. The THz waveform was measured by electro-optic sampling [36]. The time delay is defined such that the optical pulse is behind the peak of the THz pulse at positive time delay.

It can be seen that the photoluminescence reaches its minimum when the optical pulse is temporally close to the positive peak of the THz pulse for both CdTe and GaAs. The time-resolved quenching curve is composed of a fast falling edge and a slow rising edge. The fast falling edges of the photoluminescence curves of CdTe and GaAs are quite similar and within 0.5 ps. This time scale is coincident with the rising edge of the THz pulse envelope. But as the time delay increases further, i.e., the laser excitation pulse is further behind the THz pulse peak, the GaAs photoluminescence curve shows a faster recovery compared to that of CdTe. The reason for this different recovery rate will be further addressed in Section 6.5.

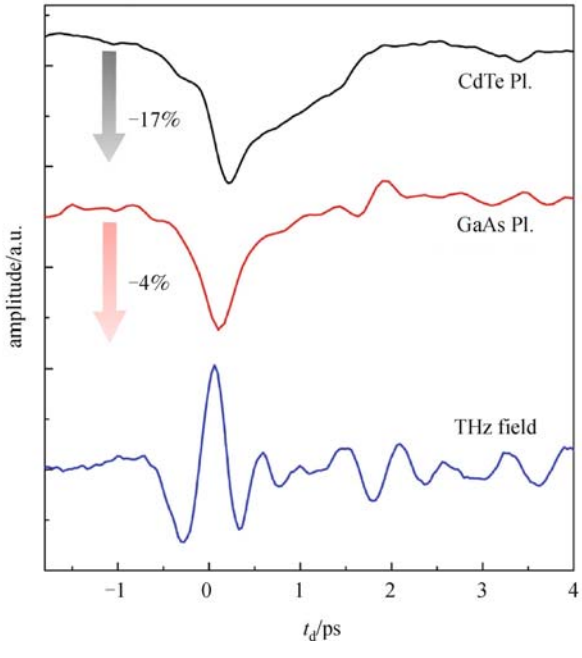


**Fig. 40** Measured time-resolved photoluminescence (Pl.) quenching in CdTe at 837 nm (top) and in GaAs at 850 nm (middle) in comparison with the time-domain waveform of a THz pulse (bottom)

### 6.4 THz intensity dependence of quenching

The THz intensity dependences of the photoluminescence quenching were measured in CdTe and GaAs in the intensity range of 0 to 13 MW/cm$^2$. 13 MW/cm$^2$ is the maximal THz intensity achievable in current experiment setup and is limited by the maximal laser output power. A pair of metal-wire broadband THz polarizers was used to attenuate the incident THz power and keep the polarization of the incident THz beam unchanged. The results of the intensity dependence measurement and linear fit are shown in Fig. 41. The time delay was set at the timing when maximal quenching occurs. The good agreement between the measurement results and linear fit indicates that the quenching magnitude is linearly proportional to the incident THz wave intensity. We also found that the quenching magnitude is independent of the THz polarization.

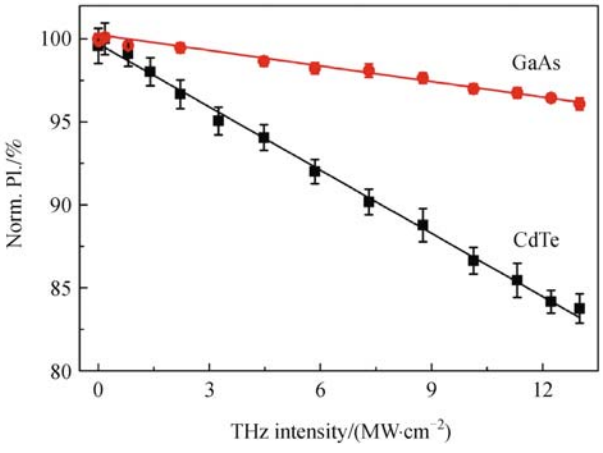


**Fig. 41** Solid black squares and red dots show the measured THz intensity dependence of photoluminescence in CdTe and GaAs, respectively. Solid lines are the linear fit. The error bars were obtained from the multiple measurements at the same point. Norm. Pl., normalized photoluminescence

### 6.5 Theory and numerical simulation

Photoluminescence quenching is usually referred to the decrease of the photo emission intensity of a sample. Common causes for photoluminescence quenching are different types of interaction including excited-state reactions, charge separation, molecular rearrangements, energy transfer, ground-state complex formation, and collisional quenching [120]. Two or more mechanisms can occur at the same time.

To identify what mechanisms are responsible for the observed quenching effect here, we first discuss various possibilities as follows:

1) The THz-wave-induced intravalley and intervalley scattering of the photocarriers might reduce the photoluminescence radiation efficiency by creating more channels for non-radiative carrier recombination, such as thermal decay without emitting any photon.

2) THz-field-assisted exciton dissociation, which is typically the quenching mechanism at cryogenic temperature, is not likely to happen here because the exciton population negligible in current experiment which was conducted at the room temperature.

3) The photoluminescence spectral profile (bandwidth and peak wavelength) when the THz field is applied, remained unchanged. This indicates that the transient THz-field-induced Franz-Keldysh effect [121] or band gap renormalization [122] is not the dominant mechanism here. Otherwise, one would expect to see the change of spectral profile.

4) Also the time-resolved measurement results suggest that the quenching effect is not only due to the "direct" interaction between THz field and photocarriers, because quenching was even observed at a time delay of 1 ps when the laser pulse was behind the THz pulse as shown in CdTe. If THz wave only influences the photocarriers, one should not expect such significant quenching at the time delay of 1 ps when photocarriers experience little THz radiation.

Taking all the arguments above into consideration, we could speculate that the quenching observed in CdTe and GaAs is probably due to the heating of the intrinsic and photo carriers by the THz field and subsequent heating of the lattice through electron-lattice collision [106]. The increase in the temperature of the carriers and lattice would affect the efficiency of photocarrier generation and recombination in various ways such as carrier-carrier scattering, carrier-phonon scattering, and etc. Shortly after heating process takes place, the quenching effect gradually vanishes as the carriers and lattice cool down over time. This decay process corresponds to the slow recovery edge observed in Fig. 40. Decay time could vary for different semiconductors and this may explain the different rate of observed quenching decay.

Here we are also intent to acquire more quantitative information about the quenching dynamics observed in CdTe and GaAs. If we express the THz-wave-induced photoluminescence quenching $\Delta PL(t_{\mathrm{d}})$ in exponential function, we can have following empirical equation:

$$\Delta PL(t_{\mathrm{d}}) \propto -\int_{t_{\mathrm{d}}}^{\infty} |E_{\mathrm{THz}}(t)|^2 \exp\left(-(t-t_{\mathrm{d}})/\tau\right) \mathrm{d}t, \quad (17)$$

where $E_{\mathrm{THz}}(t)$ is the incident THz field and $\tau$ is the exponential decay time constant for THz-pulsed-induced quenching. The appearance of $|E_{\mathrm{THz}}(t)|^2$ in Eq. (17) comes from the observed linear dependence of quenching on the THz wave intensity. By using the pre-known THz time-domain waveform $E_{\mathrm{THz}}(t)$, we can fit the profile of the time-delay-dependent photoluminescence using $\tau = (700 \pm 60)$ fs for CdTe and $\tau = (350 \pm 30)$ fs for GaAs respectively.

The experimental data and fitting using Eq. (17) are shown in Fig. 42. The fitting process was based on minimization of the root mean square of the difference between the numerical calculation and measurement data. Longer decay time in CdTe corresponds to the observed slower recovery edge. The decay time might be related to the thermal cooling, electron-electron scattering rate, electron-lattice scattering rate, recombination rate and etc.

It is also worth noting that no significant photoluminescence quenching was observed either in ZnSe, ZnTe, $Zn_{1-x}Cd_xTe$ ($x$ = 0.2, 0.4, and 0.6) or GaP. One possible reason for the absence of the photoluminescence quenching in these semiconductors is that after two photon absorption in these samples, the excess electron energy is too large to be significantly influenced by the THz field. The excess electron energy can be estimated by subtracting bandgap energy from two laser photon energy, and the value is $> 0.7$ eV for these materials. The increase of electron energy by the THz field is estimated to be about $0.2 \sim 0.3$ eV under current conditions. Therefore, the effect induced by the THz wave might be too small to be

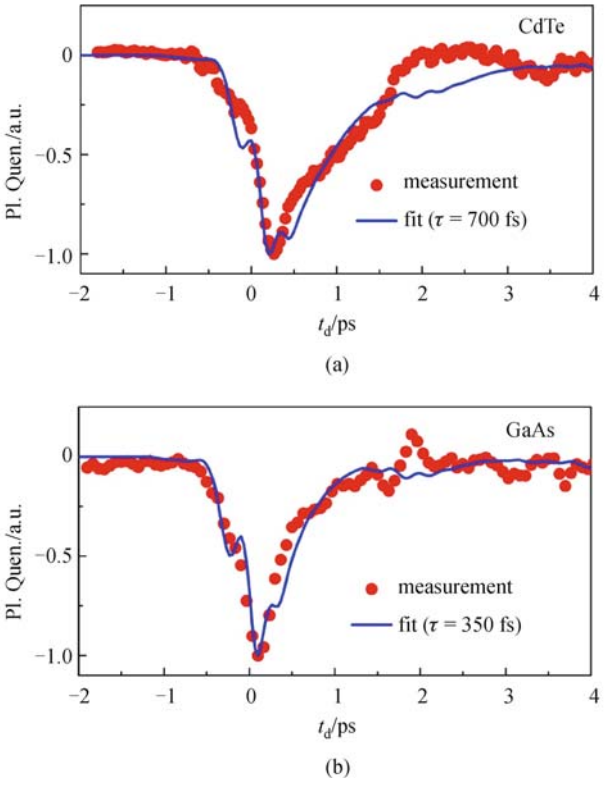


**Fig. 42** Measured photoluminescence signal (normalized) as a function of time delay between THz pulse and optical excitation pulse, and fitting results in (a) CdTe and (b) GaAs, respectively. Pl. Quen., photoluminescence quenching

observed because the energy increase is much smaller than excess electron energy. Unlike those materials, the excess electron energies in CdTe and GaAs, are only 0.07 and 0.1 eV, respectively, which are smaller than energy THz wave can transfer to the carriers. On other words, compared with the "hot" photocarriers, the "cold" photocarriers are more easily affected by the THz-wave-induced heating of carriers and lattice.

### 6.6 Summary

In this section, we reported the phenomena of photoluminescence quenching in semiconductors induced by intense THz pulses. We found that the quenching was linearly dependent on the THz wave intensity in the range of 0 to 13 MW/cm$^2$. Maximal quenching of 17% and 4%, respectively, was observed in CdTe and GaAs at a THz wave intensity of 13 MW/cm$^2$. The quenching is also highly dependent on the relative time delay between the THz pulse and laser excitation pulse. The THz-wave-induced heating of carriers and lattice and the subsequent decreased efficiency of photocarrier generation and recombination are most likely to be responsible for the quenching observed here. This study provides an enhanced understanding of ultrafast carrier dynamics which is of great importance to the future development and next-generation application of light-emitting devices and high speed electronic devices.

## 7 Conclusions

This paper presented the study of the underlying physics of the light-plasma interaction at THz frequencies, as well as its important applications, such as broadband THz remote sensing, plasma diagnostics and ultrafast photoluminescence modulation.

A semiclassical model was built to investigate the interaction between the single-cycle THz pulse and femtosecond-pulse-induced plasma. The experiments under different gas pressure, THz field strength, laser excitation intensity and gas species, were performed to verify the theoretical study and further characterize the ultrafast dynamics occurring in the process. The observed THz-REEF, can be explained by the electron heating in the THz field and electron-impact-excitation of gas molecules/ions.

Inspired by the THz-REEF from single-color laser induced plasma, we further introduced a novel "all optical" technique for broadband THz remote sensing utilizing the THz-REEF from two-color laser-induced gas plasma. The fluorescence emission is highly dependent on the THz electric-field and the symmetry of the electron drift velocity distribution created by two-color laser-fields. As a consequence, this provides a unique approach for detecting the amplitude and phase of the THz wave at the same time. With its onmi-directional emission pattern and minimal ambient water vapor absorption, this technique makes broadband standoff THz spectroscopy possible. Moreover, the technique offers a promising way to the characterization of electron behavior in strong light-matter interaction by revealing the detailed interplay process of the strong-field ionization, plasma dynamics, and THz-wave-induced electron heating. This demonstrated broadband THz wave sensing provides a promising tool in various THz sensing and imaging applications with advantages of broadband, high resolution, pinpoint detection, omni-directional signal collection, and remote capability. The cons of the method include the limitation of the highest resolvable frequency by the plasma scattering frequency and the safety issue caused by the use of the amplifier laser.

As one application of the THz-REEF, we demonstrated a unique plasma diagnostic method through THz-wave-enhanced fluorescence emission. The correlation between the time-resolved enhanced fluorescence and plasma parameters such as relaxation time and electron density, were quantitatively determined. The proposed diagnostic method is capable of resolving plasma dynamics with high temporal resolution, providing omni-directional signal collection which is crucial to potential remote applications.

Furthermore, the phenomena of photoluminescence quenching in semiconductors induced by intense THz pulses was investigated. We found that the quenching is linearly dependent on the THz wave intensity. Maximal quenching of 17% and 4%, respectively, was observed in CdTe and GaAs at a THz wave intensity of 13 MW/cm$^2$. The THz-wave-induced heating of carriers and lattice and the subsequent decreased efficiency of the photocarrier generation and recombination are most likely responsible for the quenching observed. This study provides an enhanced understanding of ultrafast carrier dynamics which is of great importance to future development and next-generation application of light-emitting devices and high speed electronic devices.

The work presented in this paper provides an improved understanding of the underlying physical principles associated with THz plasma photonics and experimental demonstration that extends its capability to a wide range of promising applications. These contributions will help further broaden the scope of the THz science and technology to homeland security, environmental monitoring, plasma-related applications and the light-emitting industry.

## References

1. Ferguson B, Zhang X C. Materials for terahertz science and technology. Nature Materials, 2002, 1(1): 26–33
2. Mittleman D M, Gupta M, Neelamani R, Baraniuk R G, Rudd J V, Koch M. Recent advances in terahertz imaging. Applied Physics B,

Lasers and Optics, 1999, 68(6): 1085–1094
3. Nahata A, Weling A S, Heinz T F. A wideband coherent terahertz spectroscopy system using optical rectification and electro-optic sampling. Applied Physics Letters, 1996, 69(16): 2321–2323
4. Shen Y C, Lo T, Taday P F, Cole B E, Tribe W R, Kemp M C. Detection and identification of explosives using terahertz pulsed spectroscopic imaging. Applied Physics Letters, 2005, 86(24): 241116-1–241116-3
5. Tonouchi M. Cutting-edge terahertz technology. Nature Photonics, 2007, 1(2): 97–105
6. Karpowicz N, Zhong H, Zhang C L, Lin K I, Hwang J S, Xu J Z, Zhang X C. Compact continuous-wave subterahertz system for inspection applications. Applied Physics Letters, 2005, 86(5): 054105-1–054105-3
7. Exter M, Fattinger C, Grischkowsky D. High-brightness terahertz beams characterized with an ultrafast detector. Applied Physics Letters, 1989, 55(4): 337–339
8. Wu Q, Zhang X C. Free-space electro-optic sampling of terahertz beams. Applied Physics Letters, 1995, 67(24): 3523–3525
9. Cook D J, Hochstrasser R M. Intense terahertz pulses by four-wave rectification in air. Optics Letters, 2000, 25(16): 1210–1212
10. Xie X, Dai J, Zhang X C. Coherent control of THz wave generation in ambient air. Physical Review Letters, 2006, 96(7): 075005-1–075005-4
11. Kim K Y, Taylor A J, Glownia J H, Rodriguez G. Coherent control of terahertz supercontinuum generation in ultrafast laser-gas interactions. Nature Photonics, 2008, 2(10): 605–609
12. Karpowicz N, Dai J M, Lu X F, Chen Y Q, Yamaguchi M, Zhao H W, Zhang X C, Zhang L L, Zhang C L, Price-Gallagher M, Fletcher C, Mamer O, Lesimple A, Johnson K. Coherent heterodyne time-domain spectrometry covering the entire "terahertz gap". Applied Physics Letters, 2008, 92(1): 011131–011133
13. Woo W, DeGroot J S. Microwave absorption and plasma heating due to microwave breakdown in the atmosphere. Physics of Fluids, 1984, 27(2): 475–487
14. Gibbon P, Förster E. Short-pulse laser-plasma interactions. Plasma Physics and Controlled Fusion, 1996, 38(6): 769–793
15. Kruer W L, Dawson J M. The physics of laser plasma interactions. Physics Today, 1989, 42(8): 69–70
16. Filevich J, Rocca J J, Marconi M C, Smith R F, Dunn J, Keenan R, Hunter J R, Moon S J, Nilsen J, Ng A, Shlyaptsev V N. Picosecond-resolution soft-X-ray laser plasma interferometry. Applied Optics, 2004, 43(19): 3938–3946
17. Seely J F, Harris E G. Heating of a plasma by multiphoton inverse bremsstrahlung. Physical Review A, 1973, 7(3): 1064–1067
18. Schlessinger L, Wright J. Inverse-bremsstrahlung absorption rate in an intense laser field. Physical Review A, 1979, 20(5): 1934–1945
19. Phelps A V. Rotational and vibrational excitation of molecules by low-energy electrons. Reviews of Modern Physics, 1968, 40(2): 399–410
20. Shakhatov V, Lebedev Y. Kinetics of excitation of $N_2(A^3\Sigma_u^+, v_A)$, $N_2(C^3\Pi_u, v_C)$, and $N_2(B^3\Pi_g, v_B)$ in nitrogen discharge plasmas as studied by means of emission spectroscopy and computer simulation. High Energy Chemistry, 2008, 42(3): 170–204
21. Sugiyama K, Fujii T, Miki M, Yamaguchi M, Zhidkov A, Hotta E, Nemoto K. Laser-filament-induced corona discharges and remote measurements of electric fields. Optics Letters, 2009, 34(19): 2964–2966
22. Czarnetzki U, Luggenhölscher D, Döbele H F. Sensitive electric field measurement by fluorescence-dip spectroscopy of Rydberg states of atomic hydrogen. Physical Review Letters, 1998, 81(21): 4592–4595
23. Zhou B, Akturk S, Prade B, André Y B, Houard A, Liu Y, Franco M, D'Amico C, Salmon E, Hao Z Q, Lascoux N, Mysyrowicz A. Revival of femtosecond laser plasma filaments in air by a nanosecond laser. Optics Express, 2009, 17(14): 11450–11456
24. Oks E A. Plasma Spectroscopy: The Influence of Microwave and Laser Fields. Berlin: Springer-Verlag, 1995
25. Dai J M, Liu J, Zhang X C. Terahertz wave air photonics: terahertz wave generation and detection with laser-induced gas plasma. IEEE Journal on Selected Topics in Quantum Electronics, 2011, 17 (1): 183–190
26. Dai J M, Xie X, Zhang X C. Detection of broadband terahertz waves with a laser-induced plasma in gases. Physical Review Letters, 2006, 97(10): 103903-1–103903-4
27. Moore C A, Davis G P, Gottscho R A. Sensitive, nonintrusive, in-situ measurement of temporally and spatially resolved plasma electric fields. Physical Review Letters, 1984, 52(7): 538–541
28. Wagenaars E, Bowden M D, Kroesen G M W. Measurements of electric-field strengths in ionization fronts during breakdown. Physical Review Letters, 2007, 98(7): 075002-1–075002-4
29. Kolner B H, Buckles R A, Conklin P M, Scott R P. Plasma characterization with terahertz pulses. IEEE Journal of Selected Topics in Quantum Electronics, 2008, 14(2): 505–512
30. Jamison S P, Shen J, Jones D R, Issac R C, Ersfeld B, Clark D, Jaroszynski D A. Plasma characterization with terahertz time-domain measurements. Journal of Applied Physics, 2003, 93(7): 4334–4336
31. Mics Z, Kadlec F, Kuzel P, Jungwirth P, Bradforth S E, Apkarian V A. Nonresonant ionization of oxygen molecules by femtosecond pulses: plasma dynamics studied by time-resolved terahertz spectroscopy. Journal of Chemical Physics, 2005, 123(10): 104310-1–104310-10
32. Kampfrath T, Perfetti L, Gericke D O, Frischkorn C, Tegeder P, Wolf M. Ultrafast capture of free electrons in optically ionized gases by the electron scavenger SF6. Chemical Physics Letters, 2006, 429(4–6): 350–354
33. Köhler R, Tredicucci A, Beltram F, Beere H E, Linfield E H, Davies A G, Ritchie D A, Iotti R C, Rossi F. Terahertz semiconductor-heterostructure laser. Nature, 2002, 417(6885): 156–159
34. Yeh K L, Hoffmann M C, Hebling J, Nelson K A. Generation of 10 μJ ultrashort terahertz pulses by optical rectification. Applied Physics Letters, 2007, 90(17): 171121-1–171121-3
35. Bartel T, Gaal P, Reimann K, Woerner M, Elsaesser T. Generation of single-cycle THz transients with high electric-field amplitudes. Optics Letters, 2005, 30(20): 2805–2807
36. Wu Q, Litz M, Zhang X C. Broadband detection capability of ZnTe electro-optic field detectors. Applied Physics Letters, 1996, 68(21): 2924–2926
37. Grischkowsky D, Keiding S, Exter M, Fattinger C. Far-infrared

time-domain spectroscopy with terahertz beams of dielectrics and semiconductors. Journal of the Optical Society of America B, Optical Physics, 1990, 7(10): 2006–2015
38. Talebpour A, Liang Y, Chin S L. Population trapping in the CO molecule. Journal of Physics B, Atomic, Molecular, and Optical Physics, 1996, 29(15): 3435–3442
39. Xu H L, Azarm A, Bernhardt J, Kamali Y, Chin S L. The mechanism of nitrogen fluorescence inside a femtosecond laser filament in air. Chemical Physics, 2009, 360(1–3): 171–175
40. Iwasaki A, Aközbek N, Ferland B, Luo Q, Roy G, Bowden C M, Chin S L. A LIDAR technique to measure the filament length generated by a high-peak power femtosecond laser pulse in air. Applied Physics B, Lasers and Optics, 2003, 76(3): 231–236
41. Martirosyan A E, Altucci C, Bruno A, de Lisio C, Porzio A, Solimeno S. Time evolution of plasma afterglow produced by femtosecond laser pulses. Journal of Applied Physics, 2004, 96 (10): 5450–5455
42. Fukuchi T, Wuerker R F, Wong A Y. Observation of small electron temperature variations in a nitrogen plasma by laser-induced fluorescence. Journal of Applied Physics, 1994, 75(11): 7237–7239
43. McDaniel E W. Collision Phenomena in Ionized Gases. New York: Wiley, 1964
44. Mlejnek M, Wright E M, Moloney J V. Femtosecond pulse propagation in argon: a pressure dependence study. Physical Review E: Statistical Physics, Plasmas, Fluids, and Related Interdisciplinary Topics, 1998, 58(4): 4903–4910
45. Talebpour A, Petit S, Chin S L. Re-focusing during the propagation of a focused femtosecond Ti:Sapphire laser pulse in air. Optics Communications, 1999, 171(4–6): 285–290
46. Tzortzakis S, Prade B, Franco M, Mysyrowicz A. Time-evolution of the plasma channel at the trail of a self-guided IR femtosecond laser pulse in air. Optics Communications, 2000, 181(1–3): 123–127
47. Bryan R B, Holt R B, Oldenberg O. Recombination and afterglow in nitrogen and oxygen. Physical Review, 1957, 106(1): 83–86
48. Schillinger H, Sauerbrey R. Electrical conductivity of long plasma channels in air generated by self-guided femtosecond laser pulses. Applied Physics B, Lasers and Optics, 1999, 68(4): 753–756
49. Kasparian J, Sauerbrey R, Chin S L. The critical laser intensity of self-guided light filaments in air. Applied Physics B, Lasers and Optics, 2000, 71(6): 877–879
50. Augst S, Strickland D, Meyerhofer D D, Chin S L, Eberly J H. Tunneling ionization of noble gases in a high-intensity laser field. Physical Review Letters, 1989, 63(20): 2212–2215
51. Corkum P B. Plasma perspective on strong field multiphoton ionization. Physical Review Letters, 1993, 71(13): 1994–1997
52. Couairon A, Mysyrowicz A. Femtosecond filamentation in transparent media. Physics Reports, 2007, 441(2–4): 47–189
53. Trushin S A, Kosma K, Fuß W, Schmid W E. Sub-10-fs supercontinuum radiation generated by filamentation of few-cycle 800 nm pulses in argon. Optics Letters, 2007, 32(16): 2432–2434
54. L'Huillier A, Balcou P. High-order harmonic generation in rare gases with a 1-ps 1053-nm laser. Physical Review Letters, 1993, 70 (6): 774–777
55. Paul P M, Toma E S, Breger P, Mullot G, Auge F, Balcou P, Muller H G, Agostini P. Observation of a train of attosecond pulses from high harmonic generation. Science, 2001, 292(5522): 1689–1692
56. Karpowicz N, Zhang X C. Coherent terahertz echo of tunnel ionization in gases. Physical Review Letters, 2009, 102(9): 093001-1–093001-4
57. Bernhardt J, Liu W, Théberge F, Xu H L, Daigle J F, Châteauneuf M, Dubois J, Chin S L. Spectroscopic analysis of femtosecond laser plasma filament in air. Optics Communications, 2008, 281(5): 1268–1274
58. Liu J, Zhang X C. Terahertz-radiation-enhanced emission of fluorescence from gas plasma. Physical Review Letters, 2009, 103 (23): 235002-1–235002-4
59. de Boer M P, Hoogenraad J H, Vrijen R B, Constantinescu R C, Noordam L D, Muller H G. Adiabatic stabilization against photoionization: an experimental study. Physical Review A, 1994, 50(5): 4085–4098
60. Talebpour A, Chien C Y, Chin S L. Population trapping in rare gases. Journal of Physics B, Atomic, Molecular, and Optical Physics, 1996, 29(23): 5725–5733
61. Liu J L, Zhang X C. Plasma characterization using terahertz-wave-enhanced fluorescence. Applied Physics Letters, 2010, 96(4): 041505-1–041505-3
62. Tzortzakis S, Méchain G, Patalano G, André Y B, Prade B, Franco M, Mysyrowicz A, Munier J M, Gheudin M, Beaudin G, Encrenaz P. Coherent subterahertz radiation from femtosecond infrared filaments in air. Optics Letters, 2002, 27(21): 1944–1946
63. Kress M, Löffler T, Eden S, Thomson M, Roskos H G. Terahertz-pulse generation by photoionization of air with laser pulses composed of both fundamental and second-harmonic waves. Optics Letters, 2004, 29(10): 1120–1122
64. Chen Y Q, Yamaguchi M, Wang M, Zhang X C. Terahertz pulse generation from noble gases. Applied Physics Letters, 2007, 91 (25): 251116-1–251116-3
65. Lu X F, Karpowicz N, Chen Y Q, Zhang X C. Systematic study of broadband terahertz gas sensor. Applied Physics Letters, 2008, 93 (26): 261106-1–261106-3
66. Hebling J, Ka-Lo Y, Nelson K A, Hoffmann M C. High-power THz generation, THz nonlinear optics, and THz nonlinear spectroscopy. IEEE Journal of Selected Topics in Quantum Electronics, 2008, 14(2): 345–353
67. Ralchenko Y, Kramida A E, Reader J. NIST Atomic Spectra Database. version 3.1. 5, 2008
68. Rolin M N, Shabunya S I, Rostaing J C, Perrin J M. Self-consistent modelling of a microwave discharge in neon and argon at atmospheric pressure. Plasma Sources Science & Technology, 2007, 16(3): 480–491
69. Zhu X M, Pu Y K. A simple collisional – radiative model for low-pressure argon discharges. Journal of Physics D, Applied Physics, 2007, 40(8): 2533–2538
70. Pine A, Glassbrenner C, Kafalas J. Pressure-tuned GaAs diode-laser absorption spectrocopy of xenon hyperfine structure. IEEE Journal of Quantum Electronics, 1973, 9(8): 800–807
71. Latimer C J, Mackie R A, Sands A M, Kouchi N, Dunn K F. The dissociative photoionization of methane in the VUV. Journal of Physics B, Atomic, Molecular, and Optical Physics, 1999, 32(11):

2667–2676
72. Au J W, Cooper G, Brion C E. The molecular and dissociative photoionization of ethane, propane, and n-butane: absolute oscillator strengths (10–80 eV) and breakdown pathways. Chemical Physics, 1993, 173(2): 241–265
73. Kong F A, Luo Q, Xu H L, Sharifi M, Song D, Chin S L. Explosive photodissociation of methane induced by ultrafast intense laser. Journal of Chemical Physics, 2006, 125(13): 133320-1–133320-5
74. Mittleman D. Sensing with Terahertz Radiation. Berlin: Springer, 2003
75. Federici J F, Schulkin B, Huang F, Gary D, Barat R, Oliveira F, Zimdars D. THz imaging and sensing for security applications—explosives, weapons and drugs. Semiconductor Science and Technology, 2005, 20(7): S266–S280
76. Dai J, Karpowicz N, Zhang X C. Coherent polarization control of terahertz waves generated from two-color laser-induced gas plasma. Physical Review Letters, 2009, 103(2): 023001-1–023001-4
77. Liu J L, Dai J M, Chin S L, Zhang X C. Broadband terahertz wave remote sensing using coherent manipulation of fluorescence from asymmetrically ionized gases. Nature Photonics, 2010, 4(9): 627–631
78. Corkum P B, Burnett N H, Brunel F. Above-threshold ionization in the long-wavelength limit. Physical Review Letters, 1989, 62(11): 1259–1262
79. Kreß M, Loffler T, Thomson M D, Dorner R, Gimpel H, Zrost K, Ergler T, Moshammer R, Morgner U, Ullrich J, Roskos H G. Determination of the carrier-envelope phase of few-cycle laser pulses with terahertz-emission spectroscopy. Nature Physics, 2006, 2(5): 327–331
80. Schumacher D W, Weihe F, Muller H G, Bucksbaum P H. Phase dependence of intense field ionization: a study using two colors. Physical Review Letters, 1994, 73(10): 1344–1347
81. Kulander K C, Schafer K J, Krause J L. Dynamic stabilization of hydrogen in an intense, high-frequency, pulsed laser field. Physical Review Letters, 1991, 66(20): 2601–2604
82. Fedorov M V. Progress in Ultrafast Intense Laser Science. Berlin: Springer, 2006
83. Hatano Y. Interaction of VUV photons with molecules: spectroscopy and dynamics of molecular superexcited states. Journal of Electron Spectroscopy and Related Phenomena, 2001, 119(2–3): 107–125
84. Azarm A, Xu H L, Kamali Y, Bernhardt J, Song D, Xia A, Teranishi Y, Lin S H, Kong F, Chin S L. Direct observation of super-excited states in methane created by a femtosecond intense laser field. Journal of Physics B, Atomic, Molecular, and Optical Physics, 2008, 41(22): 225601-1–225601-4
85. Christophorou L G, Olthoff J K. Electron interactions with excited atoms and molecules. Advances in Atomic, Molecular, and Optical Physics, 2001, 44: 155–293
86. Lao C, Gamero A, Sola A, Petrova T, Benova E, Petrov G M, Zhelyazkov I. Populations of excited atomic states along argon surface-wave plasma columns at low and intermediate pressures. Journal of Applied Physics, 2000, 87(11): 7652
87. Filin A, Compton R, Romanov D A, Levis R J. Impact-ionization cooling in laser-induced plasma filaments. Physical Review Letters, 2009, 102(15): 155004-1–155004-4
88. Wen H, Lindenberg A M. Coherent terahertz polarization control through manipulation of electron trajectories. Physical Review Letters, 2009, 103(2): 023902-1–023902-4
89. Ammosov M V, Delone N B, Krainov V P. Tunnel ionization of complex atoms and of atomic ions in an alternating electromagnetic field. High Intensity Laser Processes, 1986, 664: 138–141
90. Mlejnek M, Wright E M, Moloney J V. Moving-focus versus self-waveguiding model for long-distance propagation of femtosecond pulses in air. IEEE Journal of Quantum Electronics, 1999, 35(12): 1771–1776
91. Exter M, Fattinger C, Grischkowsky D. Terahertz time-domain spectroscopy of water vapor. Optics Letters, 1989, 14(20): 1128–1130
92. Dai J M, Zhang X C. Terahertz wave generation from gas plasma using a phase compensator with attosecond phase-control accuracy. Applied Physics Letters, 2009, 94(2): 021117-1 – 021117-3
93. Huddletsone R H, Leonard S L. Plasma diagnostic techniques. In: Plasma Diagnostic Techniques. New York: Academic, 1965
94. Hopwood J, Guarnieri C R, Whitehair S J, Cuomo J J. Langmuir probe measurements of a radio frequency induction plasma. Journal of Vacuum Science & Technology A, Vacuum, Surfaces, and Films, 1993, 11(1): 152–156
95. Griem H R. Plasma Spectroscopy. New York: McGraw-Hill, 1964
96. Heald M A, Wharton C B. Plasma Diagnostics with Microwaves. New York: McGraw-Hill, 1965
97. Ashby D E T F, Jephcott D F. Measurement of plasma density using a gas laser as an infrared interferometer. Applied Physics Letters, 1963, 3(1): 13–16
98. Krause J L, Schafer K J, Kulander K C. High-order harmonic generation from atoms and ions in the high intensity regime. Physical Review Letters, 1992, 68(24): 3535–3538
99. Kasparian J, Rodriguez M, Méjean G, Yu J, Salmon E, Wille H, Bourayou R, Frey S, Andre Y B, Mysyrowicz A, Sauerbrey R, Wolf J P, Wöste L. White-light filaments for atmospheric analysis. Science, 2003, 301(5629): 61–64
100. Théberge F, Liu W W, Simard P T, Becker A, Chin S L. Plasma density inside a femtosecond laser filament in air: strong dependence on external focusing. Physical Review E: Statistical, Nonlinear, and Soft Matter Physics, 2006, 74(3 Pt 2): 036406-1–036406-7
101. Park H K, Mansfield D K, Johnson L C. Parametric study of electron density profile evolution following injection in TFTR. Review of Scientific Instruments, 1986, 57(8): 1999
102. Jamison S P, Shen J, Jones D R, Issac R C, Ersfeld B, Clark D, Jaroszynski D A. Plasma characterization with terahertz time-domain measurements. Journal of Applied Physics, 2003, 93(7): 4334–4336
103. Kolner B H, Conklin P M, Buckles R A, Fontaine N K, Scott R P. Time-resolved pulsed-plasma characterization using broadband terahertz pulses correlated with fluorescence imaging. Applied Physics Letters, 2005, 87(15): 151501-1–151501-3
104. Crompton R W, Elford M T, Robertson A G. The momentum transfer cross section for electrons in helium derived from drift

velocities at 77°K. Australian Journal of Physics, 1970, 23(5): 667–682
105. Itikawa Y. Cross sections for electron collisions with nitrogen molecules. Journal of Physical and Chemical Reference Data, 2006, 35(1): 31–53
106. Othonos A. Probing ultrafast carrier and phonon dynamics in semiconductors. Journal of Applied Physics, 1998, 83(4): 1789–1830
107. Taylor A J, Erskine D J, Tang C L. Ultrafast relaxation dynamics of photoexcited carriers in GaAs and related compounds. Journal of the Optical Society of America B, Optical Physics, 1985, 2(4): 663–673
108. Prabhu S S, Ralph S E, Melloch M R, Harmon E S. Carrier dynamics of low-temperature-grown GaAs observed via THz spectroscopy. Applied Physics Letters, 1997, 70(18): 2419–2421
109. Averitt R D, Taylor A J. Ultrafast optical and far-infrared quasiparticle dynamics in correlated electron materials. Journal of Physics Condensed Matter, 2002, 14(50): R1357–R1390
110. Mittleman D M, Cunningham J, Nuss M C, Geva M. Noncontact semiconductor wafer characterization with the terahertz Hall effect. Applied Physics Letters, 1997, 71(1): 16–18
111. Leitenstorfer A, Hunsche S, Shah J, Nuss M C, Knox W H. Femtosecond charge transport in polar semiconductors. Physical Review Letters, 1999, 82(25): 5140–5143
112. Beard M C, Turner G M, Schmuttenmaer C A. Transient photoconductivity in GaAs as measured by time-resolved terahertz spectroscopy. Physical Review B: Condensed Matter and Materials Physics, 2000, 62(23): 15764–15777
113. Lui K P H, Hegmann F A. Ultrafast carrier relaxation in radiation-damaged silicon on sapphire studied by optical-pump – terahertz-probe experiments. Applied Physics Letters, 2001, 78(22): 3478–3480
114. Zhou Q L, Shi Y L, Jin B, Zhang C L.Ultrafast carrier dynamics and terahertz conductivity of photoexcited GaAs under electric field. Applied Physics Letters, 2008, 93(10): 102103-1–102103-3
115. Sell A, Leitenstorfer A, Huber R. Phase-locked generation and field-resolved detection of widely tunable terahertz pulses with amplitudes exceeding 100 MV/cm. Optics Letters, 2008, 33(23): 2767–2769
116. Gaal P, Kuehn W, Reimann K, Woerner M, Elsaesser T, Hey R. Internal motions of a quasiparticle governing its ultrafast nonlinear response. Nature, 2007, 450(7173): 1210–1213
117. Danielson J R, Lee Y S, Prineas J P, Steiner J T, Kira M, Koch S W. Interaction of strong single-cycle terahertz pulses with semiconductor quantum wells. Physical Review Letters, 2007, 99 (23): 237401-1–237401-4
118. Wen H, Wiczer M, Lindenberg A M. Ultrafast electron cascades in semiconductors driven by intense femtosecond terahertz pulses. Physical Review B: Condensed Matter and Materials Physics, 2008, 78(12): 125203-1–125203-6
119. Su F H, Blanchard F, Sharma G, Razzari L, Ayesheshim A, Cocker T L, Titova L V, Ozaki T, Kieffer J C, Morandotti R, Reid M, Hegmann F A. Terahertz pulse induced intervalley scattering in photoexcited GaAs. Optics Express, 2009, 17(12): 9620–9629
120. Lakowicz J R, Masters B R. Principles of Fluorescence Spectroscopy. 3rd ed. New York: Springer, 2006
121. Nordstrom K B, Johnsen K, Allen S J, Jauho A P, Birnir B, Kono J, Noda T, Akiyama H, Sakaki H. Excitonic dynamical franz-keldysh effect. Physical Review Letters, 1998, 81(2): 457–460
122. Brinkman W F, Rice T M. Electron-hole liquids in semiconductors. Physical Review B: Condensed Matter and Materials Physics, 1973, 7(4): 1508–1523

**Jingle Liu**–Senior Quantitative Researcher in Bloomberg Tradebook LLC, a global leading agency broker in New York, where his work focuses on trading strategy, statistical models, market microstructure and smart order routing. He received the B.S. degree in physics from Wuhan University, Wuhan, China, in 2004, and the M.S. and Ph.D degrees in physics in 2007 and 2010 from the Rensselaer Polytechnic Institute, Troy, NY. He is the author or coauthor of more than 50 scientific publications including 22 peer-review journal papers and 30 conference papers, 3 US patents and contributor to book chapters in area of physics research.

Previously he was a Co-op with General Electric, where he was engaged in computer modeling and simulation of novel ultrasonic flow sensing/imaging.

His honors and awards include: The Karen & Lester Gerhardt Prize in Science and Engineering (2011), Northeastern Association of Graduate School Best Thesis Award (2011), Small Business Innovation Research Proposal Winner (2010), IMRA Fellowship (2010), Hillard B. Huntington Award for Outstanding Achievement (2010), Founders Award of Excellence (2009), Coherent Award of Excellence (2010).

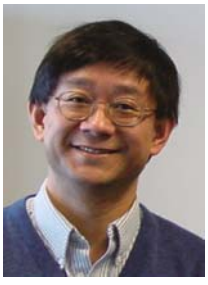

**Xi-Cheng Zhang**–Parker Givens Chair of Optics, assumes Directorship of The Institute of Optics, University of Rochester (UR), NY, a foremost institution in optics and optical physics research and education, on 1/1/2012. Prior to joining UR, he pioneered world-leading research in the field of ultrafast laser-based terahertz technology and optical physics at Rensselaer Polytechnic Institute (RPI), Troy NY (1992 – 2012). At RPI, he is the Eric Jonsson Professor of Science; Acting Head at the Department of Physics, Applied Physics & Astronomy; Professor of Electrical, Computer & System; and Founding Director of the Center for THz Research. He is co-founder of Zomega Terahertz Corp. With a B.S. (1982) from Peking University, he earned the M.S. (1983) and Ph.D degree (1985) in Physics from Brown University, RI.

Previous positions included Visiting Scientist at MIT (1985), Physical Tech. Division of Amoco Research Center (1987), EE Dept. at Columbia University (1987–1991); Distinguished Visiting Scientist at Jet Propulsion Lab, Caltech (2006). He holds 27 U.S. patents, and is a prolific author and speaker. He is a Fellow of AAAS, APS (lifetime), IEEE, OSA (lifetime), and SPIE (lifetime). Dr. Zhang is serving as Editor-in-Chief of Optics Letters (2014 – 2016).

His honors and awards include: IRMMW-THz Kenneth Button Prize (2014); OSA William F. Meggers Award (2012); IEEE

Photonics Society William Streifer Scientific Achievement Award (2011); Rensselaer William H. Wiley 1866 Award (2009); Japan Society for the Promotion of Science Fellowship & NRC-CIAR Distinguished Visiting Scientist, Ottawa, Canada (2004); and First Heinrich Rudolf Hertz Lecturer, RWTH, Aachen, Germany (2003). He also served two years as a Distinguished Lecturer of IEEE/LEOS. He received Rensselaer Early Career Award (1996), Research Corporation Cottrell Scholar Award (1995), NSF Early Career Award (1995), K.C. Wong Prize, K.C. Wong Foundation, Hong Kong (1995), NSF Research Initiation Award (1992). In 1993 – 1994, he was an AFOSR-SRPF Fellow at Hanscom Air Force Base.